이학박사학위논문

암세포의 중심체 과복제와
Cep90 결핍 신장에서의 신장낭 연구

Studies on Centrosome Amplification in Cancer Cells and Cystogenesis in Cep90 Knockout Kidneys

2025년 2월

서울대학교 대학원

생명과학부

신 병 호

암세포의 중심체 과복제와

Cep90 결핍 신장에서의 신장낭 연구

Studies on Centrosome Amplification in Cancer Cells and Cystogenesis in Cep90 Knockout Kidneys

지도교수 이 건 수

이 논문을 이학박사 학위논문으로 제출함
2024 년 11 월

서울대학교 대학원
생명과학부

신 병 호

신병호의 이학박사학위논문을 인준함
2024 년 11 월

위 원 장 _____공영윤_____(인)

부위원장 _____이건수_____(인)

위 원 _____장원열_____(인)

위 원 _____성영훈_____(인)

위 원 _____김진홍_____(인)

Studies on Centrosome Amplification in Cancer Cells and Cystogenesis in Cep90 Knockout Kidneys

A dissertation submitted in partial
fulfillment of the requirement
for the degree of

DOCTOR OF PHILOSOPHY

to the Faculty of
School of Biological Sciences
at
Seoul National University
by

Byungho Shin

Date Approved:
November, 2024

Young Yun Kong

Kunsoo Rhee

Wonyul Jang

Young Hoon Sung

Jin Hong Kim

ABSTRACT

Studies on Centrosome Amplification in Cancer Cells and Cystogenesis in Cep90 Knockout Kidneys

Byungho Shin

Department of Biological Sciences

The Graduate School

Seoul National University

The centrosome is an organelle ubiquitously present in nearly all types of animal cells. It is involved in a variety of cellular processes including mitotic spindle pole formation and nucleation of microtubules in interphase. Another essential function of the centrosome is serving as a template for the primary cilium. Primary cilium is cellular antenna which integrates and modulates a wide array of signaling pathways. Given the universal presence of centrosomes in vertebrate cells, primary cilia also function across diverse cell types. Due to their extensive roles, structural or functional abnormalities in centrosome or cilia are implicated in numerous human diseases, including cancer and polycystic kidney disease. However, understanding how defects in these organelles contribute to disease remains challenging, as these defects are multifaceted and occur within varied physiological contexts.

In this study, I investigated the novel aspects of centrosome and cilia aberrations in the context of cancer and polycystic kidney disease, respectively. As part of elucidating centrosome aberration in cancer, I investigated the amplification mechanism of centrosomes in cancer cells

thereby elucidating the novel mechanisms of centrosome amplification at M phase. Using a panel of cancer cell lines, I assessed the relationship between cell cycle stage and centrosome amplification. I found out that a few cell lines analyzed exhibited novel fashion of centrosome amplification at M phase. To further delineate the M-phase specific centrosome amplification mechanisms, I characterized the property of centrosomes in that cell lines interrogating centriole separation status, susceptibility to a drug inhibiting centriole duplication kinase, and cellular levels of pericentriolar material. Additionally, I demonstrated that the overexpression of pericentriolar material protein significantly suppressed centrosome amplification in a few cell lines. Based on these results, I propose that a sub-threshold level of pericentriolar material can result in centrosome amplification in cancer cells.

As a means to investigating cilia aberration in kidney disease, I examined the dynamics of cilia-associated kidney disease progression using a mouse model in which the gene *Cep90* was specifically knocked out in kidney. The *Cep90* KO mice exhibited polycystic kidney disease and concurrent loss of cilia. Notably, the *Cep90* KO mice displayed a slow progression of the disease, allowing for a detailed investigation of ciliary involvement in cystogenesis. The *Cep90* KO mice exhibited fully formed late-stage cysts in which comprising cells are totally losing cilia and partially formed early-stage cysts in which ciliated and non-ciliated cells co-reside. I analyzed the signaling pathways known to be involved in cystogenesis and found out that there are temporal dynamics among them. mTOR signaling was specifically upregulated in non-ciliated cells in early-stage cysts, whereas non-ciliated cells in late-stage cysts did not upregulate mTOR signaling implying that another signaling pathways are involved in maintenance and progression of the disease. Unlike mTOR signaling, YAP was activated from early-stage cysts and its activation persisted throughout cyst development, independent of ciliary status. Based on these results, I propose that defects in cilia can lead to polycystic kidney disease by direct and indirect pathways which exhibit distinct temporal dynamics.

Keywords: Centrosome, pericentriolar material, Cep90, cancer, polycystic kidney disease

Student number: 2020-21683

CONTENTS

LIST OF FIGURES

BACKGROUNDS

1. Centrosome

Centrosome is an organelle ubiquitously present in most of the animal cells. As it is present in a wide variety of cells, it is crucial for many cellular processes including mitotic spindle pole formation and organizing interphase microtubule network by nucleating microtubules (Nigg and Holland, 2018). In addition, it serves as a template for primary cilia when ciliogenic cue is present in a cell (Derderian et al., 2023). Considering its diverse roles and nearly ubiquitous presence, abnormalities of centrosome can lead to a variety of diseases.

1.1. Structure and function of centrosome

The centrosome is an ultrastructure composed of a variety of subcomplexes. In addition, it is unique in that a cell normally contains two centrosomes which undergo slight modification and duplication throughout the cell cycle (Nigg and Holland, 2018). At G1 phase, the centrosome is composed of two centrioles which are microtubule-based cylinders (Fig. 1). They are linked to each other by protein linker complexes and they are also enwrapped by protein matrix called pericentriolar material (PCM) which functions as microtubule organizing center. Notably, at G1 phase, one of the two centrioles possesses subcomplex called distal appendages which will be later required for docking to plasma membrane when primary cilium is formed. At S phase, centrioles start to duplicate. At G1-S transition phase, a single new centriole is formed at a perpendicular angle to a pre-existing centriole with the aid of a kinase called polo-like kinase 4 (PLK4) (Fig. 2). These newly formed centrioles are called

procentrioles, which will be continuously elongated throughout the remaining cell cycle phases. At G2 phase, centrosome starts to accumulate PCM preparing for accurate execution of mitosis. At M phase, two centrosomes become disconnected by dissolution of linker complexes and a centriole pair in a centrosome is separated. At this stage, mitotic PCM enwraps the separated centrioles so that a mitotic cell possesses two mitotic spindle poles which nucleate mitotic spindles (Kim et al., 2019). Following telophase, PCM undergoes drastic re-organization and two centrioles are liberated in that they make two centrosomes in the next cell cycle.

The function of centrosome can be dissected corresponding to distinct cell cycle phases. In interphase, they nucleate most of the microtubules in a cell and organize microtubule network which is essential for transport of proteins or organelles with the aid of microtubule-associated motor proteins (Fig. 3). In addition, it is involved in cellular migration harmonizing with actin filaments. At mitosis, centrosome functions as spindle pole which is essential for accurate segregation of chromosomes into a daughter cell.

1.2. Centrosome and cancer

Since the centrosome is crucial for segregating chromosomes into daughter cells, abnormal centrosome can lead to inaccurate chromosome segregation, which is the hallmark of cancer (Chan, 2011). Consistent with this, high proportion of cancer cells exhibits abnormality in centrosome, for example, centrosome amplification or loss of centrosomes. Although there are limited evidences that centrosome abnormality induces carcinogenesis, dysfunction of the centrosome can promote cancer progression in many ways. Chromosomal instability (CIN) is one of the outcomes that improper chromosome segregation by dysfunctional centrosome can bring (Marthiens et al., 2013). Though aneuploidy per se can be beneficial or detrimental to cancer cell, it promotes cancer evolution via providing diverse genetic pools that selection pressure can act on. Another way of promoting cancer progression is via enhancing invasion of cancer cells. It is reported that supernumerary centrosomes

promote excessive microtubule nucleation which promotes cell-autonomous invasion (Godinho et al., 2014). Furthermore, cancer cells with centrosomes are known to promote invasion of adjacent cells via paracrine signaling. Overall, abnormality in centrosome can be a multifaceted factor which aggravates cancer progression.

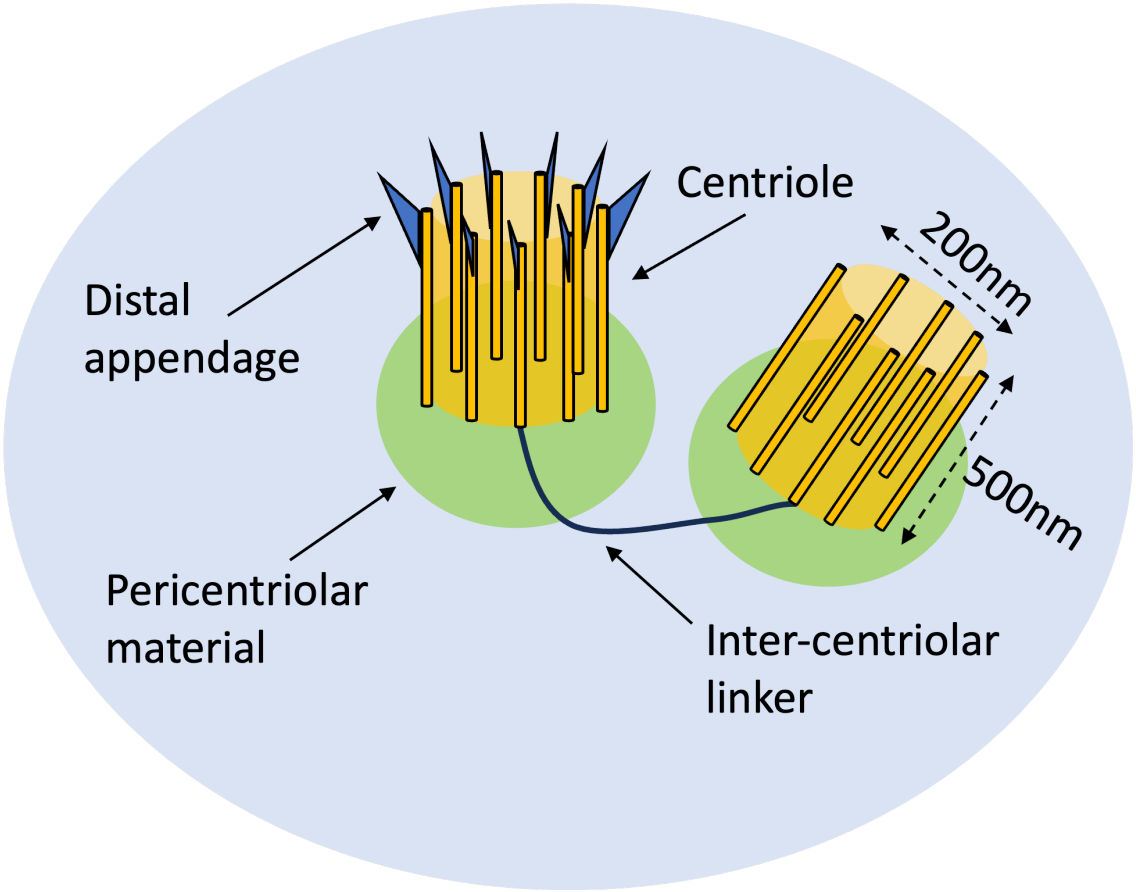

Figure 1. Structure of the centrosome Illustration of G1 phase centrosome. Each centriole is composed of 9 triplets of microtubules and a centriole pair is connected by inter-centriolar linker. Each centriole is surrounded by pericentriolar material, protein matrix essential for microtubule organization. Older centriole is decorated with distal appendages at its distal part.

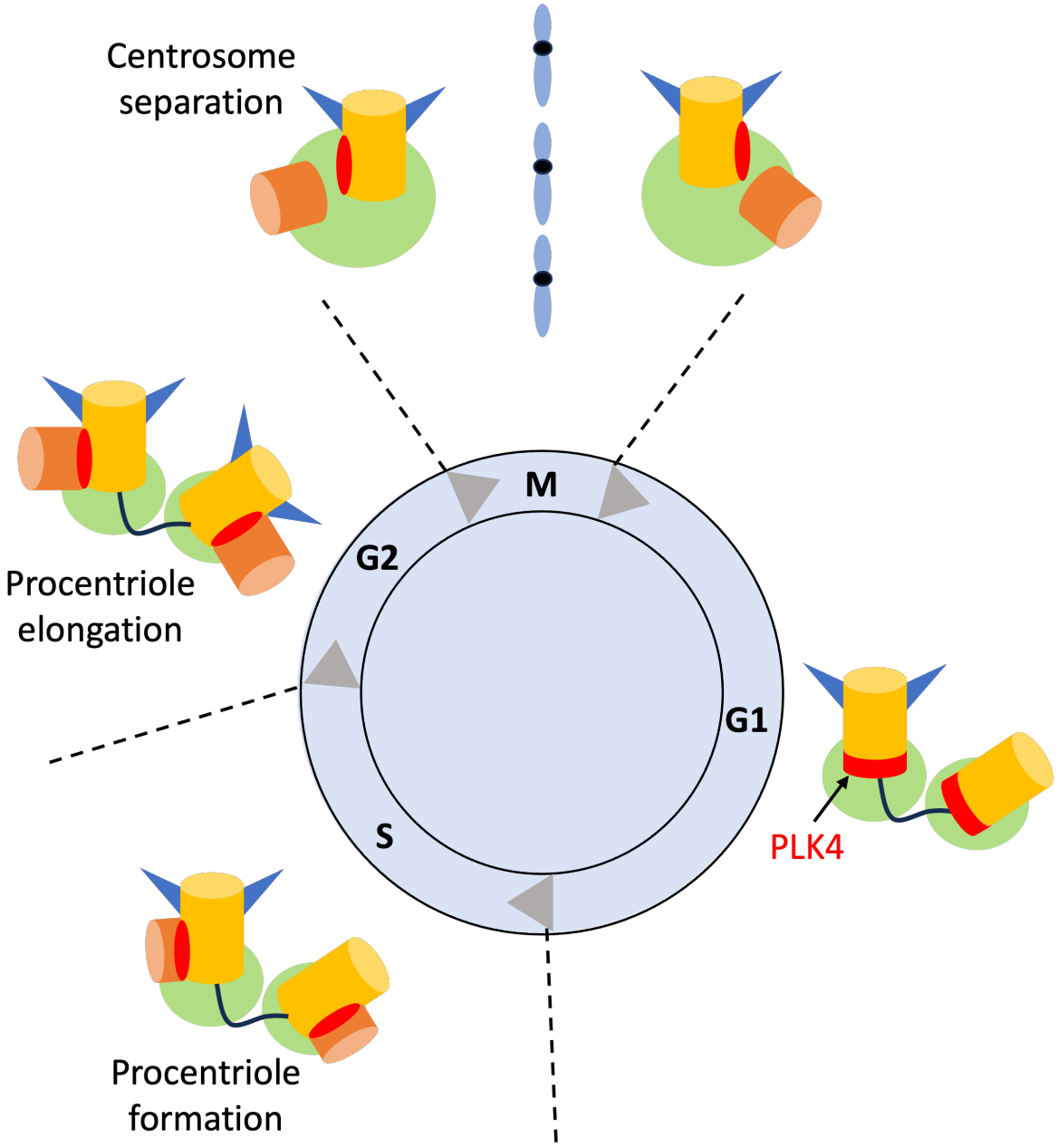

Figure 2. Centrosome duplication cycle At G1 phase, centrosomes comprise one centriolar pair. Each centriole harbors PLK4 ring at its proximal part. At G1-S transition PLK4 coalesces at one discrete point thereby building a site for centriole biogenesis. At this point, procentriole is formed. Following S and G2 phase, procentriole elongates to a certain point. At M phase, two centrosomes are separated by dissolution of inter-centriolar linker to form spindle poles. Furthermore, a centriole pair disengages but is enwrapped by pericentriolar material. Following telophase, each centriole pair is inherited to daughter cells to be two centrosomes.

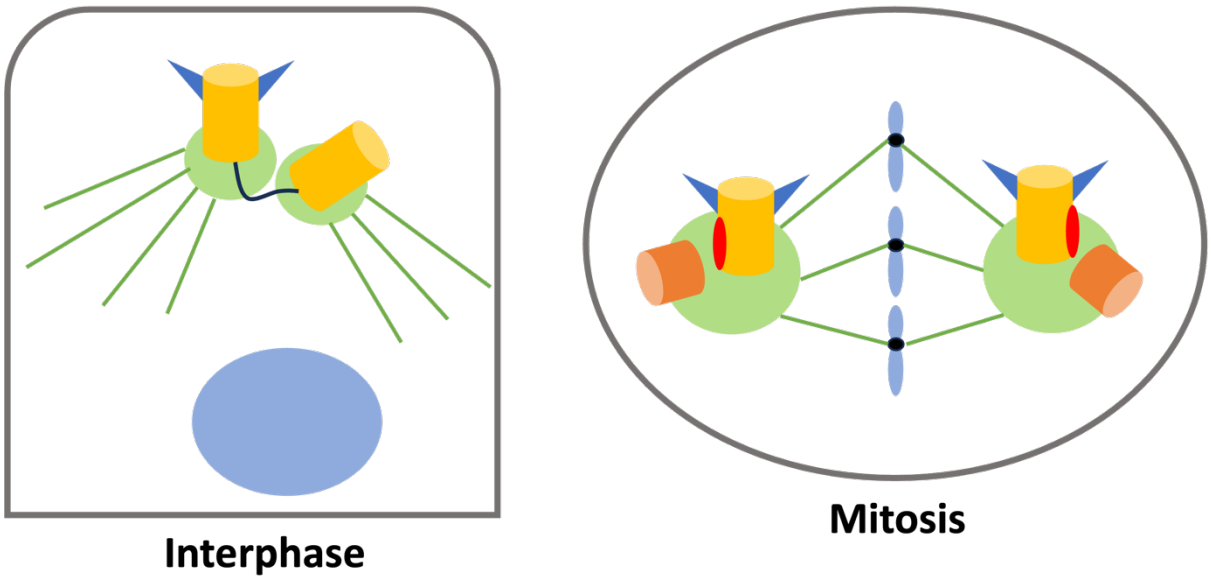

Figure 3. Function of centrosome During interphase, centrosome functions as a major microtubule organizing center. Consequently, it is involved in cellular trafficking, cellular migration and also maintenance of cell morphology. During mitosis, centrosomes form spindle poles which is essential for segregating sister chromatids to daughter cells.

2. Primary cilia

2.1 Structure and function of primary cilia

Primary cilium is an organelle which protrudes from a centriole when ciliogenic cue is present. It is a solitary organelle which is essential for transducing diverse cellular signaling pathways and exists in nearly all types of cells in vertebrates (Derderian et al., 2023). Cilia are ultrastructure comprising various sub-complexes (Fig. 4) (Kumar et al., 2021). Distal appendages are complexes required for membrane anchoring of cilia. Transition zone is the region where protein complexes form molecular sieves separating cilioplasm from cytoplasm. Lastly, axoneme, a microtubule-based structure, is formed from pre-existing centriole. Since cilia are composed of various components and its formation is a multistep process, dysfunction of any of these components is known to result in defective cilia.

The importance of primary cilia in vertebrates is related to its function as cellular antennae which transduces multiple signaling pathways. Canonical hedgehog signaling is the most prominent one since canonical hedgehog signaling should be transduced through primary cilia not elsewhere. When Hedgehog ligand arrives, Smoothened translocates to primary cilia and transcriptional effector Gli is activated. Furthermore, flow sensing is another prominent function of cilia. Cilia bending by fluid flow is known to regulate some signaling pathways. mTOR is known to be inactivated by flow-sensing of LKB1 in cilia which in turn activates AMPK (Boehlke, 2010). Furthermore, the same pathway is reported to inactivate YAP when cilia are subjected to fluid flow (Claude-Taupin et al., 2023). Besides these pathways, Wnt signaling and calcium signaling are also regulated by primary cilia.

2.2 Ciliopathy

Since primary cilia are involved in a myriad of signaling pathways and exists nearly ubiquitously in vertebrate tissues, dysfunction of cilia is known to cause multi-organ diseases which are collectively termed as 'ciliopathy' (McConnachie et al., 2021). Ciliopathy phenotypes range from retinal degeneration, polydactyly to congenital heart defects just to name a few. The limitation to understand the ciliopathy lies in its diversity. Since cilia are involved in diverse signals, it is hard to pinpoint which signals contribute to pathogenesis when cilia are abrogated. Furthermore, a large pool of causative genes makes deciphering the pathogenic mechanism challenging. To data, more than 50 genes were identified as ciliopathy-associated genes. These genes encode proteins essential for structural components of cilia or receptors involved in cilia-associated signaling pathways. However, interrogation of ciliopathy phenotypes caused by mutation in one of the structure-associated genes can give insights that can be translated to the case caused by another structure-associated genes.

2.3. Polycystic kidney disease

Polycystic kidney disease (PKD) is a disorder characterized by the formation of fluid-filled cysts in the kidneys (Fig. 5) (Ma, 2021). In PKD, renal tubules become severely dilated, with cells that flatten and exhibit a high proliferative potential. Over time, these cysts damage the normal renal parenchyma, leading to end-stage renal disease. PKD is commonly associated with structural or functional defects in primary cilia.

Autosomal dominant polycystic kidney disease (ADPKD) is the most common form of PKD, resulting from mutations in either the *PKD1* or *PKD2* genes. These genes encode membrane proteins that localize to cilia and are presumed to play roles in calcium signaling, although their exact functions remain unknown (Harris and Torres, 2009). Consequently, ADPKD is considered a type of PKD driven by functional abnormalities of cilia. The second

type of PKD is ciliopathy-linked PKD, which results from structural abnormalities in primary cilia and is inherited in an autosomal recessive pattern, unlike ADPKD. Pathogenesis in ciliopathy-linked PKD is associated with the complete absence or shortening of cilia.

Beyond these genetic etiologies, various signaling pathways are implicated in PKD pathogenesis (Harris and Torres, 2009). In particular, cAMP signaling is heavily associated with ADPKD, while mTOR signaling is thought to be upregulated in PKD. However, the initiating signaling pathways remain unclear. The diverse phenotypes observed in mouse models further complicate our understanding of cystogenesis. In ADPKD mouse models with intact cilia, severe cyst formation is common. However, cyst severity decreases when *Pkd1* or *Pkd2* is co-deleted with primary cilia (Ma et al., 2013). In contrast, mice with cilia ablation but intact *Pkd1* or *Pkd2* genes exhibit mild cyst formation (Derderian et al., 2023). These epistatic interactions suggest that the mechanisms driving cystogenesis may overlap across different genetic backgrounds, while also possessing unique aspects specific to each mutation.

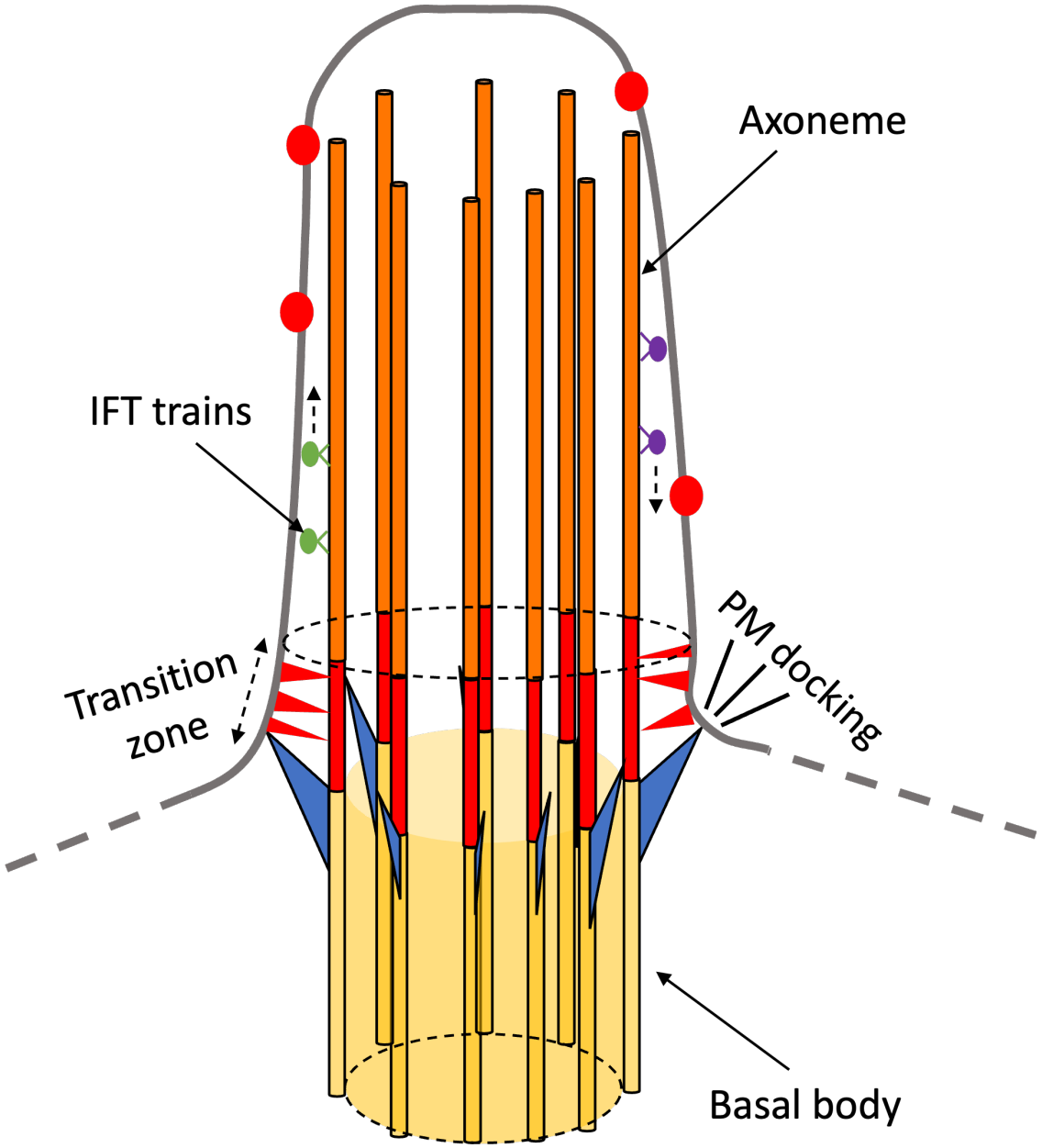

Figure 4. Structure of primary cilia Primary cilium is an organelle which protrudes from basal body, a centriole which is decorated with components essential for formation of cilia. From basal body, axoneme, modified 9-fold microtubule array, is formed. At this event, docking of basal body to plasma membrane enables pushing it concomitantly with axoneme elongation. Transition zone demarcates cilioplasm from cytoplasm. IFT trains function as trafficking machinery in cilia with the aid of motor proteins. Furthermore, transmembrane proteins such as PKD1/PKD2 complex localize to primary cilia, which allow it to function as sensory organelles.

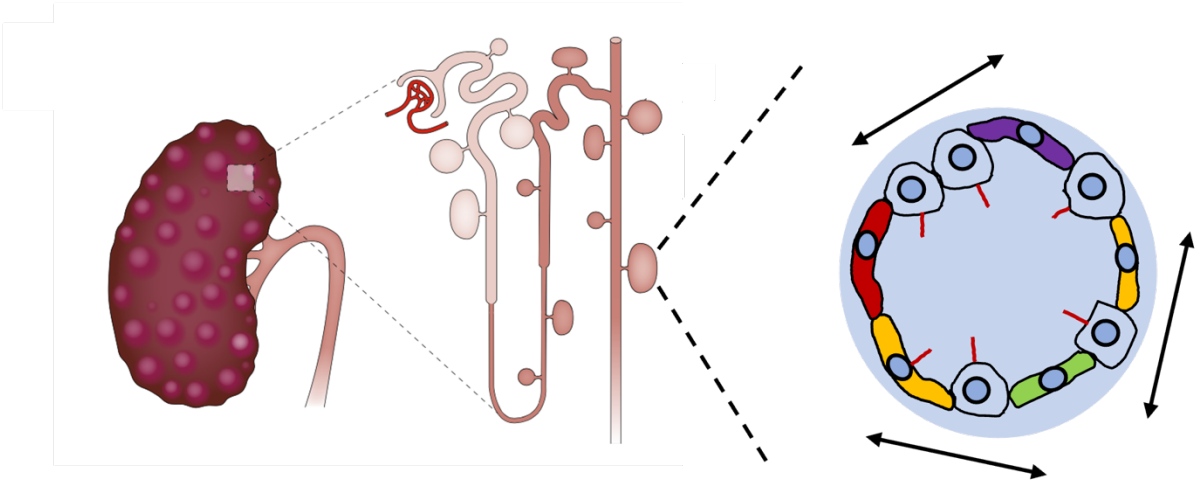

Figure 5. Polycystic kidney disease Polycystic kidney disease (PKD) is characterized by fluid-filled sacs across nephrons. Diverse signaling pathways are involved in the initiation and progression of PKD which collectively enlarges tubular lumen by promoting proliferation and morphological change of constituent cells. (Revised from Bergmann et al., 2018)

PURPOSE

The centrosome and cilia are ubiquitous organelles whose function is critical for cellular physiology. As such, aberrations in either structure or function of the centrosome and cilia can lead to severe diseases across multiple organs. Given that centrosome and cilia are organelles composed of multiple subcomplexes where a vast array of components are engaged, their complexity has posed challenges to fully elucidating the pathologies associated with them. Consequently, it still remains unclear how specific defects in centrosome and cilia translate into distinct pathological outcomes across different disease contexts.

In this study, I aimed at elucidating novel aspects of centrosome and cilia-associated diseases in the context of cancer and polycystic kidney disease. In the context of cancer, I verified the possible role of pericentriolar material in suppressing centriole amplification. Furthermore, concerning polycystic kidney disease, I examined how structural defects in cilia contribute to ciliopathy-associated polycystic kidney disease, a relatively underexplored type of polycystic kidney disease. Through this work, I sought to deepen understanding of how specific centrosome and cilia dysfunctions contribute to disease.

Chapter I.

M-phase-specific generation of supernumerary centrioles in cancer cells

ABSTRACT

Many cancer cells maintain supernumerary centrioles, despite the potential risks associated with catastrophic outcomes during mitosis. In this study, I searched for cancer cell lines in which supernumerary centrioles are generated during the M phase and identified a few cell lines among the dozen examined. PLK4 activity is also required for M-phase-specific generation of supernumerary centrioles. I observed that mitotic centrioles prematurely separate in many cancer cells when levels of pericentriolar material (PCM) proteins, such as PCNT and CEP215, are low. Furthermore, the presence of supernumerary centrioles was correlated with reduced mitotic PCM levels. Notably, overexpression of PCNT led to a reduction in supernumerary centrioles in MDA-MB-157 cells. These findings suggest that diminution of mitotic PCM may be a cause of M-phase-specific generation of supernumerary centrioles in selected cancer cells.

INTRODUCTION

Many cancer cells maintain supernumerary centrioles, despite the catastrophic challenges they pose during mitosis (Chan, 2011; Marteil et al., 2018; Morretton et al., 2022). As one of coping mechanisms, extra centrosomes form clusters to facilitate spindle formation and eventually segregate a set of chromosomes into daughter cells (Kwon et al., 2008; Song et al., 2023). However, this process takes longer for the execution of mitosis and frequently disrupts balanced chromosome segregation. The presence of extra centrosomes is, indeed, considered a common underlying cause for chromosomal instability in cancer cells (Song et al., 2023; Ganem et al., 2009).

Several mechanisms have been proposed for generation of supernumerary centrioles in cancer cells (reviewed in Shin et al., 2021). First, overexpression of centriole assembly factors, such as PLK4, a central regulator of centriole assembly, can generate extra centrioles in the S phase (Bettencourt-Dias et al., 2005; Habedanck et al., 2005; O'Connell et al., 2001). Therefore, tight regulation of these assembly factors is essential for maintaining normal centriole numbers; otherwise, supernumerary centrioles could be generated. Elevated levels of PLK4 are indeed detected in a variety of tumor cells (Li et al., 2016; Liao et al., 2019).

Second, it is well-established that cytokinesis failure frequently occurs in cancer cells (Sagona and Stenmark, 2010; Lens and Medema, 2019). Indeed, whole genome doubling is known to precede aneuploidy in approximately one-third of tumors (Zack et al., 2013). Direct examination of cells in primary human tumors revealed high incidence of cytokinesis failure, leading to generation of extra centrosomes (Krajcovic et al., 2011). While extra centrosomes in non-transformed cells are often rapidly lost from the cell population after several cell divisions (Ganem et al., 2009; Krzywicka-Racka et al., 2011; Godinho et al., 2014; Potapova etal., 2016; Galofré et al., 2020), the loss of p53 may create a permissive environment for supernumerary centrioles as cells fail to sense mitotic delays caused by defects in bipolar spindle formation (Galipeau et al., 1996; Fukasawa et al., 1996; Lambrus et al., 2017; Lambrus et al., 2016).

Finally, unscheduled centriole assembly is known to occur during the G2 and M phases. Structural aberrations and over-elongation of centrioles are frequently observed in various

tumor cells (Chan, 2011; Marteil et al., 2018). Severe centriole over-elongation can promote amplification through both centriole fragmentation and ectopic procentriole formation along their elongated walls (Marteil et al., 2018; Kohlmaier et al., 2009).

In this study, I screened cancer cells in which supernumerary centrioles are generated at M phase through a novel mechanism derived from lack of surrounding protein matrix called pericentriolar material (PCM). In a normal cell, a daughter centriole assembles next to the mother centriole during the S phase, and it remains engaged with the mother centriole until the M phase. Upon entering mitosis, daughter centrioles disengage from the mother centrioles but remain associated within the centrosome, surrounded by PCM (Shukla et al., 2015). If, for some reason, centrioles are liberated from PCM, they acquire the ability to generate centrioles even during the M phase (Karki et al., 2017; Kim et al., 2019; Jung and Rhee, 2021). For example, deletion of *pericentrin* (*PCNT*) reduces mitotic PCM, resulting in precocious centriole separation and centriole assembly at M phase (Kim et al., 2019; Jung and Rhee, 2021). PCM may be also dissipated from the centrosomes, when the cells are arrested at G2 and M phase for a prolonged period (Karki et al., 2017; Cabral et al., 2013; Seo et al., 2015). While the M-phase-assembly of centrioles are disclosed through genetic manipulations of centrosome-associated genes in tissue culture cells, it remains largely elusive whether this unscheduled centriole formation mechanism genuinely operates for generation of supernumerary centrioles in unmanipulated, natural cancer cells or not. In this study, I sought to investigate mechanisms for supernumerary centriole generation operating in a number of natural cancer cell lines. Ultimately, my findings provide evidence that precocious centriole separation accompanied with PCM reduction effectively operates to generate supernumerary centrioles in selected cancer cells.

MATERIALS & METHODS

Cell culture, synchronization and transfection

SKBR3, BT20, HCC1937, HCC1954, RD, H23, PANC1, DU145, PC3, and HCT116 cell lines were obtained from Korean Cell Line Bank. MDA-MB-157, MDA-MB-468, MDA-MB-231, and MCF7 were gifts from Dr. Won Shik Han (Seoul National University College of Medicine). BT549 and Hs589T were gifts from Dr. Sujae Lee (Hanyang University College of Medicine). PLK4-overexpressing HeLa (HeLa PLK4-OE) and *TP53/PCNT/CEP215* triple knockout HeLa (HeLa TKO) were previously described (Jung and Rhee, 2021).

HeLa, HeLa PLK4-OE, MDA-MB-468, MDA-MB-231, MCF7, Hs578T, RD, PANC-1 and HCT116 were cultured in DMEM (LM001-05, Welgene, South Korea) supplemented with 10% fetal bovine serum (FBS, S101-01, Welgene, South Korea) and antibiotics (ANT-MPT, Invivogen). MDA-MB-157, BT549, SKBR3, BT20, HCC1954, HCC1937, NCI-H23, DU145 and PC3 were cultured in RPMI1640 (LM011-01, Welgene, South Korea) supplemented with 10% FBS and antibiotics. RPE1 was cultured in DMEM/F12 (LM030-01, Welgene, South Korea) supplemented with 10% FBS and antibiotics. HeLa TKO was cultured in DMEM supplemented with 10% Tet-approved FBS (630017, Takara) to minimize leaky expression. All cell lines were maintained in a 5% CO_2 atmosphere at 37°C. For overexpression of PLK4, PLK4-OE HeLa was treated with 100 ng/ml doxycycline (D9891, Sigma-Aldrich).

For cell cycle synchronization, the cells were treated with 2 mM thymidine for 24 h, released, treated with 5 μM RO3306 for 8 h, released, and fixed at specific timepoints. S phase cells were fixed at the end of the thymidine treatment. G2 phase cells were fixed at the end of the RO3306 treatment, M phase cells were fixed at 0.5 h after the RO3306 release, and G1 phase cells were fixed at 4 h after the RO3306 release. To enrich mitotic cells, the cells were treated with 2mM thymidine for 24 h, released, and treated with 10 μM STLC for 9.5 h. For inactivation of PLK4, 100 nM centrinone was treated (Wong et al., 2015).

HeLa, HeLa TKO, MDA-MB-231, and MDA-MB-157 was transiently transfected with the expression vectors, using Lipofectamine 3000 (Invitrogen). Twenty-four hours later, the transfected cells were treated with thymidine for 24 h, followed by STLC for 9.5 h, and fixed for immunostaining analyses.

Antibodies

The following primary antibodies were used in this study: rabbit antibodies against CEP135 (1:500) (Kim et al., 2008), CP110 (1:500) (Kim et al., 2008), CEP215 (1:500) (Lee and Rhee, 2010) and pericentrin (1:1000) (Kim and Rhee, 2011); mouse antibodies against centrin-2 (04-1624, Millipore; 1:500), cyclin B1 (SC-245, Santa Cruz; 1:50), BrdU (B5002, Sigma-Aldrich; 1:1000) and the Flag-tag (F3165, Sigma-Aldrich; 1:200). Secondary antibodies conjugated with fluorescent dyes (Alexa Fluor 488, 594 and 647; Invitrogen; 1:1000) were used.

Immunofluorescence staining and microscopy

For immunofluorescence analysis, the cells were cultured on coverslips. The cells were fixed with -20°C methanol for 10 min, washed with PBS three times, permeabilized with PBST (PBS with 0.1% Triton X-100) for 10 min, incubated with a blocking solution (PBST with 3% bovine serum albumin) for 30 min at room temperature. The cells were then incubated with the primary antibodies for 1 h, washed with PBST three times, incubated with the secondary antibodies for 30 min, washed with PBST twice, stained with 4,6-diamidino-2-phenylindole (DAPI) for 2 min, and washed twice with PBST. The coverslips were mounted on a slide with ProLong Gold antifade reagent (P36930, Life Technologies).

For determination of cell cycle stages in asynchronous populations, the cells were treated with 20 μM BrdU for 30 min prior to fixation. The cells were coimmunostained with the cyclin B1, centrin-2 and CP110 antibodies and post-fixed with 4% paraformaldehyde (PFA) overnight at 4°C. The post-fixed cells were washed with PBS three times, denatured with the treatment of pre-heated 37°C 2N HCl, neutralized with the sodium borate buffer (pH8.5) for 10 min and washed with PBST three times. The cells were then incubated with the blocking solution for 30min, incubated with the BrdU antibody for 1 h, washed with PBST three times, and incubated with secondary antibody for 30 min, stained with DAPI for 2 min, and mounted on a slide glass. In case of 4-channel staining, pre-labeled antibodies were prepared using Zenon IgG labeling kits (Invitrogen) and the cells were treated with them after incubation with the secondary antibodies.

For phalloidin staining, the cells were fixed using 4% PFA, washed with PBS, permeabilized with PBST for 10 min and incubated with rhodamine-conjugated phalloidin (Invitrogen, R415). The cells were stained with DAPI for 2 min and mounted on a slide glass.

Acquiring the images and counting the number of fluorescent signals were performed using a fluorescence microscope (IX51, Olympus, Tokyo, Japan) equipped with 60×/1.35 NA UPlanSApo objective lens and with a CCD camera (Qicam Fast 1394, Teledyne Photometrics, Tucson, AZ, USA) or using a confocal laser-scanning microscope system (LSM700, Carl Zeiss, Germany) equipped with 100×/1.4 NA Plan-Apochromat objective lens. Intensities of the fluorescent signals were analyzed using ImageJ (National Institutes of Health).

DepMap data source and CA20 score analysis

I used a publicly available data source from Cancer Cell line Encyclopedia (CCLE) to obtain expression profiles of cell lines examined. RNA-seq data for expression profiles of 1,479 cancer cell lines were obtained from DepMap expression public 23Q4. RNA-seq data of the genes were log2 transformed with a pseudo count of 1. To estimate relative CA20 score, expression levels of CA20 genes were log2-median centered and summed. The CA20 genes in this study are as follows: *AURKA*, *CCNA2*, *CCND1*, *CCNE2*, *CDK1*, *CEP63*, *CEP152*, *E2F1*, *E2F2*, *LMO4*, *MDM2*, *MYCN*, *NDRG1*, *NEK2*, *PIN1*, *PLK1*, *PLK4*, *SASS6*, *STIL* and *TUBG1*.

Flow cytometry

For FACS analysis, the cells were harvested with 0.25% (w/v) Trypsin/EDTA (LS015-01, Welgene, South Korea), fixed with cold 70% ethanol with vortex and stored at 4°C for 10 min. The cells were washed three times with PBS and stained with propidium iodide (PI) with RNase and EDTA (pH 7.5). About 10000 cells were counted for each sample to draw the PI histogram plots. FACS data was collected in FACS CANTO 2 (BD Biosciences).

Statistical analysis

For statistical analyses, experiments were independently performed three times. To calculate *P*-values, unpaired two-tailed *t*-test, one-way analysis of variance (ANOVA) were

performed in Prism 5 (GraphPad Software). In the case of ANOVA, the Tukey's post-test or Newman-Keuls post-test was performed when the *P*-values were lower than 0.5.

RESULTS

Cell cycle stage-specificity of supernumerary centriole acquisition in cancer cell lines

Supernumerary centrioles are maintained at discrete proportions in cancer cell lines (Marteil et al., 2018). To determine the cell-cycle-stage specificity in acquisition of supernumerary centrioles, I synchronized the cancer cells with the thymidine-RO3306 block and release method (Fig. 6A). Cell cycle synchronization was confirmed through fluorescence-activated cell sorting analysis (Fig. 6B). Cell cycle stages of individual cells were determined by coimmunostaining with antibodies specific to the cell cycle stages (BrdU and cyclin B1), along with the centrin-2 and CP110 antibodies which detect the core and distal end of centrioles, respectively (Fig. 6C). As results, the S and G2 phase cells were immunostained with the BrdU and cyclin B1 antibodies, respectively (Fig. 6D). G1 phase cells showed no signal, and M phase cells were identified through DAPI staining (Fig. 6D). As controls, HeLa displayed minimal percentages of cells with supernumerary centrioles in all cell cycle stages (Fig. 7A). *TP53;PCNT;CEP215* triple KO HeLa (HeLa TKO) displayed significant acquisition of supernumerary centrioles at M phase, as reported previously (Jung and Rhee, 2021) (Fig. 7A). On the contrary, PLK4-overexpressing HeLa (HeLa PLK4-OE) displayed supernumerary centrioles in all cell cycle stages, possibly due to inheritance of the centrioles which had been generated at the preceding cell cycle (Fig. 7A). Among the cancer cell lines, PANC-1, DU145 and HCT116 displayed high percentages of supernumerary centrioles in all cell cycle stages, implying that they constitutively retained supernumerary centrioles (Fig. 7A). I also observed cell-cycle-stage-specific acquisitions of supernumerary centrioles, such as HCC1954 and NCI-H23 at S phase, BT549 at G2 phase, and MDA-MB-157 and MDA-MB-231 at M phase (Fig. 7A). These results reveal that cancer cell lines exhibit distinct patterns of supernumerary centrioles concerning the cell cycle stage, as summarized in Fig. 7B.

M-phase-specific generation of supernumerary centrioles

Among several different mechanisms for generation of supernumerary centrioles, I just focused on mechanisms in which they are generated at G2 and M phases. I did not pay attention to the cancer cell lines in which centriole assembly-associated genes are overexpressed, based on gene expression profile analyses (Fig. 8). Nor did I pay attention to the cancer cell lines in which cytokinesis frequently fails (Fig. 9).

PLK4 is a key enzyme for daughter centriole assembly at G1/S transition phase (Kleylein-Sohn et al., 2007). The PLK4 activity surges at G1/S transition phase and prevails up to M phase (Zitouni et al., 2016). To determine involvement of PLK4 in generation of supernumerary centrioles at M phase, I treated centrinone, a PLK4 inhibitor, to the G2 phase cells which already contained both mother and daughter centriole pairs. The cells were accumulated at G2/M phase border with RO3306 and released to M phase, and centrinone was treated for 8.5 h at the end of the culture (Fig. 10A). My results revealed that centrinone hardly affects proportions of supernumerary centriole-containing cells in PLK4-overexpressing HeLa and NCI-H23 cell lines (Fig. 10B). These results are expected, since most of their supernumerary centrioles are generated at G1/S transition phase (Fig. 7D). On the contrary, centrinone reduced the number of supernumerary centriole-containing HeLa TKO cells in which supernumerary centrioles are known to assemble at M phase (Fig. 7D; Jung and Rhee, 2021). The number of supernumerary centriole-containing M phase cells was also reduced in MDA-MB-157 cells supporting the notion that their supernumerary centrioles are generated at M phase with the PLK4 activity (Fig. 10B). Intriguingly, supernumerary centrioles were only slightly suppressed by centrinone in MDA-MB-231 (Fig. 10B). Precocious centriole separation was mostly unaffected when centrinone was treated at G2 phase cells (Fig. 10C).

A similar experiment was carried out with the cells whose cell cycle was arrested at S phase with aphidicolin (Fig. 11A). My results revealed that centrinone inhibited generation of supernumerary centrioles in HeLa TKO and MDA-MB-157 cells after G1/S transition as well (Fig. 11B). These results indicate that supernumerary centrioles can be generated at M phase in selected cancer cell lines with help of the PLK4 activity. It is interesting that prolonged treatment of aphidicolin enhanced precocious centriole separation in most cell lines tested (Fig. 11C; Dwivedi et al., 2023).

Precocious centriole separation at M phase in selected cancer cell lines

Daughter centrioles typically disengage from the mother centrioles in early prophase, but remain associated, likely due to the surrounding PCM (Shukla et al., 2015; Cabral et al., 2013; Seo et al., 2015). The final separation of mother and daughter centrioles occurs at the end of mitosis when mitotic PCM disintegrates (Seo et al., 2015; Kim et al., 2015). However, in the absence of mitotic PCM, mother and daughter centrioles may precociously separate, potentially leading to self-amplification even in the middle of mitosis (Kim et al., 2019; Jung and Rhee, 2021). I sought to investigate whether the precocious separation of centrioles might contributes to the M-phase-specific acquisition of supernumerary centrioles in cancer cells.

Centriole separation can be assessed using the centrin-2 and CEP135 ratio, where a 2:1 ratio indicates associated centrioles, and 1:1 ratio signifies separated centrioles (Fig. 12A). As reported previously, HeLa TKO cells exhibited a high rate of precocious centriole separation at M phase (Jung and Rhee, 2021) (Fig. 12B-D). In contrast, even though centrioles in HeLa PLK4-OE cells were amplified, most remained associated throughout M phase (Jung and Rhee, 2021) (Fig. 12B-D). In these conditions, I observed prevalent precociously separated centrioles in most of the cancer cells during M phase. MDA-MB-157 displayed the highest levels, and MDA-MB-231 also exhibited considerable precocious centriole separation in M phase cells in both synchronous and asynchronous populations (Fig. 12C, D). These results indicate that precocious centriole separation is common in some cancer cell lines and may contribute to the M phase-specific generation of supernumerary centrioles.

Inverse correlation of the mitotic PCM levels with generation of supernumerary centrioles in M phase

Previous studies have reported that precocious centriole separation occurs when mitotic PCM levels are low (Kim et al., 2019). Therefore, I determined mitotic PCM levels of the cancer cells relative to the occurrence of precocious centriole separation (Fig. 13A). To accurately quantify the fluorescence intensity of PCM in a pair of centrioles, I defined a region of interest (ROI) to encompass both mother and daughter centrioles and measured the PCM intensity. In cases where the ROI did not encompass both centrioles, individual PCM intensities were measured and then combined.

PCNT levels in mitotic centrosomes exhibited high variability within the cancer cell lines, except for HeLa TKO in which *PCNT* is deleted (Fig. 13B). Notably, centrioles were frequently separated in cells with low PCNT levels, observed not only in MDA-MB-231 and MDA-MB-157 with high frequencies of centriole separation, but also in the other cancer cell lines (Fig. 13B). Similarly, the centrosome levels of CEP215, another major building block PCM protein, were found to be low in cells with separated centrioles (Fig. 13C). The close correlations between precocious centriole separation and low PCM protein levels suggest that the mitotic PCM level may be involved in the occurrence of precocious centriole separation in cancer cells.

It is known that centrioles prematurely assemble even at M phase when cells are manipulated to make centrioles precociously separated (Kim et al., 2019; Jung and Rhee, 2021). I counted centriole numbers in a natural cancer cell in relation to the centriole separation status at M phase. Consistent with previous reports, HeLa TKO cells possessed supernumerary centrioles along with precociously separated centrioles (Jung and Rhee, 2021) (Fig. 14). However, even in HeLa TKO cells, the majority maintained a normal number of centrioles in the cells with associated centrioles (Fig. 14). In such conditions, I assessed centriole amplification in cancer cells. The results showed that some cancer cells maintain supernumerary centrioles at discrete proportions irrespective of the centriole separation status (Fig. 14). However, in other cancer cell lines, such as MDA-MB-231, HCC1954, and MDA-MB-157, supernumerary centrioles were more frequent in the cells with precociously separated centrioles (Fig. 14). Altogether, these findings suggest that precocious centriole separation contributes to generation of supernumerary centrioles at M phase in selected cancer cells, such as MDA-MB-231, HCC1954 and MDA-MB-157.

Overexpression of PCM suppresses generation of supernumerary centrioles in MDA-MB-157

Even if precocious centriole separation may be a significant indication for generation of supernumerary centrioles at M phase, I know that it should not be all. It is known that prolonged treatment of aphidicolin induce precocious centriole separation, possibly activating DNA damage checkpoint (Dwivedi et al., 2023). I also observed that aphidicolin significantly increased precocious centriole separation at M phase (Fig. 11C). However, aphidicolin

treatment did not increase M-phase-specific generation of supernumerary centrioles at all, suggesting that centriole separation itself may not be sufficient to generate supernumerary centrioles at M phase (Fig. 10C, 11C). It is likely that additional conditions should be satisfied for generation of M-phase-specific supernumerary centrioles, such as reduction in PCM levels.

Previous correlative results propose that mitotic PCM may be critical for preventing generation of supernumerary centrioles at M phase in selected cancer cells. To test the hypothesis, I overexpressed PCM protein genes in the cancer cells. Consistent with earlier reports, the overexpression of PCNT into HeLa TKO significantly reduced both supernumerary centrioles and precocious centriole separation at M phase (Kim et al., 2019; Jung and Rhee, 2021) (Fig. 15A, B). Similar outcomes, though to a lesser extent, were observed in cells overexpressing CEP215 (Fig. 15A, B). In line with the previous results (Fig. 10B, 11B), the overexpression of PCNT and CEP215 had minimal effects on either the rates of precocious centriole separation or generation of supernumerary centrioles in MDA-MB-231 (Fig. 15C). However, in MDA-MB-157, overexpression of PCNT, and to a lesser extent CEP215, significantly reduced the rates of both precocious centriole separation and supernumerary centriole generation (Fig. 15D). These results strongly support the idea that the reduction in mitotic PCM can be a causative mechanism for generation of supernumerary centrioles at M phase in selected cancer cells.

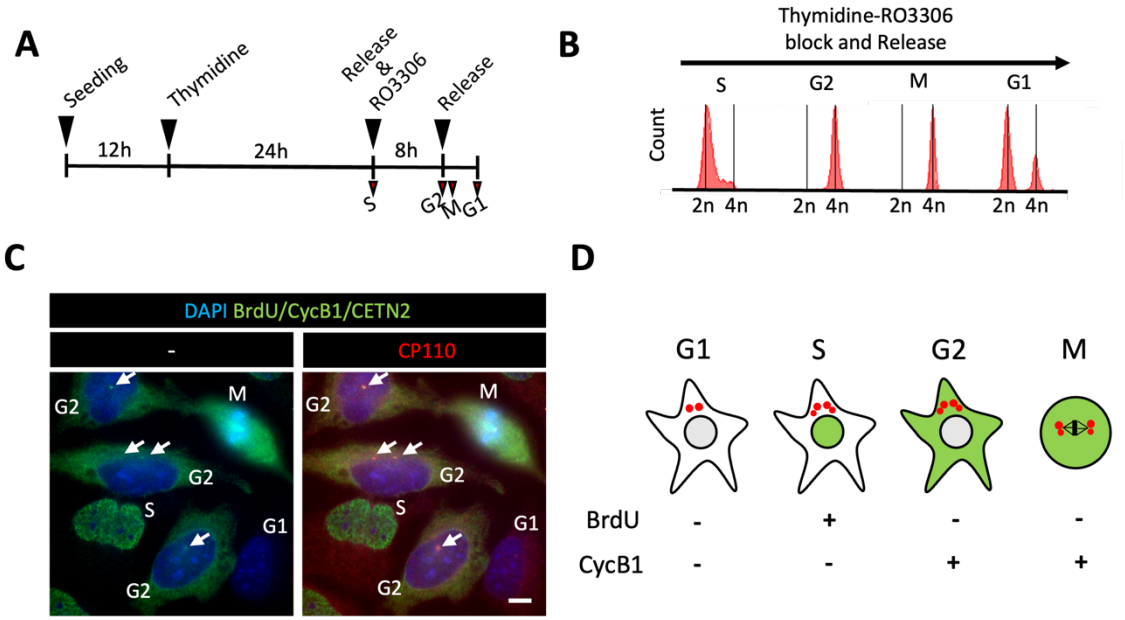

Figure 6. Establishment of methods for investigating cell cycle stage-specificity in generation of supernumerary centrioles in the cancer cell lines (A) Cells were sequentially treated with thymidine and RO3306, and released to obtain populations at specific cell cycle stages. (B) Fluorescence-activated cell sorting analysis confirmed synchronized populations of the HeLa cells at indicated cell cycle stages. (C) HeLa cells were coimmunostained with the antibodies specific to centrin-2 (green), cyclin B1 (green), bromodeoxyuridine (BrdU, green) and CP110 (red). DNA was stained with DAPI. Centrosomes are marked with arrows. Scale bar, 10 μm. (D) Graphical illustration for determination of the cell cycle stages.

A

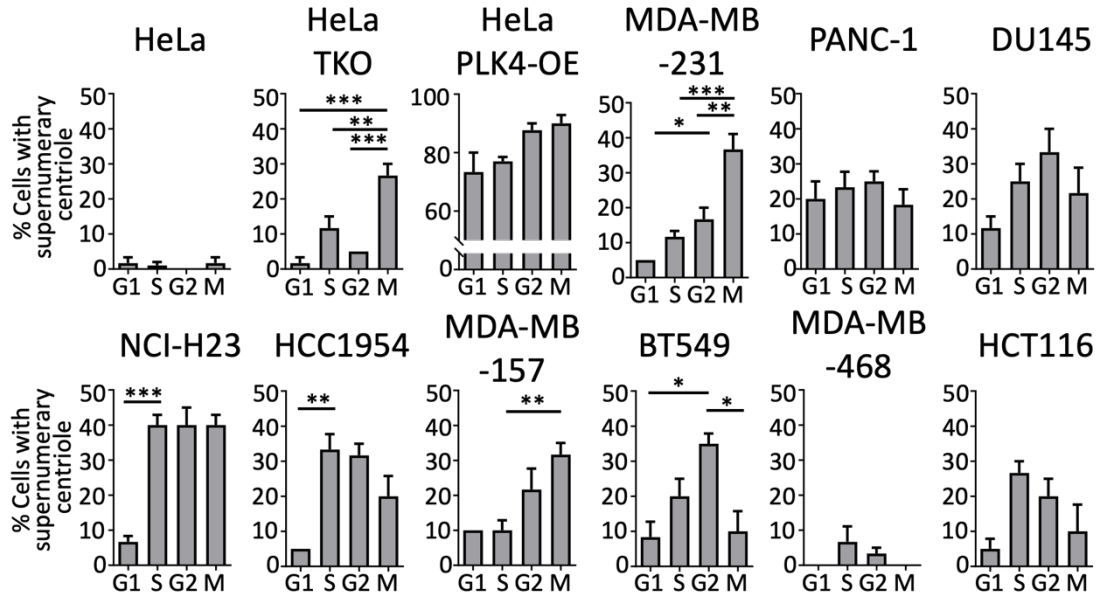

B

Cell line	Cell cycle stage for SC generation	Cell line	Cell cycle stage for SC generation
HeLa	N.A.	NCI-H23	S
HeLa TKO	M	HCC1954	S
HeLa PLK4-OE	S	MDA-MB-157	M
MDA-MB-231	M	BT549	G2
PANC-1	Constitutive	MDA-MB-468	Constitutive
DU145	Constitutive	HCT116	Constitutive

Figure 7. Cell cycle stage-specificity in generation of supernumerary centrioles in the cancer cell lines (A) The number of cells with supernumerary centrioles was counted at indicated cell cycle stages. At least 60 cells per experimental group were analyzed in 3 independent experiments. Values are means with standard deviations. Statistical significance was determined using one-way ANOVA with Newman-Keuls post hoc test (*, $P<0.05$; **, $P<0.01$; ***, $P<0.001$). (B) Summary of the cell cycle stage-specificity in generation of supernumerary centrioles in the cancer cell lines.

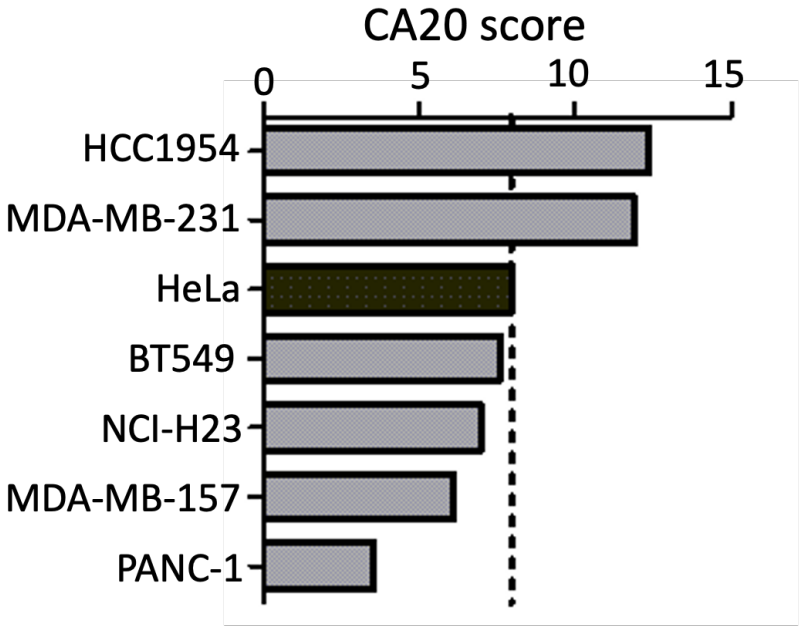

Figure 8. Analysis of centrosome duplication-associated transcript levels in cancer cells CA20 scores of the cancer cell lines were determined with known data sets of the 20 signature genes for centriole amplification (Ogden et al., 2017).

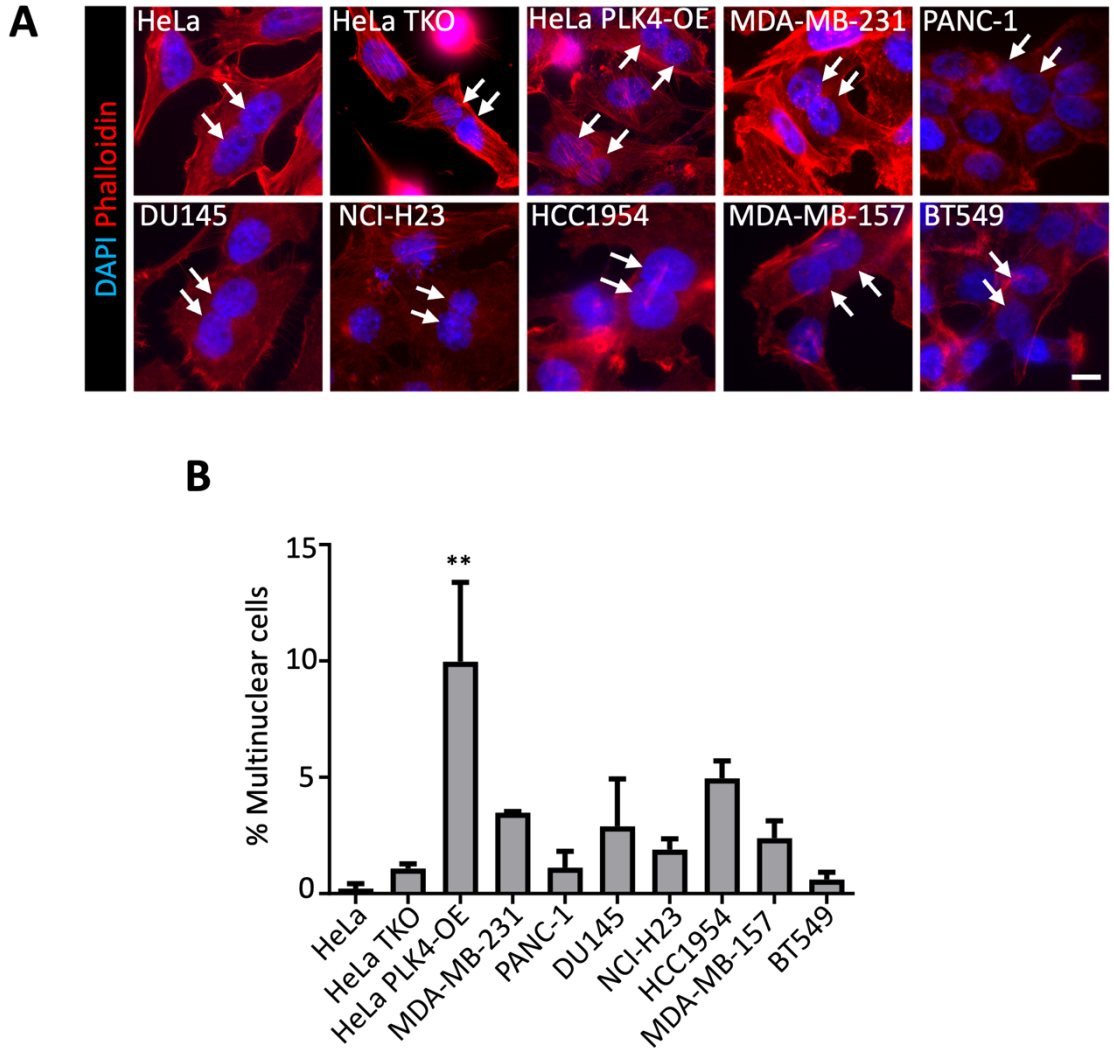

Figure 9. Analysis of cytokinesis failure rate in cancer cells (A) Asynchronous populations of the cancer cells were stained with rhodamine-conjugated phalloidin (red) and DAPI (blue). Multinuclear cells are marked with arrows. Scale bar, 10 μm. (B) The number of multinuclear cells was counted. At least 250 cells per cell line were analyzed in 3 independent experiments. Values are means with standard deviations. Statistical significance was determined using one-way ANOVA with Tukey post hoc test (**, $P<0.01$).

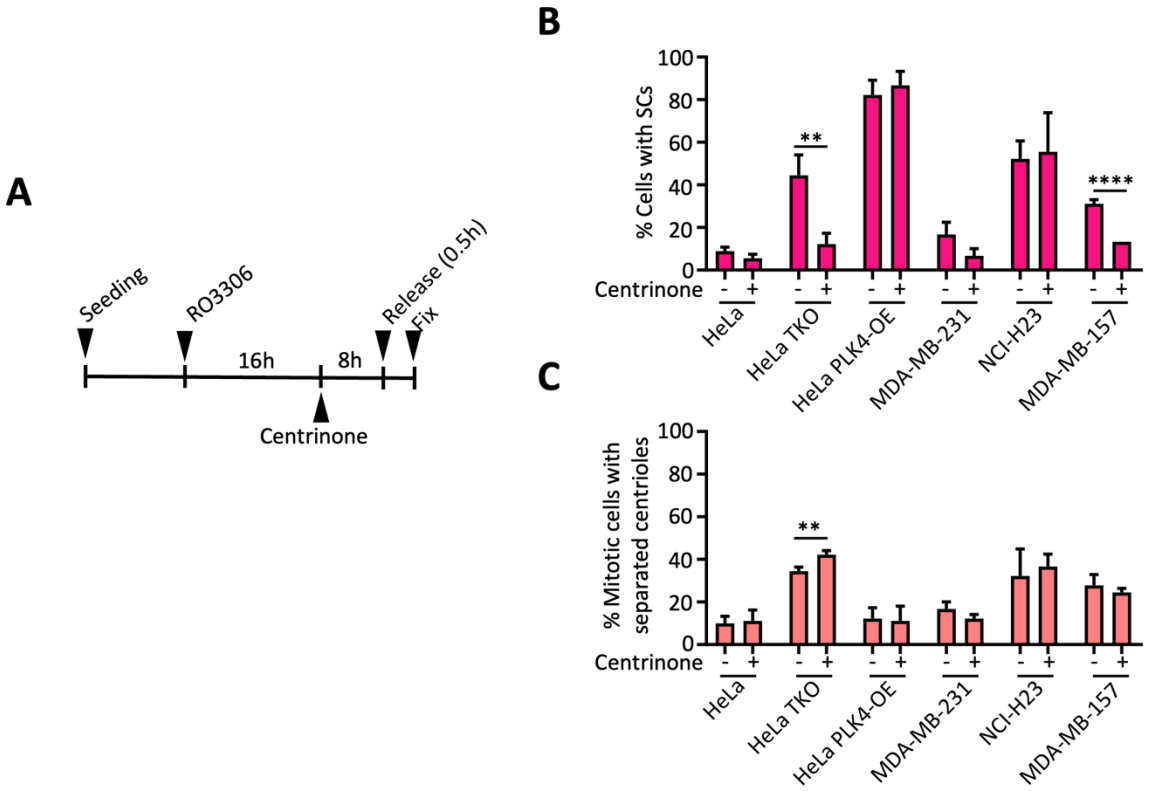

Figure 10. Inhibition of M-phase-specific supernumerary centrioles with centrinone with R03306-release method (A) Cell cycle was arrested at G2 phase with RO3306 for 24 h, and subsequently released for 0.5 h. PLK4 activity was inhibited by centrinone for 8.5 h at the end of the culture. The cells at M phase were coimmunostained with centrin-2 and CEP135 antibodies. (B, C) The numbers of cells with supernumerary centrioles (B) and separated centrioles (C) were counted. (B,C) At least 90 cells per experimental group were analyzed in 3 independent experiments. Statistical significance was determined using unpaired two-tailed t-test (**, P<0.01; ****, P<0.0001).

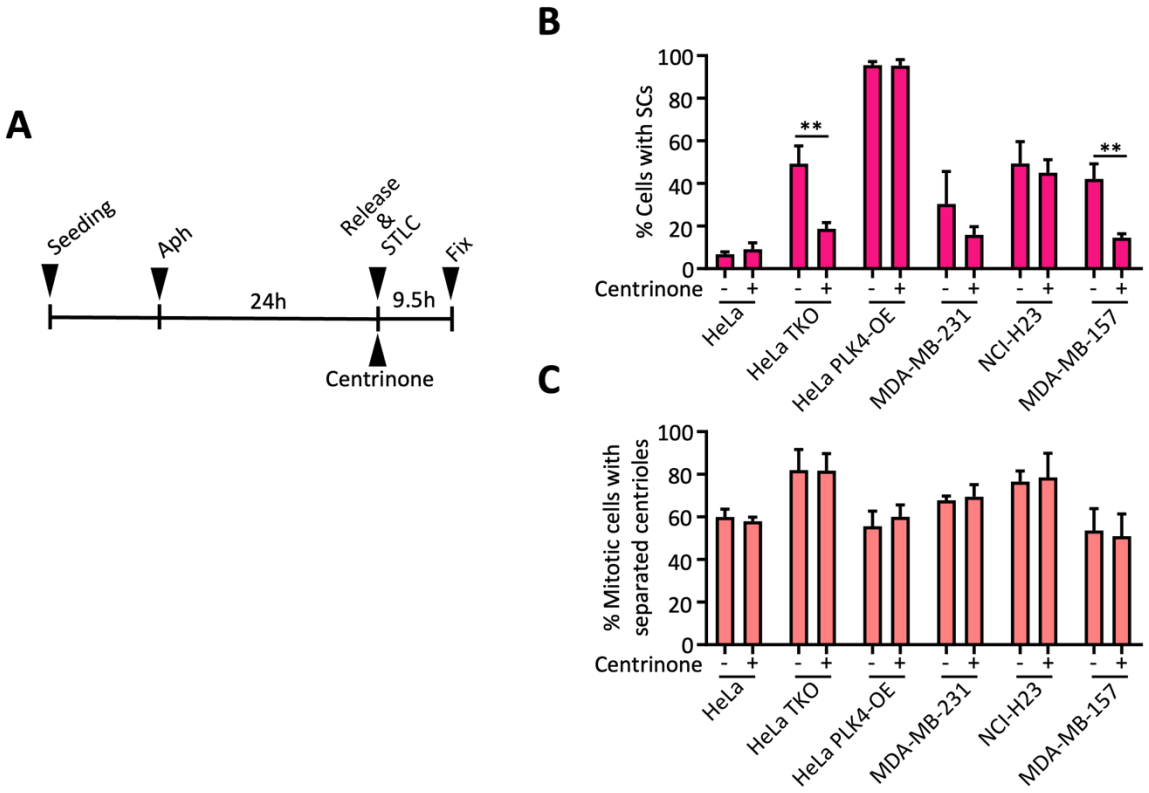

Figure 11. Inhibition of M-phase-specific supernumerary centrioles with centrinone with Aphidicoline and STLC-arrest method (A) Cell cycle was arrested at S phase with aphidicolin for 24 h, and subsequently at prometaphase with STLC for 9.5 h. PLK4 activity was inhibited by centrinone for 9.5 h at the end of the culture. The cells at prometaphase were coimmunostained with centrin-2 and CEP135 antibodies. (B, C) The numbers of cells with supernumerary centrioles (B) and separated centrioles (C) were counted. (B,C) At least 90 cells per experimental group were analyzed in 3 independent experiments. Statistical significance was determined using unpaired two-tailed t-test (**, $P<0.01$; ****, $P<0.0001$).

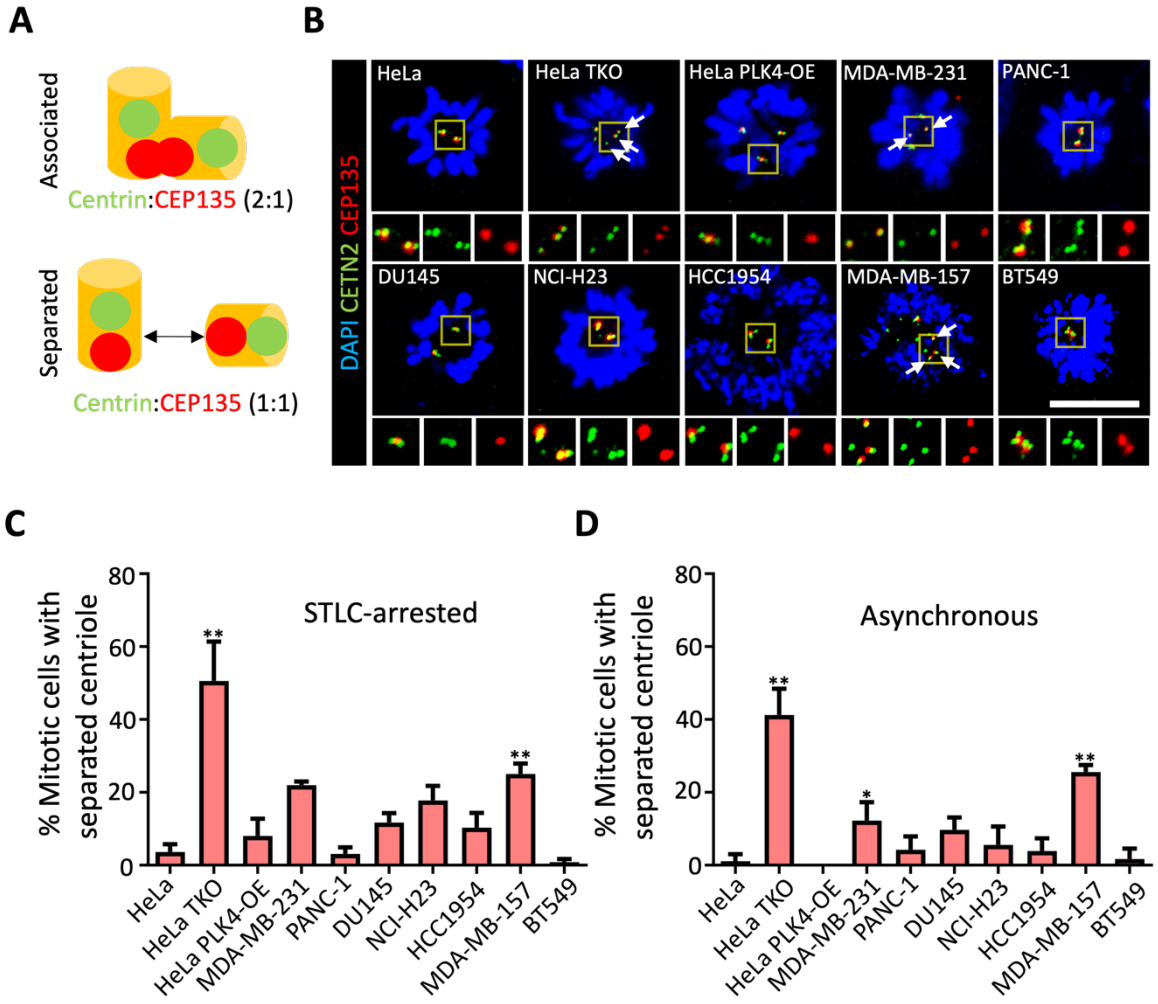

Figure 12. Precocious centriole separation in selected cancer cell lines (A) Association and separation of centrioles were determined with the ratio of centrin-2 and CEP135 foci. (B) The STLC-treated M phase cells were coimmunostained with centrin-2 (green) and CEP135 (red) antibodies. DNA was stained with DAPI. Separated centrioles are marked with arrows. Scale bar, 10 μm. (C, D) The M phase cells were obtained with the STLC treatment (C) or from asynchronous populations (D). The number of cells with separated centrioles were counted at indicated cell lines. At least 90 cells per each cell line were analyzed in 3 independent experiments. Values are means with standard deviations. Statistical significance was determined using one-way ANOVA in comparison to the HeLa cells (*, $P<0.05$; **, $P<0.01$).

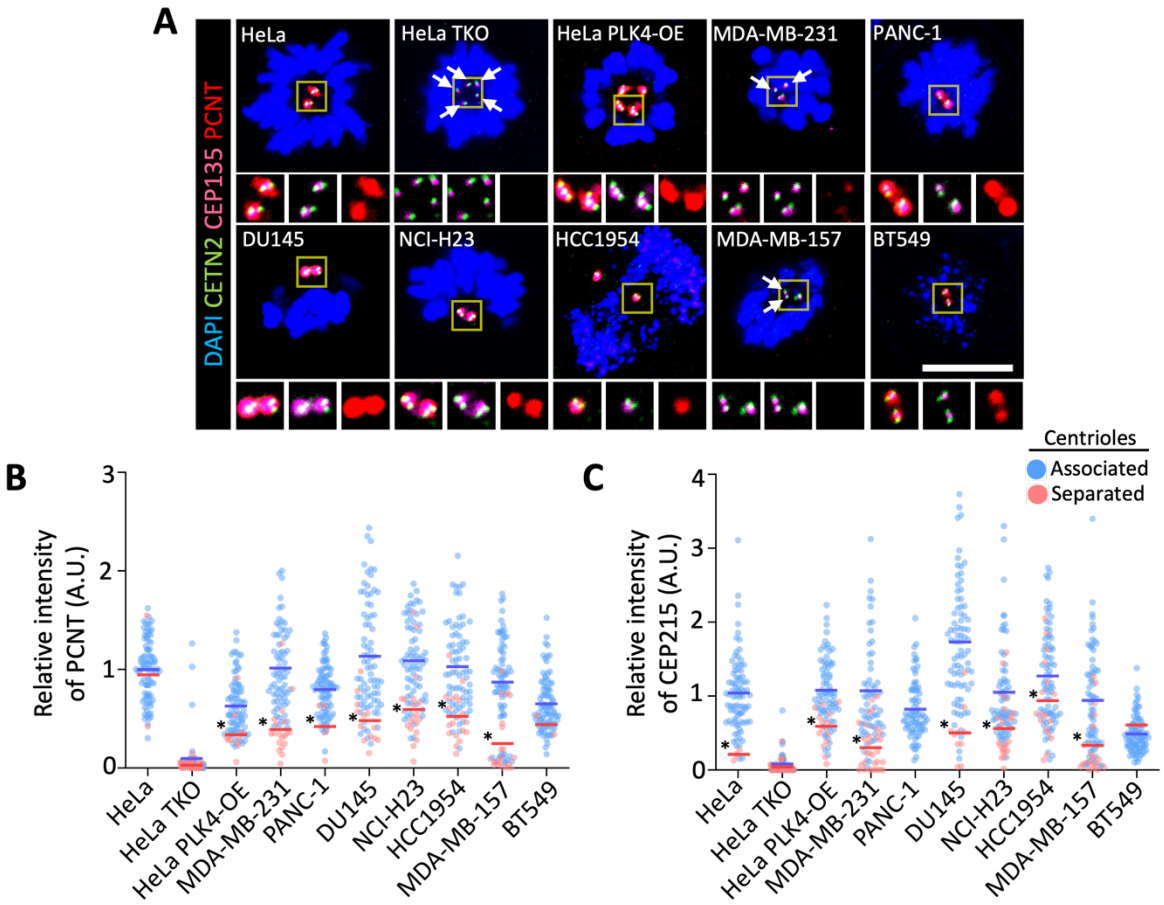

Figure 13. Inverse correlation of the mitotic PCM levels with centriole separation and in selected cancer cell lines (A) The STLC-treated M phase cells were coimmunostained with centrin-2 (green), CEP135 (magenta) and PCNT (red) antibodies. DNA was stained with DAPI. Separated centrioles are marked with arrows. Scale bar, 10 μm. (B, C) Centriole intensities of PCNT (B) and CEP215 (C) were determined and indicated with the scatter plots. Blue and pink dots indicate the associated and separated centrioles, respectively. Mean values of the associated and separated centrioles were marked with the blue and pink bars. At least 79 cells per experimental group were analyzed in 3 independent experiments. Statistical significance was determined using unpaired two-tailed t-test (*, P<0.05).

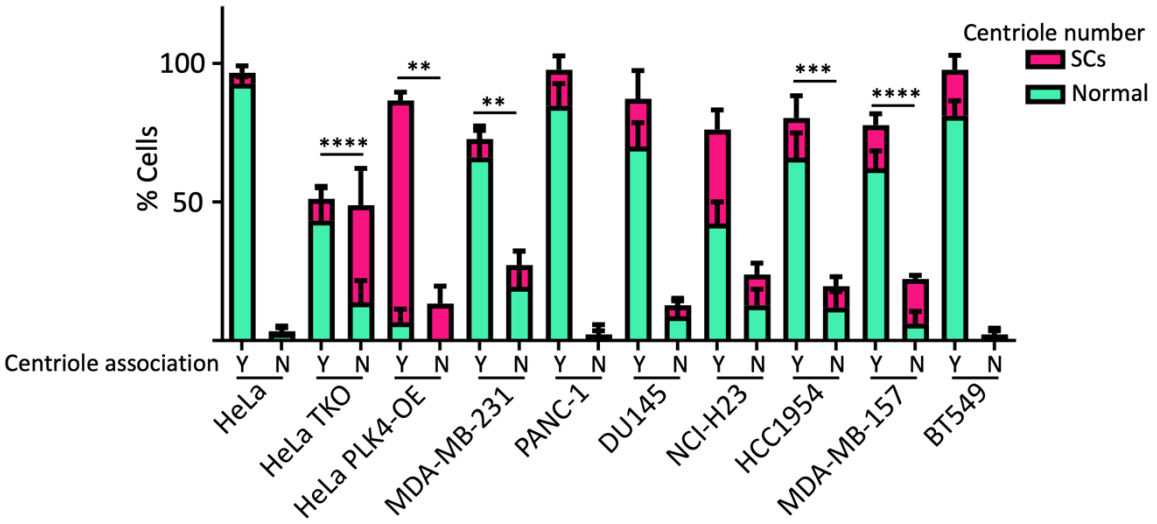

Figure 14. Correlation of centriole separation and acquisition of supernumerary centrioles in selected cancer cell lines The number of cells with supernumerary centrioles was counted within the centriole association and separation groups and the proportions of the cells with supernumerary centrioles were compared. At least 169 cells per experimental group were analyzed in 6 independent experiments. Statistical significance in the proportions of cells with supernumerary centrioles was determined using unpaired two-tailed t-test (*, $P<0.05$; **, $P<0.01$; ***, $P<0.001$).

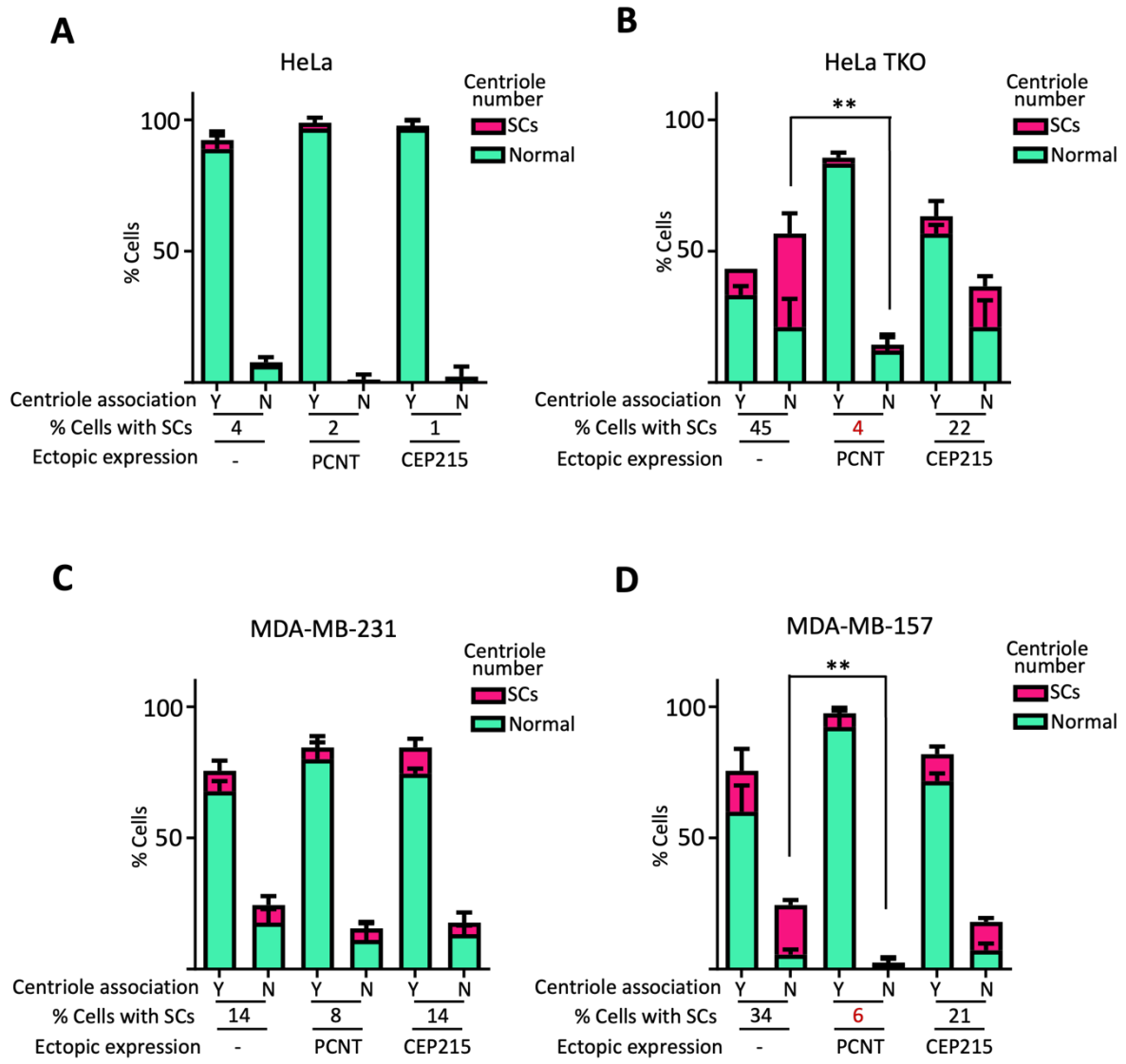

Figure 15. Suppression of centriole separation and amplification through PCM overexpression in a selected cancer cell line FLAG-PCNT and FLAG-CEP215 were ectopically expressed in HeLa (A), *TP53*;*PCNT;CEP215* KO HeLa (HeLa TKO) (B), MDA-MB-231 (C) and MDA-MB-157 (D) cells. The STLC-treated M phase cells were coimmunostained with FLAG, centrin-2 and CEP135 antibodies. The number of cells with supernumerary centrioles was counted within the centriole association and separation groups. Values are means with standard deviations. At least 90 cells per experimental group were analyzed in 3 independent experiments. Statistical significance in the proportions of cells with supernumerary centrioles was determined using one-way ANOVA with Tukey post hoc test (*, $P<0.05$; **, $P<0.01$).

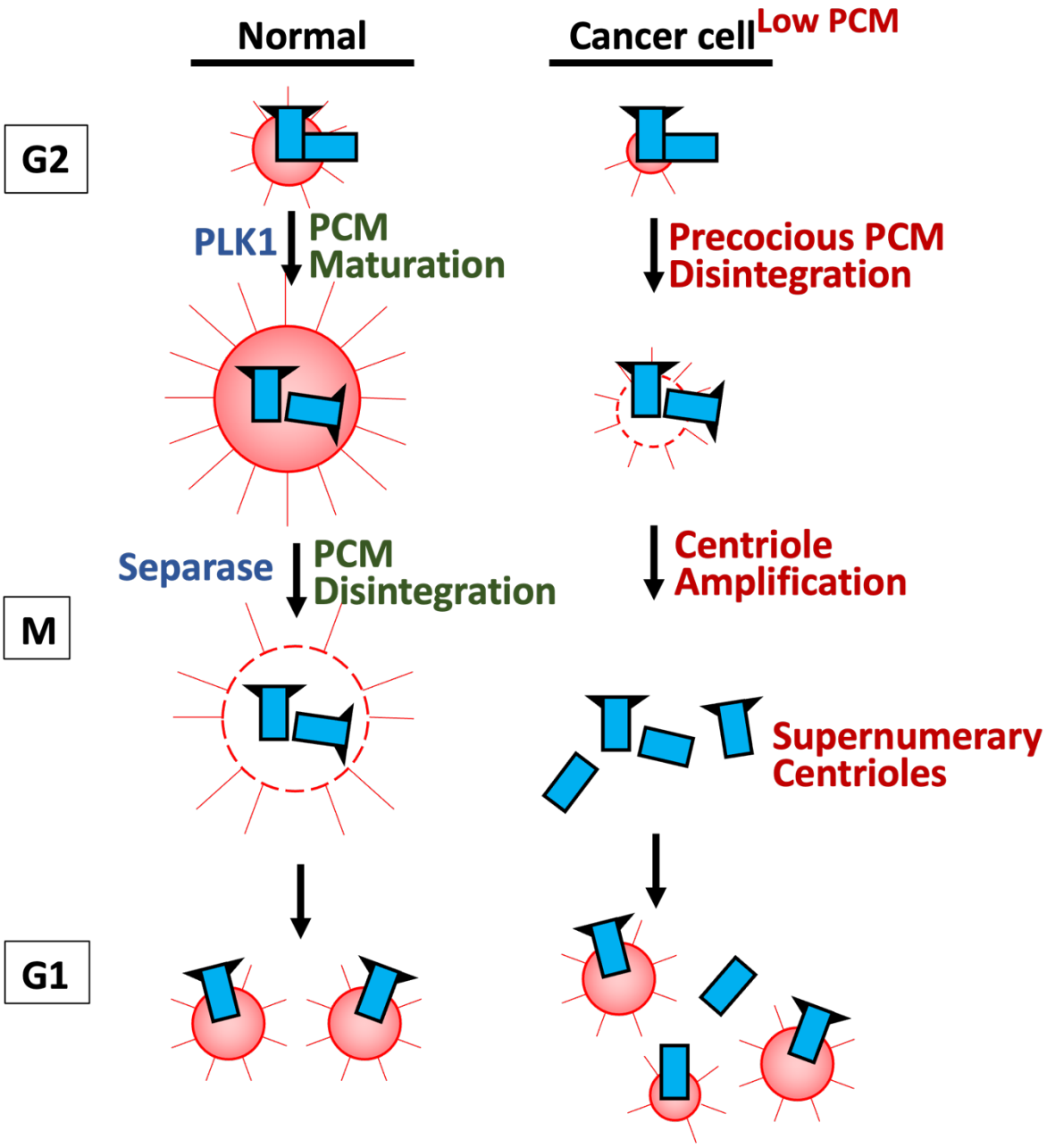

Figure 16. Model for M-phase-specific supernumerary centriole generation in cancer cells
In normal cells, daughter centrioles disengage from the mother centrioles during M phase but remain associated surrounded by mitotic PCM. When the cells exit mitosis, PCM is disintegrated, and mother and daughter centrioles separate to form two independent centrosomes. In cancer cells with low PCM, mother and daughter centrioles precociously separate to each other, leading to centriole amplification during the M phase. These extra centrioles may become supernumerary centrioles.

DISCUSSION

In this study, I searched for cancer cell lines in which supernumerary centrioles are generated at M phase, independent of scheduled daughter centriole assembly at S phase. Among a dozen cancer cell lines examined, I found that MDA-MB-157 and MDA-MB-231 acquire supernumerary centrioles specifically at M phase. PLK4 activity is necessary for M-phase-specific generation of supernumerary centrioles. The M-phase-generated supernumerary centrioles can be detected with two different antibodies which recognize the core and distal end of centriole, suggesting they are more or less intact. My study reveals that M-phase-specific generation of supernumerary centrioles genuinely occurs in selected natural cancer cells.

It was previously revealed that M-phase centriole amplification occurs in *PCNT* KO HeLa cells (Kim et al., 2019). The number of M-phase-generated centrioles were even enhanced when *CEP215* was co-deleted, indicating that intact PCM is critical for prevention of M-phase centriole generation (Jung and Rhee, 2021). Centrioles in interphase cells are surrounded by PCM of the characteristic toroid structure (Lawo et al., 2012; Mennella et al., 2012). When the cells enter the M phase, centrosomes robustly accumulate additional PCM proteins to organize microtubules for mitosis (Lawo et al., 2012; Loncarek et al., 2010). Another crucial function of mitotic PCM may be to prevent centriole amplification by maintaining the mother and daughter centrioles to be associated during mitosis (Kim et al., 2019). When mitotic PCM is not sufficiently accumulated at the centrosomes, mother and daughter centrioles precociously separate at the M phase (Karki et al., 2017; Kim et al., 2019; Jung and Rhee, 2021). Indeed, in the *PCNT* KO HeLa cells, reduction of mitotic PCM leads to precocious centriole separation, resulting in unscheduled centriole assembly (Kim et al., 2019; Jung and Rhee, 2021; Press et al., 2019).

In this study, I observed that a fraction of the cancer cells with low centrosome levels of PCNT and CEP215 frequently exhibited precociously separated centrioles at the M phase, suggesting that precocious centriole separation is a prevalent event in most cancer cells with low mitotic PCM levels. Furthermore, in the case of MDA-MB-157, overexpression of PCNT reduced the number of cells with precociously separated centrioles and eventually those with supernumerary centrioles (Fig. 15). These results support the proposal that reduction of mitotic

PCM is a working mechanism to generate supernumerary centrioles at M phase in cancer cells (Fig. 16). However, it is also the case that precocious centriole separation itself may not be sufficient to induce centriole amplification. For example, aphidicolin may induce precocious centriole separation but does not result in supernumerary centrioles at M phase (Fig. 11). It is likely that cancer cells need additional conditions for generation of supernumerary centrioles. The dynamics of PCNT in normal cycling cells might provide a clue. During telophase, PCNT undergoes cleavage by separase to liberate two centrioles held together during mitosis. However, even in this condition when two centrioles are liberated, centriole amplification does not take place. It is possibly due to remaining PCNT population building toroid structure which presumably is not cleaved by separase. It is worthwhile to investigate the role of toroidal PCNT in the further study.

Also, it remains to be investigated why a fraction of cancer cells include reduced amount of PCM at their spindle poles. One possible cause may be mutations in PCM protein genes, exemplified in the *TP53;PCNT;CEP215* triple KO cells. However, it is unlikely that mutations are the predominant cause for the reduction of mitotic PCM in many cancer cells, as only subpopulations of the examined cancer cell lines showed reduced levels of centrosome PCNT and CEP215, two major PCM proteins. My immunoblot analyses further indicated comparable expression levels of PCNT and CEP215 across the examined cancer cell lines (data not shown).

Another scenario may be related to checkpoint arrest of cancer cells at G2 and M phases (Shukla et al., 2015; Balczon et al., 1995; Inanç et al., 2010; Loncarek et al., 2010). Prolonged cell cycle arrest at G2 and M phases might deplete the mitotic PCM levels of cancer cells, leading to the liberation of centrioles from PCM (Karki et al., 2017; Cabral et al., 2013; Seo et al., 2015). In addition, mitotic PCM may be prematurely degraded by uncontrolled separase activity in cancer cells. It is known that an initial event for mitotic PCM disintegration involves separase specifically cleaving PCNT (Dodson et al., 2004; Lee et al., 2012; Matsuo et al., 2012). The activity of separase remains silent until APC/C^{Cdc20} degrades securin, an inhibitory subunit (Lu et al., 2014). Apparently, APC/C activity is not strictly regulated in many cancer cells (Lawo et al., 2012; Mennella et al., 2012; Dictenberg et al., 1998). Consistent with this, precocious separase activation before anaphase onset is known to occur in several cancer cell lines (Shindo et al., 2021). Mild replication stress also induces G2 arrest with concomitant

sub-critical PLK1 activity, priming PCNT for separase-dependent degradation at G2 phase (Dwivedi et al., 2023).

This study represents the first report that supernumerary centrioles may be generated at M phase in cancer cells with reduced levels of PCM proteins. Therefore, further investigations are necessary to explore the involvement of PCM proteins in tumor progression in specific cancer cells.

Chapter II.

Characterization of early-stage cysts in the ciliopathic kidneys of *Cep90* KO mice

ABSTRACT

Cilia serve as subcellular organelles for signal reception and cell motility. *Cep90* is essential for ciliogenesis, and mutations in it lead to Joubert syndrome in humans, characterized by developmental defects including polycystic kidney disease. However, it remains elusive how dysfunction of Cep90 manifests pathological outcomes. Here, I generated kidney-specific *Cep90* knockout (KO) mice and investigated their kidney phenotypes. Renal cystogenesis initiated concomitantly with cilia ablation resulting from absence of distal appendages in *Cep90* KO kidney cells. Furthermore, I dissected renal cystogenesis into early and late stages, depending on the composition of renal epithelial cells. Early cysts are composed of both ciliated and non-ciliated cells, whereas large cysts exclusively comprised non-ciliated epithelial cells. mTOR was preferentially activated in non-ciliated cells of early-stage cysts, while nuclear YAP translocation commenced at early stages and persisted until late stages, irrespective of cilia presence. Based on these observations, I propose that renal cystogenesis progresses through sequential activations of specific signaling pathways in *Cep90* KO kidneys.

INTRODUCTION

Primary cilia are subcellular organelles crucial for development and homeostasis, transducing a diverse array of extracellular stimuli (Derderian et al., 2023). Dysfunctional cilia typically lead to pleiotropic phenotypes, indicative of their widespread distribution and varied functionality. More than 35 human genetic diseases, collectively termed ciliopathies, have been associated with over 180 established ciliopathy-related proteins (McConnachie et al., 2021). In the kidney, cilia on epithelial cells of the renal tubules extend into the lumen to perform sensory functions. Deletion of cilia on renal epithelium is sufficient to trigger cystogenesis, a hallmark of polycystic kidney disease (PKD) (Davenport et al., 2007; Lin et al., 2003; Pazour et al., 2000). Indeed, several cilia-related genes have been discovered in the search for PKD genes.

PKD represents a group of monogenic disorders characterized by renal cyst formation (Harris and Torres, 2009). Cysts originate from tubular epithelial cells due to abnormally high rates of misoriented cellular proliferation, expression of a secretory phenotype, fluid accumulation, and altered protein sorting (McConnachie et al., 2021). Over time, cysts displace renal parenchyma, compress microvasculature, and contribute to PKD-associated kidney injury, which in turn stimulates systemic inflammatory changes (Chapin and Caplan, 2010).

The genetic etiology of PKD has been extensively studied. Autosomal-dominant polycystic kidney disease (ADPKD) is the most prevalent form, affecting approximately 1 in every 400–1000 individuals (Ong et al., 2015). Mutations in *polycystin-1* and *polycystin-2* account for the majority of ADPKD cases (Ma, 2021). The ‘two-hit’ hypothesis has been proposed to elucidate the genetic mechanism underlying focal nature of cystogenesis in ADPKD. According to this hypothesis, inheritance of a single mutant allele from one parent, followed by a somatic second-hit on the normal allele of the same gene, leads to gene inactivation at the cellular level, initiating cyst formation (Wu et al., 1998; Watnick et al., 1998; Tan et al., 2018). Autosomal-recessive polycystic kidney disease (ARPKD) is also recognized, with mutations identified in the *polycystic kidney and hepatic disease 1* gene (Zerres et al, 1994; Ma, 2021).

Cep90 was initially known as a secretory protein named progesterone immunomodulatory binding factor 1 (Pibf1) which plays crucial roles in modulation of

maternal immune system and trophoblast development (Szekeres-Bartho et al., 2018; Lee et al., 2024). Cep90 is also characterized as a centrosome protein localized at centriolar satellites and the distal end of centrioles (Kim et al., 2011; Kodani et al., 2015; Kumar et al., 2021). It is involved in distal appendage assembly, critical for positioning the mother centriole at the cellular membrane for cilia formation (Kumar et al., 2021). Notably, ciliogenesis fails in the absence of Cep90 (Kim et al., 2012; Kumar et al., 2021). Mutations in *Cep90* results in Joubert syndrome, which encompasses various ciliopathy-associate abnormalities, including PKD (Wheway et al., 2015; Hebbar et al., 2018).

In this study, I investigate kidney phenotypes of kidney-specific *Cep90* knockout (KO) mice. I demonstrate renal cystogenesis concurrent with cilia ablation in tubular epithelial cells of *Cep90* KO kidneys. By leveraging the gradual onset of cystogenesis in *Cep90* KO mice, I dissect the direct consequences of cilia ablation and unravel the molecular pathways underlying cystogenesis progression. My findings showed that cystogenesis proceeds through sequential activation of specific signaling pathways in the absence of Cep90.

MATERIALS AND METHODS

Animals

All animal experiments were performed under the Korean Ministry of Food and Drug Safety guidelines. Experimental procedures were reviewed and approved by the Institutional Animal Care and Use Committees (IACUC) of Asan Institute for Life Sciences (2019-12-217) and of Seoul National University (SNU-211112-3-11). All mice were maintained in the specific pathogen-free facility of the Laboratory of Animal Research at Asan Medical Center (AMCLAR). The floxed *Cep90/Pibf1* mice was described previously (Lee et al., 2024). *Cdh16-Cre* (B6;129-Tg(Cdh16-cre)1Spe/J, 017968) mice were purchased from the Jackson Laboratory (Bar Harbor, ME, USA). All mice used in this study were PCR-genotyped with primer pairs as follows:

Gene	Target	Forward (5′→3′)	Reverse (5′→3′)	Size (bp)
Cep90	Intron 1	CTTGGTAACTCACGCAAGGAT	TCAAACTCAAGGAGAGGTTGATT	WT, 497; floxed, 531
	Intron 17	AGTGTAGTGTCTTCAAGATTCATTC	CCTCCCAGCTCCCTGTAGT	WT, 286; floxed, 320
Cdh16-Cre Tg	Cre transgene	GCAGATCTGGCTCTCCAAAG	AGGCAAATTTTGGTGTACGG	420
	Internal control	CAAATGTTGCTTGTCTGGTG	CAAATGTTGCTTGTCTGGTG	200

Tissue collection

Mice were euthanized in a CO_2 chamber. Cardiac perfusion was performed with PBS. Freshly isolated kidneys were fixed in 4% paraformaldehyde overnight at 4°C, paraffin-embedded and sectioned at either 5-μm or 20-μm thickness. For qRT-PCR, freshly isolated kidneys were immersed in TRIzol reagent (Invitrogen) and total RNA was extracted according to the manufacturer's instructions.

Serum Biochemical Analysis

The wild-type and mutant mice were anesthetized by isoflurane inhalation (Terrell Isoflurane, Piramal critical care, Bethlehem, USA), and blood samples were taken from the abdominal inferior vena cava (IVC). After incubating them at room temperature for 30 min, the serum was isolated by centrifugation of coagulated whole blood at 3,000 rpm for 10 min.

Serum alanine aminotransferase (ALT), aspartate aminotransferase (AST), alkaline phosphatase (ALP), albumin, glubulin, bilirubin, creatine, and total protein levels were measured using an automatic analyzer (Hitachi 7180, Tokyo, Japan).

Antibodies

Rabbit anti-Cep90 (IHC, 1:100; ICC, 1:200; IB, 1:1000; Kim et al., 2011), and rabbit anti-Cep164 (IHC, 1:100, Kim et al., 2019) were previously described. Rabbit anti-β-catenin (IHC, 1:100) was a kind gift from William Nelson (Stanford University).

Rabbit anti-Arl13b (Proteintech, 17711-1-AP; IHC, 1:100), rabbit anti-Cep83 (Sigma-Aldrich, HPA038161; IHC, 1:100), rabbit anti-p-S6RP (Cell Signaling Technology, 2211; IHC, 1:200), rabbit anti-p-mTOR (Cell Signaling Technology, 2971; IHC, 1:50), rabbit anti-Ki-67 (Abcam, ab15580; IHC, 1:100), rabbit anti-YAP (Proteintech, 135841-1-AP; IHC, 1:200; ICC, 1:200), rabbit anti-γ-tubulin (Abcam, ab11317; ICC, 1:1000), rabbit anti-p-FAK (Cell Signaling Technology, 8556; IHC, 1:200), mouse anti-Aqp1 (Santa curz, sc-32737; IHC, 1:100), mouse anti-Aqp2 (Santacruz, sc-515770, IHC, 1:200), mouse anti-Calb1 (Abcam, ab82812; IHC, 1:500), mouse anti-acetylated tubulin (Sigma-Aldrich, T6793; IHC, 1:100; ICC, 1:200), mouse anti-γ-tubulin (Abcam, ab11316; IHC, 1:100), mouse anti-centrin2 (Millipore, 04-1624; ICC, 1:500), mouse anti-polyglutamylated tubulin (Adipogen, AG-20B-0020; ICC, 1:200), and mouse anti-Gapdh (Invitrogen, AM4300; IB, 1:10000) were purchased from commercial suppliers.

Alexa Fluor 488-, 594-, and 647-conjugated secondary antibodies were purchased. For immunohistochemistry with 3,3'-diaminobenzidine (DAB) as chromogen, Vectastain ABC-HRP kit (Vector Laboratories, PK-4001) was applied. Anti-mouse IgG-HRP (Sigma-Aldrich, A9044; IB, 1:1000) and anti-rabbit IgG-HRP (Millipore, AP132P; IB, 1:1000) were used as secondary antibodies for the immunoblot analyses. In case of triple staining, Zenon labeling kits (Invitrogen, Z25005 and Z25302) was applied.

.

Histological analysis

For H&E staining, kidney sections were rehydrated and stained using an automatic staining machine (Leica, Leica ST5010 Autostainer XL). Stained sections were mounted with Limonene mount medium (Electron Microscopy Sciences, 17987-01). Images were acquired with conventional light microscope using 40× objectives (Olympus, BX51) and EVOS FL Auto2 using 4× and 20× objectives (ThermoFisher, Waltham, MA, USA) for tile-scanning of the whole kidney sections. Measuring the surface area of cysts were performed with tile-scanned kidney images and image analysis was conducted by manually annotating the size of each cyst and applying measuring tool in ImageJ (National Institute of Health).

For immunohistochemistry, kidney sections were rehydrated and subjected to antigen retrieval with the Tris-EDTA buffer (10 mM Tris pH 9.0, and 1mM EDTA) and citrate buffer (10mM sodium citrate pH 6.0, and 0.1% Tween 20) in a microwave for 25-35 min. The sections were then permeabilized in 0.1% PBST, blocked in 3% BSA in PBST, and incubated with primary antibodies for 24 h followed by the secondary antibodies for 1 h. After nuclear staining with DAPI, the samples were observed using a confocal laser-scanning microscope system equipped with 40×/1.2 NA korr C-Apochromat objective lens or 100×/1.4 NA Plan-Apochromat objective lens and a fluorescence microscope (Olympus; IX51) equipped with 60×/1.35 NA UPlanSApo objective lens and with a CCD camera (Qimaing, Qicam Fast 1394).

Confocal 2D images were analyzed in ImageJ or Zen lite software (Carl Zeiss). In case of 3D imaging, kidney sections were z-stacked and analyzed by manually capturing the luminal view of each cell in ICY software and drawing and measuring the surface area in ImageJ (de Chaumont et al., 2012).

Cell culture, transfections and plasmids

The hTERT-RPE1 cells were cultured in Dulbecco's modified eagle medium/Nutrient mixture F-12 (F12/DMEM) supplemented with 10% FBS at 37°C under 5% CO_2. To induce ciliogenesis, the cells were transferred to a medium supplemented with 0.1% FBS and cultured for 48 h.

To generate *Cep90* KO RPE1 cells, gRNA targeting *Cep90* was cloned into the plasmid pSpCas9(BB)-2A-Puro (PX459) V2.0 (Plasmid #62988). *Cep90* gRNA (5'-GAT GAG GAA ATA TCA TCC GT-3') was adopted from Kumar et al. (2021). The donor vector was

digested with BbsI and ligated annealing gRNA using T4 DNA ligase (Roche, 10481220001). RPE1 cells were transfected using Lipofectamine3000 (Invitrogen) and selected with 4 μg/ml puromycin (Sigma-Aldrich, P8833) for 48 h.

Immunocytochemistry

For immunofluorescence analysis, the cells were cultured on coverslips. The cells were fixed either with -20°C methanol for 10 min or with 4% PFA for 12 min, washed with PBS three times, permeabilized with PBST (PBS with 0.1% Triton X-100) for 10 min, incubated with a blocking solution (PBST with 3% bovine serum albumin) for 30 min at room temperature. The cells were then incubated with the primary antibodies for 1 h, washed with PBST three times, incubated with the secondary antibodies for 30 min, washed with PBST twice, stained with 4,6-diamidino-2-phenylindole (DAPI) for 2 min, and washed twice with PBST. The coverslips were mounted on a slide with ProLong Gold antifade reagent (Life Technologies, P36930).

Acquiring the images and counting the number of fluorescent signals were performed using a fluorescence microscope (Olympus; IX51) equipped with 60×/1.35 NA UPlanSApo objective lens and with a CCD camera (Qimaing, Qicam Fast 1394). Intensities of the fluorescent signals were analyzed using ImageJ. For nuclear YAP quantification, nuclear/cytoplasmic ratios of YAP mean fluorescence intensities (N/C ratio) were determined to define YAP distribution patterns as nuclear (N/C ratio > 1.2) (Kim et al., 2015).

Immunoblotting

The cells were lysed on ice for 10 min with RIPA buffer (150 mM NaCl, 1% Triton X-100, 0.5% sodium deoxycholate, 0.1% SDS, 50 mM Tris-HCl at pH 8.0, 10 mM NaF, 1 mM Na_3VO_4, 1 mM EDTA, and 1 mM EGTA) containing a protease inhibitor cocktail (P8340; Sigma-Aldrich) and centrifuged with 12,000 rpm for 10 min at 4°C. The supernatants were mixed with 4×SDS sample buffer (250 mM Tris-HCl at pH 6.8, 8% SDS, 40% glycerol, and 0.04% bromophenol blue) and 10 mM DTT (0281-25G; Amresco). Mixtures were boiled for 5 min. The protein samples were loaded in SDS polyacrylamide gels (3% stacking gel and 4–10%

separating gel), electrophoresed, and transferred to Protran BA85 nitrocellulose membranes (10401196; GE Healthcare Life Sciences). The membranes were blocked with blocking solution (5% nonfat milk in 0.1% Tween 20 in TBS) for 2 h, incubated with primary antibodies diluted in blocking solution for 16 h at 4°C, washed four times with TBST (0.1% Tween 20 in TBS), incubated with secondary antibodies in blocking solution for 30 min, and washed again. To detect the signals of secondary antibodies, the ECL reagent (ABfrontier, LF-QC0101) and X-ray films (Agfa, CP- BU NEW) were used.

qRT-PCR

Extracted total RNA was subjected to reverse transcription with random hexamers. PCR products were prepared using TOPreal SYBR Green qPCR premix (Enzynomics, RT500), and Real-time PCR was carried out with QuantStudio 3 Real-Time PCR system (Applied Biosystems) piloted by Design and Analysis 2 software. The data were plotted on relative expressions of *c-Myc*, *Cyr61*, *Ctgf*, and *Amotl2* normalized to *Gapdh* were calculated using the 2ΔΔC(t) method. The primer sequences are as follows:

Gene	Forward (5′→3′)	Reverse (5′→3′)	References
c-myc	CCTTTGGGCGTTGGAAACC	CGTCGCAGATGAAATAGGG	Cai et al, 2018
Cyr61	GCTCAGTCAGAAGGCAGACC	GTTCTTGGGGACACAGAGGA	
Ctgf	AGTGTGCACTGCCAAAGATG	CCAGGCAAGTGCATTGGTAT	
Amotl2	AGGGACAATGAGCGATTGCAG	CCTCACGCTTGGAAGAGGT	
Gapdh	CCCAATGTGTCCGTCGTGGAT	TGTAGCCCAAGATGCCCTTCAG	

Statistical analysis

Data sample sizes were determined from prior experience. I was not blinded to allocation during experiments and outcome of assessment. Statistical significance was

determined using an unpaired two-tailed t-test, one-way analysis of variance (ANOVA) and Kruskal-Wallis test on Prism 8 (GraphPad software). All values are given as mean ±SD except for the cases where individual data were presented and described in legends. P values indicated on figure follow the *P<0.05, **P< 0.01, ***P< 0.001, ****P<0.0001.

RESULTS

Renal cyst formation in *Cep90* KO mice

Previous works revealed two very different functions of Cep90/Pibf1 as a centrosome component (Kim et al., 2011) and a signaling molecule (Szekeres-Bartho et al., 2018). In order to determine which role of Cep90/Pibf1 is played in the kidney, I crossed *Cep90*-floxed mice with renal epithelial cell-specific *Cdh16-Cre* transgenic mice (Shao et al., 2002). The resulting *Cep90*$^{fl/fl}$*;Cdh16-Cre* mice (hereafter referred to as *Cep90* KO) lost a 149 kb fragment encompassing the majority of the protein coding region (Fig. 17). The mutant mice were viable at birth but displayed progressively enlarged kidneys with distinct physiological features of polycystic kidney diseases (Fig. 18A, B, Table 1). At postnatal day 7 (P7), *Cep90* KO kidneys appeared mostly normal but began exhibiting cystic dilations by P21, with severe cyst enlargement evident by P42 and P84, accompanied by elevated kidney to body weight ratios (Fig. 18C, D, Fig 19). The kidneys of Cep90 heterozygous KO mice were grossly normal until 1 year of age (data not shown). Notably, there was no significant gender difference in cyst formation (Fig. 20).

To dissect the tissue origins of kidney cysts in *Cep90* KO mice, I immunostained the kidney sections with aquaporin-1, calbindin-1 and aquaporin-2 antibodies, marking proximal convoluted tubules, distal convoluted tubules and collecting ducts, respectively (Fig. 21A). Cystic dilations were predominantly observed in distal convoluted tubules and collecting ducts at P21 and P42, gradually expanding to proximal convoluted tubules by P84 (Fig. 21B). These findings underscore the progressive renal cyst formation resulting from kidney-specific deletion of *Cep90*.

Gradual loss of cilia and its contribution to developing cysts in *Cep90* KO kidneys

Cep90 is essential for the establishment of distal appendages at centrioles, a prerequisite for ciliogenesis (Kumar et al., 2021). To measure the extent of ciliary loss and determine its contribution to the polycystic kidney phenotype in mutant mice, I assessed distal appendage formation in tubular cells of *Cep90* KO kidneys. Even in the mutant kidneys, Cep83,

a marker for distal appendages, was detected in epithelial cells at normal tubules, but not in cysts (Fig. 22A, B). Furthermore, cilia were not observed in the basal bodies lacking Cep83 signals in cyst cells (Fig. 22A). Similar results were obtained using Cep164, another marker for distal appendages (Fig. 22C, D). These findings strongly suggest that cilia fail to form in *Cep90*-deleted cells, due to the absence of distal appendages at centrioles.

To investigate whether the absence of cilia in epithelial cells contributes to renal cyst formation in *Cep90* KO kidneys, I coimmunostained kidney tissues with cilia markers, including acetylated tubulin and Arl13b antibodies, along with the Cep90 antibody. I focused on P42 kidney tissues, where both normal tubules and cysts are readily identifiable. My results revealed the presence of cilia in epithelial cells of normal tubules but their absence in cysts (Fig. 23A-C). Additionally, Cep90 signals were detected at basal bodies in epithelial cells of normal tubules but not in cyst-lining epithelial cells (Fig. 23A). These results indicate that deletion of the *Cep90* gene occurs progressively in my mouse model and provide a direct link between ciliary loss induced by the Cep90 deficiency and renal cyst development.

Along this line, I observed a diversity of cysts with varying lumen sizes in *Cep90* KO kidneys. Coimmunostaining analyses revealed coexistence of both ciliated and non-ciliated epithelial cells in small cysts, whereas large cysts exclusively comprised non-ciliated epithelial cells (Fig. 24A-C). I classified cysts containing ciliated epithelial cells as early-stage cysts, while those lacking ciliated cells were designated as late-stage cysts. The lumen area of early-stage cysts measured approximately 500 μm^2, whereas that of late-stage cysts was approximately 10 times larger (Fig. 24A, C).

I quantified the number of early- and late-stage cysts during renal cystogenesis. Early-stage cysts predominated at P21 and P42 but declined by P84 in Cep90 KO kidneys (Fig. 25A, B). Conversely, the number of late-stage cysts began to increase at P42 and their area became predominant by P84 (Fig. 25A, B). These findings suggest that small cysts at the early-stage progress to large cysts at the late stage during cystogenesis, possibly due to continuous loss of cilia in cyst epithelial cells of *Cep90* KO kidneys.

Flattening of cyst epithelial cells may represent a notable feature of PKD kidneys (Grantham et al., 1987), and flat cyst epithelial cells were prevalently detected in the cysts of Cep90 KO kidneys (Fig. 26). I investigated the transformation of cuboidal tubule cells to flattened cyst cells during renal cystogenesis in *Cep90* KO kidneys. Coimmunostaining of P42

kidneys with Arl13b antibody to identify cilia, β-catenin antibody to measure epithelial cell widths, and aquaporin-2 antibody to delineate collecting tubules revealed that most epithelial cells in wild-type kidneys were cuboidal, regardless of cilia presence (Fig. 27A-C). Conversely, the majority of cyst cells in late-stage cysts of *Cep90* KO kidneys exhibited flattened morphology, characterized by decreased heights and increased widths of epithelial cells (Fig. 27A-C). In early-stage cysts, ciliated cells retained a cuboidal shape, while non-ciliated cells displayed a flattened morphology, even when coexisting within the same cyst (Fig. 27A-C).

To corroborate my observations, I coimmunostained kidney tissues with acetylated tubulin and β-catenin antibodies, focusing on the luminal side of epithelial cell surface. My results demonstrated that the surface areas of non-ciliated cells are larger than those of ciliated cells in early-stage cysts (Fig. 28A, B). These findings suggest that the epithelial linings of early-stage cysts in Cep90 KO kidneys is composed of a mixture of cuboidal cells with cilia and flattened cells without cilia (Fig. 29). Based on these observations, I propose that the cuboidal tubular cells undergo flattening upon loss of cilia following deletion of Cep90.

Selective activation of mTOR at the non-ciliated epithelial cells of early-stage cysts

The mTOR pathway is known to be regulated by cilia in kidney tubular cells in response to fluid flow, influencing cell size (Boehlke et al., 2010). To evaluate the role of the mTOR pathway in the morphological changes observed in Cep90 KO kidney tubule cells, I conducted coimmunostaining analysis with phospho-S6 ribosomal protein (p-S6RP) and acetylated tubulin antibodies. Results revealed a significant abundance of p-S6RP-positive populations in non-ciliated cells of early-stage cysts, while ciliated cells within the same cysts showed minimal positivity (Fig. 30A, B). Additionally, the number of p-S6RP-positive cells decreased in non-ciliated cells of late-stage cysts (Fig. 30A, B). Similar experiments using phospho-mTOR (p-mTOR) antibody, another indicator of mTOR activation, showed induction of p-mTOR exclusively in non-ciliated cells of early-stage cysts, with no such activation observed in ciliated cells (Fig. 31A, B). However, the proportion of p-mTOR-positive cells significantly decreased in late-stage cysts, suggesting a transient induction of mTOR activity in non-ciliated cyst cells at the early stage of cystogenesis.

To correlate mTOR activity with epithelial cell morphology, I coimmunostained P42 *Cep90* KO kidneys with p-S6RP and β-catenin antibodies. Interestingly, p-S6RP-positive cells

in early-stage cysts exhibited flattened morphology, characterized by increased cellular width, whereas p-S6RP-negative cells within the same cysts were cuboidal, suggesting selective activation of the mTOR pathway in the non-ciliated epithelial cells at early-stage cysts (Fig. 32 A-C). As anticipated, most cells in late-stage cysts exhibited flattened morphology, regardless of mTOR activity (Fig. 32A-C). The transient induction of mTOR activity in non-ciliated cyst cells at the early stage of cystogenesis suggests its potential role for initiating morphological changes of the epithelial cells.

YAP activation promoting the proliferation of flat cyst epithelial cells at late-stage cysts

Flat cyst epithelial cells in ADPKD mice are highly proliferative and become dominant during cystogenesis (Nishio et al., 2005; Cai et al., 2018; Lee et al., 2020; Panda et al., 2022). I also observed a significant increase in Ki-67-positive cells within late-stage cysts in Cep90 KO kidneys (Fig. 33). Based on the transient activation of the mTOR pathway in early-stage cysts of Cep90 KO kidneys (Fig. 30, Fig. 31), alternative molecular mechanisms should be adopted to maintain the proliferative capacity of late-stage cyst epithelial cells. Importance of YAP signaling in cystogenesis has been proposed in ADPKD and juvenile cystic kidney model mice (Cai et al., 2018; Dwivedi et al., 2020; Panda et al., 2022). I observed a significant increase in nuclear YAP-positive cells within cysts of Cep90 KO kidneys (Fig. 34). In support, I demonstrated upregulation of YAP downstream genes, including *c-myc*, *Cyr61*, *Ctgf*, and *Amotl2* in *Cep90* KO kidneys (Fig. 35). These findings collectively demonstrate YAP activation during cystogenesis in *Cep90* KO mice.

To examine the correlation between YAP activation and cilia ablation in renal cyst cells, I conducted coimmunostaining analyses with YAP and acetylated tubulin antibodies. Nuclear YAP was detected in approximately 20% of tubular cells in wild-type kidneys (Fig. 36). The proportion of nuclear YAP-positive cells significantly increased in epithelial cells of early-phase cysts, regardless of cilia presence (Fig. 36). Furthermore, the majority of late-phase cyst cells exhibited nuclear YAP positivity (Fig. 36). Consistent with cilia-independent YAP activation in late-stage cysts of Cep90 KO kidneys, cilia ablation did not activate YAP in a 2D culture system (Fig. 37). These results suggest progressive activation of YAP in cyst cells, irrespective of cilia.

FAK activation in cyst epithelial cells

Focal adhesion kinase (FAK) serves as a crucial link between mechanical stimuli and intracellular signaling outputs (Lachowski et al., 2018). YAP is one of the downstream targets of FAK (Totaro et al., 2018). Coimmunostaining analysis with phospho-FAK (p-FAK) antibody revealed a higher abundance of p-FAK-positive cells in cyst epithelial cells compared to normal epithelial cells (Fig. 38). Early-cyst epithelial cells predominantly exhibited p-FAK positivity, regardless of cilia presence, suggesting FAK activation in epithelial cells under mechanical stress during the early stage of cystogenesis (Fig. 38). FAK activity may be somewhat reduced after the formation of large cysts at late stages (Fig. 38). These results suggest that FAK may mediate mechanical stress to YAP activation during the early phase of cystogenesis, irrespective of ciliary functions.

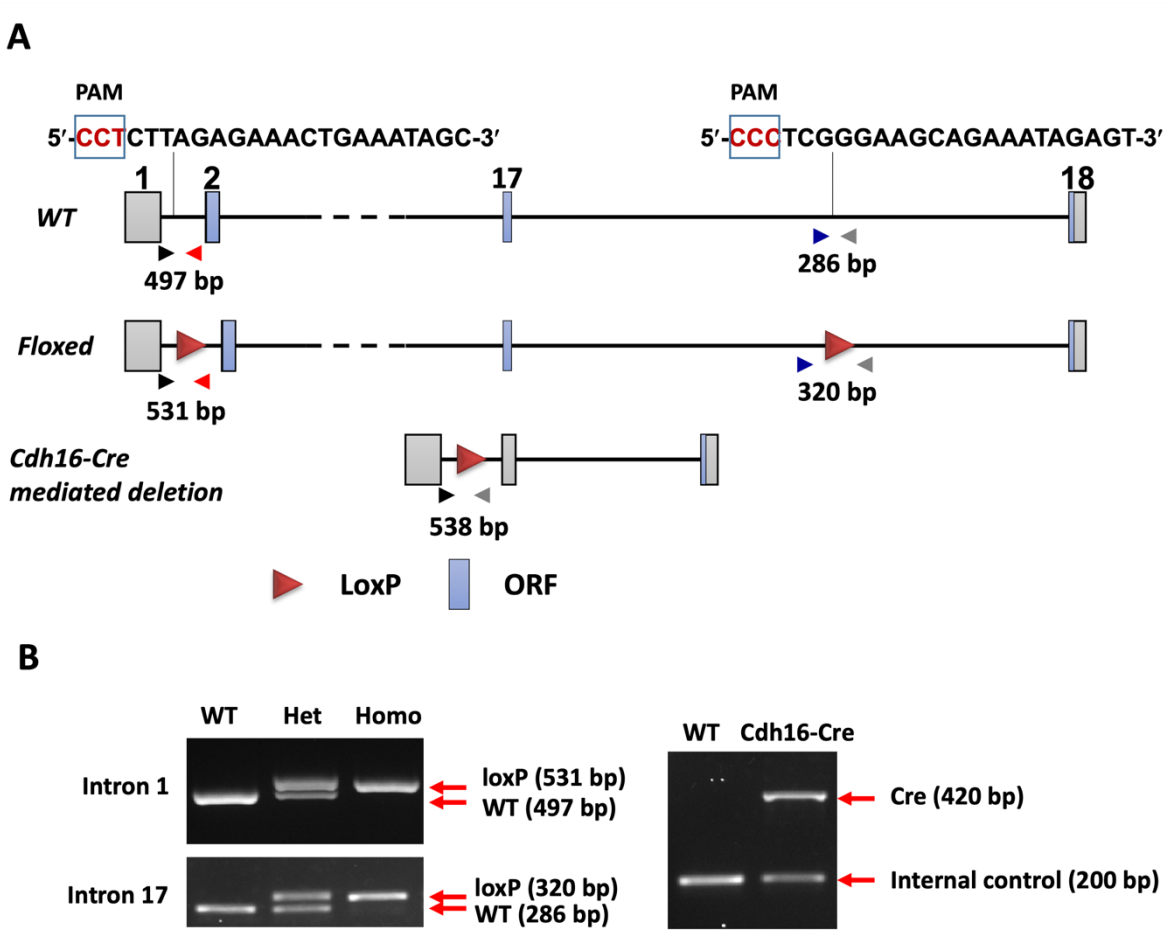

Figure 17. Kidney-specific *Cep90* KO mice (A) Schematic diagram illustrating the genetic strategy for Cdh16-Cre-mediated deletion of the floxed *Cep90* allele at the kidney. *LoxP* sites were inserted at the first and seventeenth introns of the *Cep90* gene, resulting in deletion of most of *Cep90* locus after the Cre-mediated recombination. (B) Representative PCR genotyping results for the floxed *Cep90* allele (left) and *Cdh16-Cre* transgene (right).

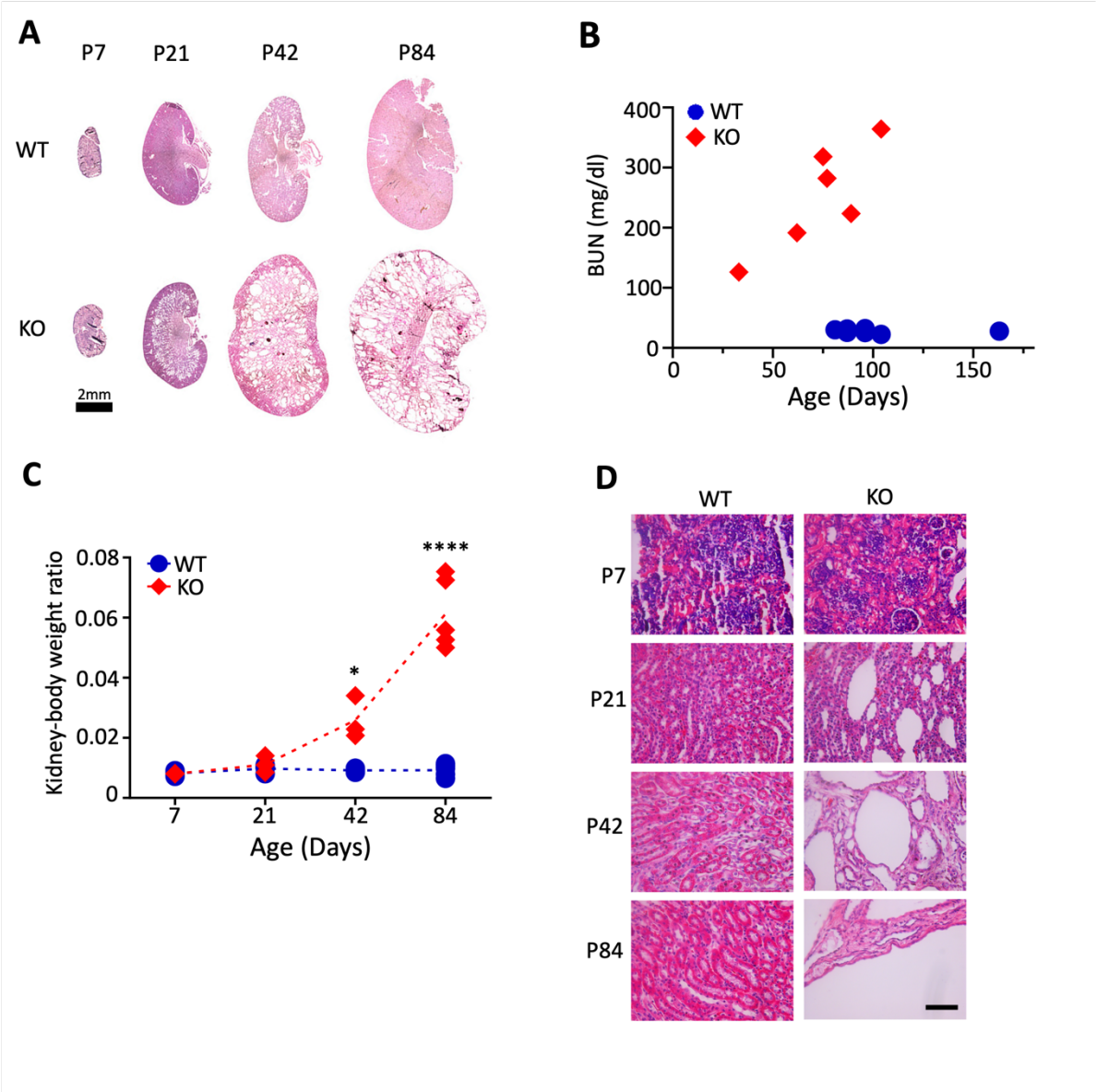

Figure 18. Renal cyst formation in the *Cep90* KO mice (A) Representative H&E staining images of *Cep90* KO kidneys at postnatal days 7, 21, 42, and 84. Scale bar, 2 mm. (B) Blood urea nitrogen (BUN) levels of the *Cep90* KO mice at indicated ages. (C) Kidney-to-body weight ratios of the *Cep90* KO mice at indicated ages. Statistical significance was determined using unpaired t-test (*, P<0.05; ****, P< 0.0001). (D) H&E staining of the kidney tissues of *Cep90* KO mice at indicated ages. Scale bar, 50 μm. (B,C) Data points represent individual mice examined.

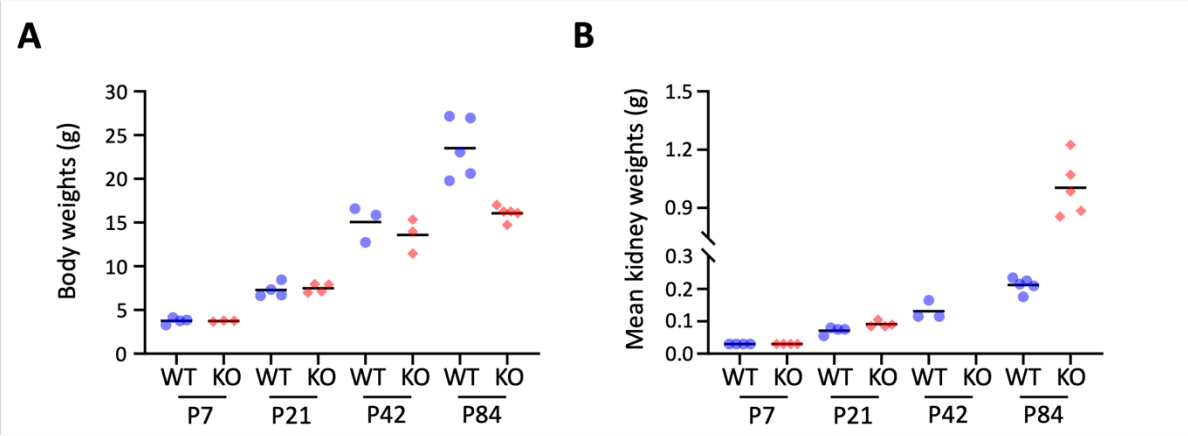

Figure 19. Measurement of body and kidney weights of the Cep90 KO mice Body weights (panel A) and average weights of both kidneys (panel B) of WT and *Cep90* KO mice. Mean values are depicted as black lines. Data points represent individual mice examined.

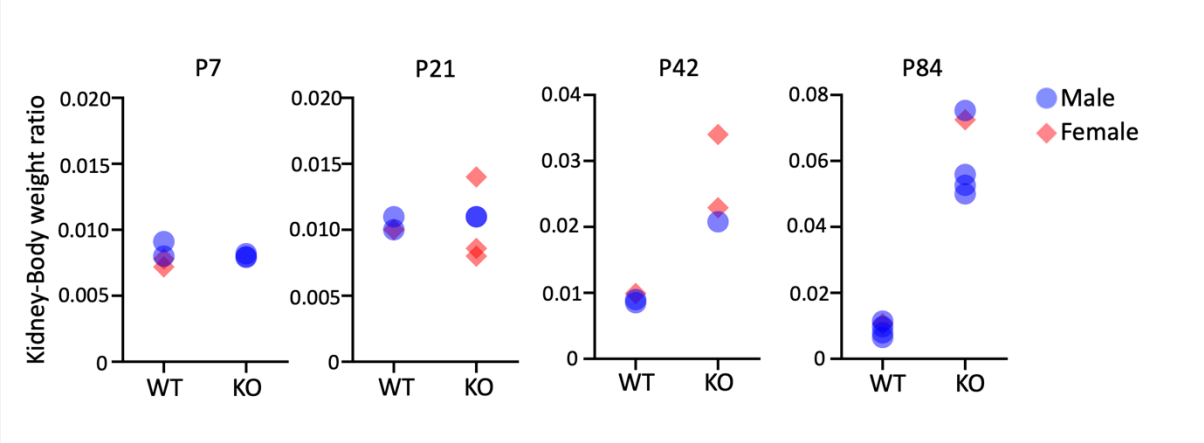

Figure 20. Sex-invariant roles of *Cep90* in renal cystogenesis The kidney-body weight ratios of male (blue) and female (pink) mice were determined. Data points represent individual mice examined.

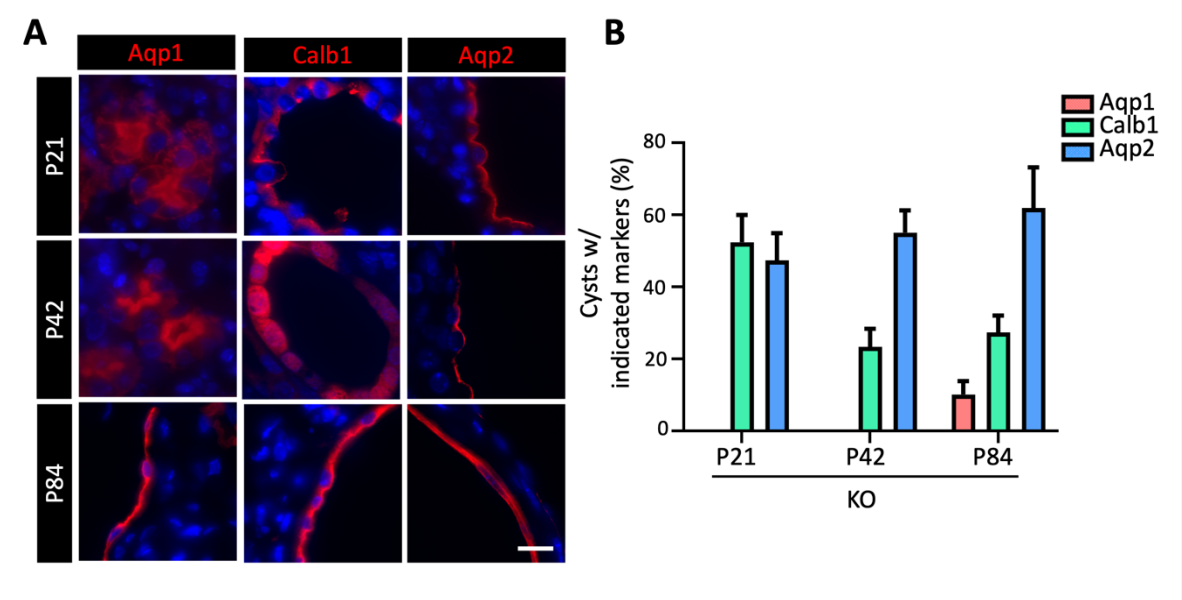

Figure 21. Origins of cysts in the *Cep90* KO kidneys (A) Kidney tissues of *Cep90* KO mice were immunostained with antibodies specific to nephron segment-specific markers (red), such as aquaporin-1 (Aqp1, proximal convoluted tubules), calbindin1 (Calb1, distal convoluted tubules), and aquaporin-2 (Aqp2, collecting tubules). Nuclei were visualized with DAPI. Scale bar, 10 μm. (B) The number of cysts with nephron segment markers was counted in *Cep90* KO kidneys. At least 600 cysts per an age group were counted (n=3). Values are means with standard deviations.

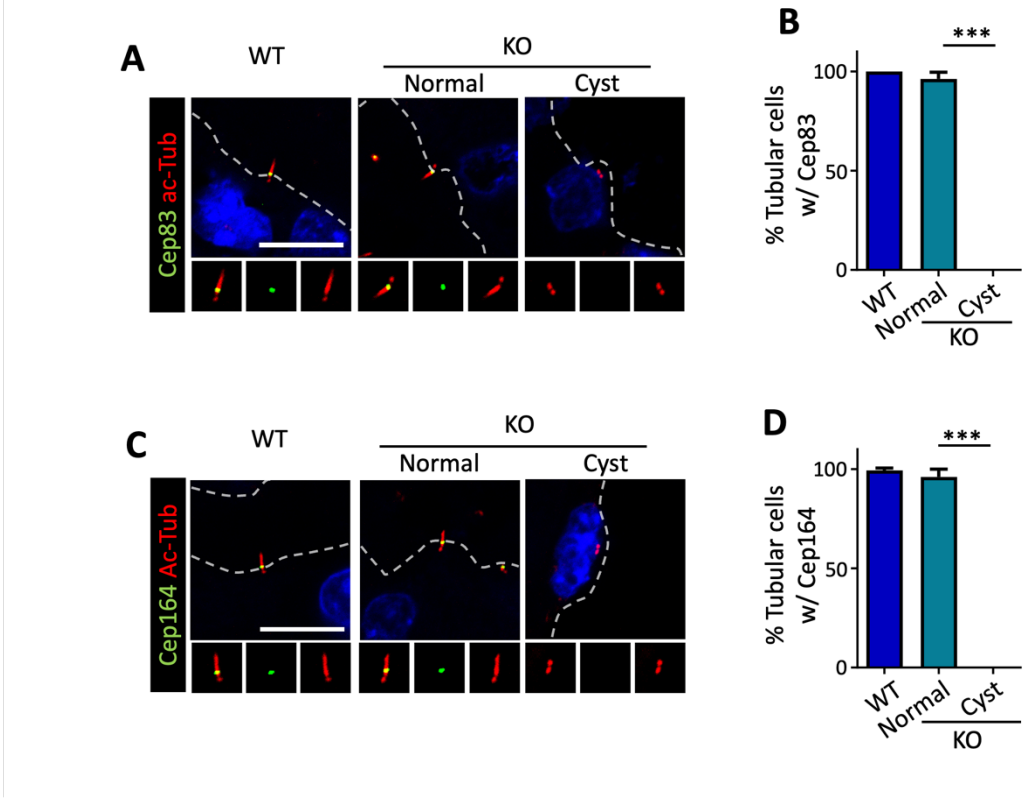

Figure 22. Absence of distal appendages at the cyst epithelial cells of *Cep90* KO kidneys
(A-D) Normal and cyst tissues of *Cep90* KO kidneys at P42 were coimmunostained with Cep83 (green) (A) and Cep164 (green) (C) antibodies, along with acetylated tubulin (red) antibody. The number of epithelial cells with Cep83 (B) and Cep164 (D) was counted. (A, C) nuclei were visualized with DAPI. Dotted lines were drawn to designate lumen boundary. Scale bars, 10 μm. (B, D) At least 150 cells per experimental group were counted in 3 independent experiments (n=3). Values are means with standard deviations. Statistical significance was determined using one-way ANOVA with Tukey post hoc test (***, P<0.001).

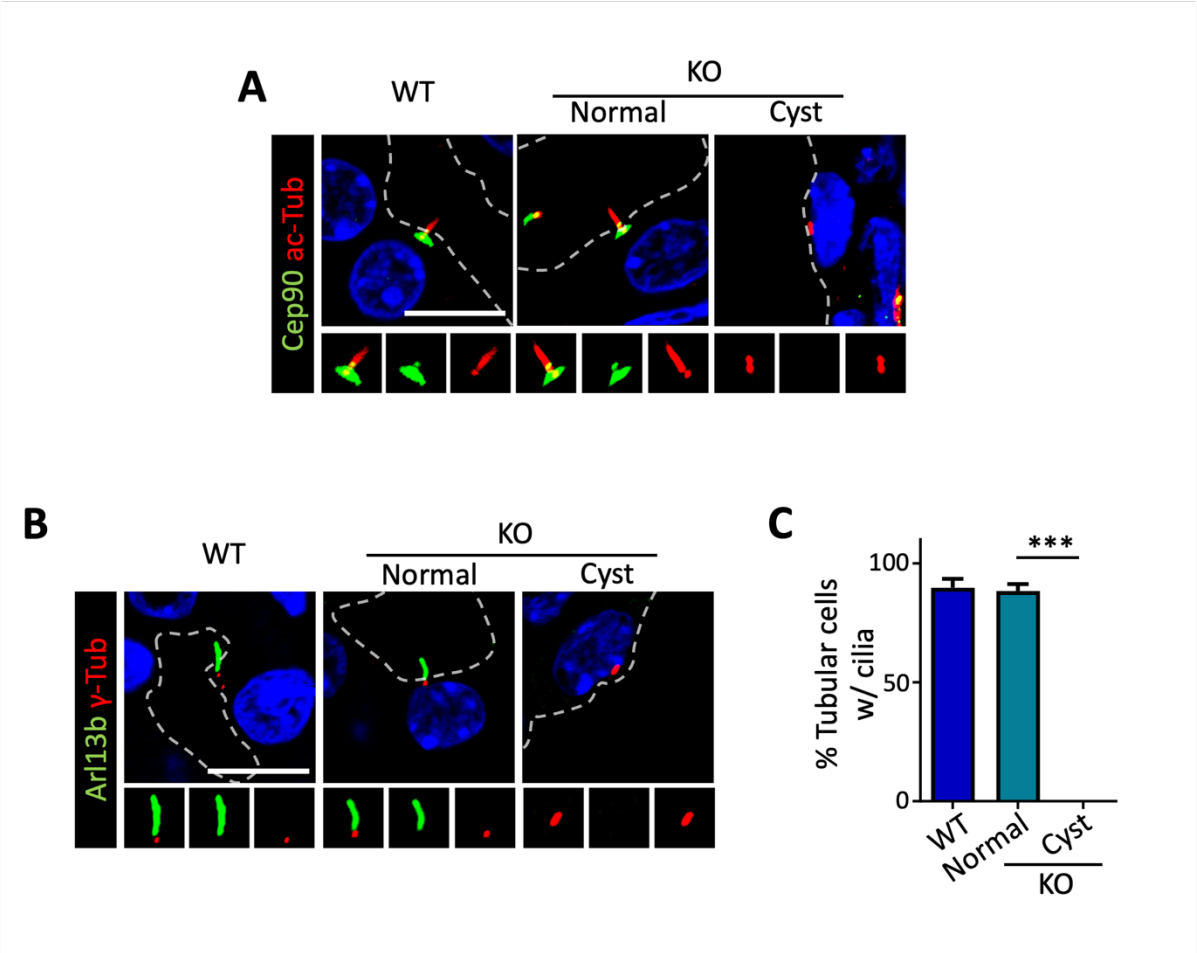

Figure 23. Absence of cilia at the cyst epithelial cells of *Cep90* KO kidneys (A) Normal and cyst cells of *Cep90* KO kidneys at P42 were coimmunostained with Cep90 (green) and acetylated-tubulin (red) antibodies. (B) The same tissues were coimmunostained with Arl13b (green) and γ-tubulin (red) antibodies. (C) The number of epithelial cells with primary cilia was counted. (A, B) nuclei were visualized with DAPI. Dotted lines were drawn to designate lumen boundary. Scale bars, 10 μm. (C) At least 150 cells per experimental group were counted in 3 independent experiments (n=3). Values are means with standard deviations. Statistical significance was determined using one-way ANOVA with Tukey post hoc test (***, P<0.001).

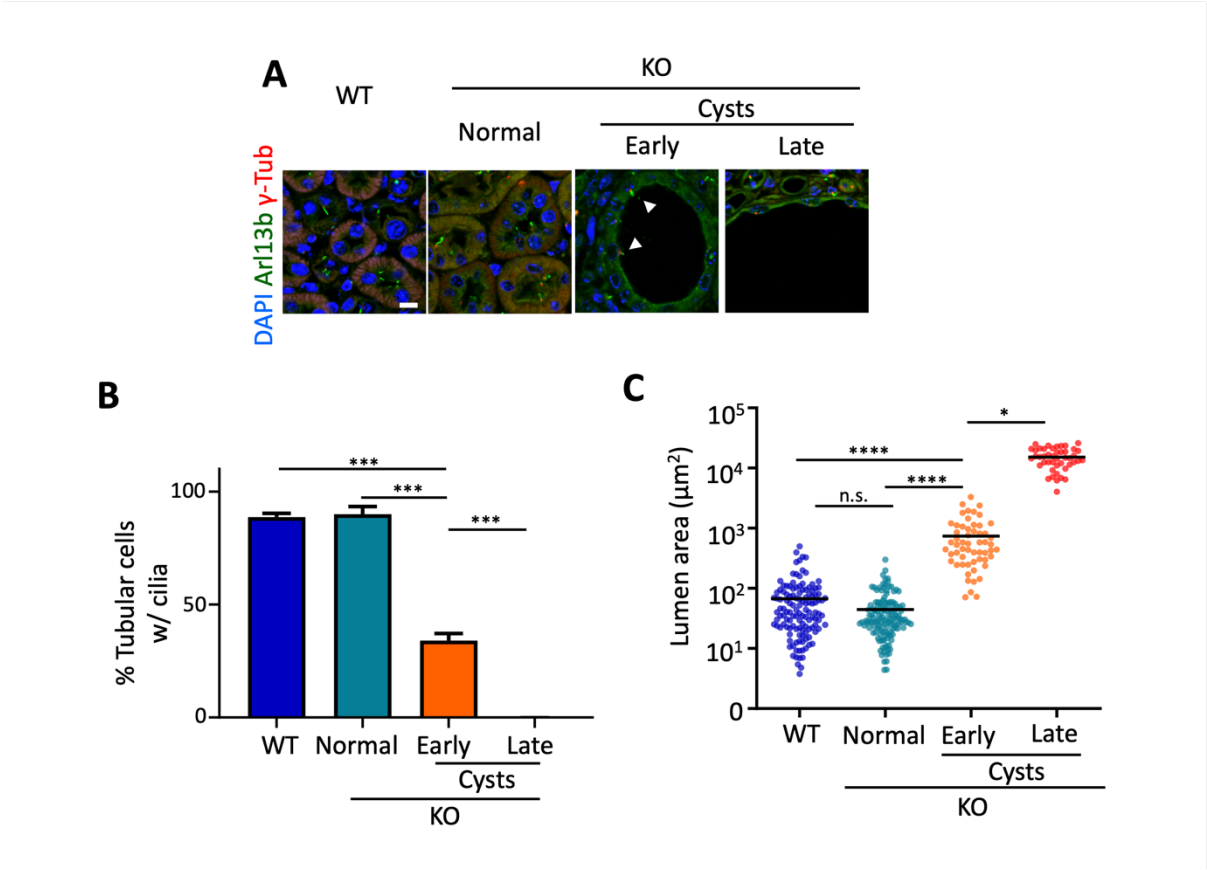

Figure 24. Definition of early- and late-stage cysts in *Cep90* KO kidneys (A) Kidney tissues of *Cep90* KO mice at P42 were coimmunostained with Arl13b (green) and γ-tubulin (red) antibodies. Cilia in the early-stage cysts were indicated as arrowheads. DNA was visualized with DAPI. Scale bar, 10 μm. (B) The number of epithelial cells with cilia was counted. At least 150 cells per category were counted (n=3). (C) The lumen area of early- and late-stage cysts was measured. At least 45 cysts per category were analyzed in 3 independent experiments (n=3). Values are means with standard deviations. Statistical significance was determined using one-way ANOVA with Tukey post hoc test or using Kruskal-Wallis test with Dunn's post hoc test (*, P<0.05; **, P< 0.01; ***, P< 0.001; ****, P<0.0001).

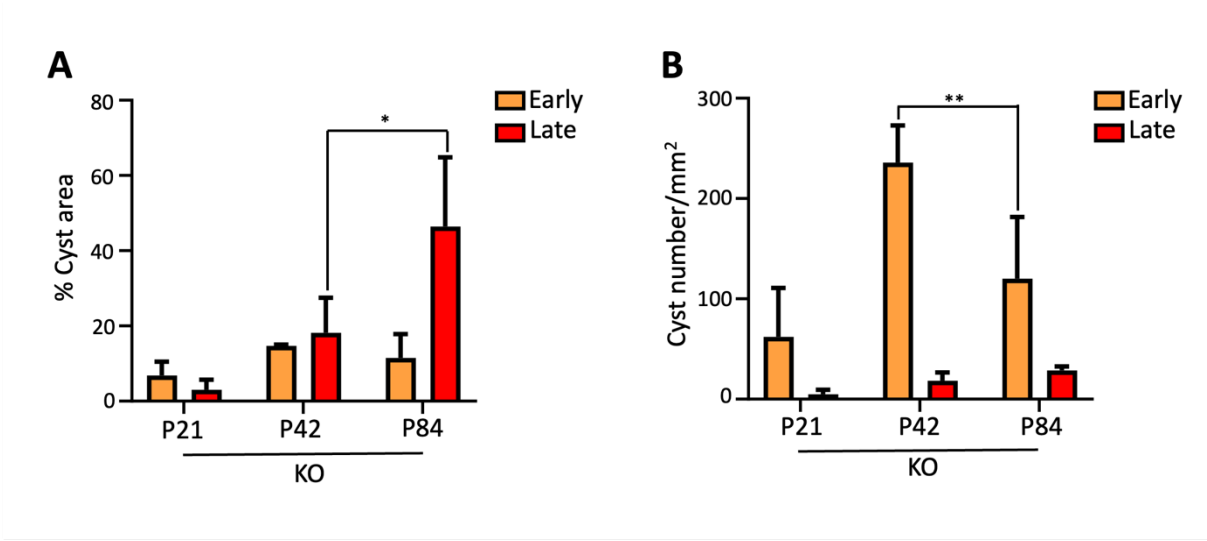

Figure 25. Occupancy of early- and late- stage cysts in the progression of cystogenesis in Cep90 KO kidneys (A) Proportion of the cyst area in the whole kidney tissues was determined. (B) The number of cysts in the whole kidney tissues were counted and presented as an average number of cysts per unit area. (A, B) At least 3 kidney sections per an age group were analyzed (n=3). Values are means with standard deviations. Statistical significance was determined using one-way ANOVA with Tukey post hoc test (*, $P<0.05$; **, $P< 0.01$; ***, $P< 0.001$; ****, $P<0.0001$).

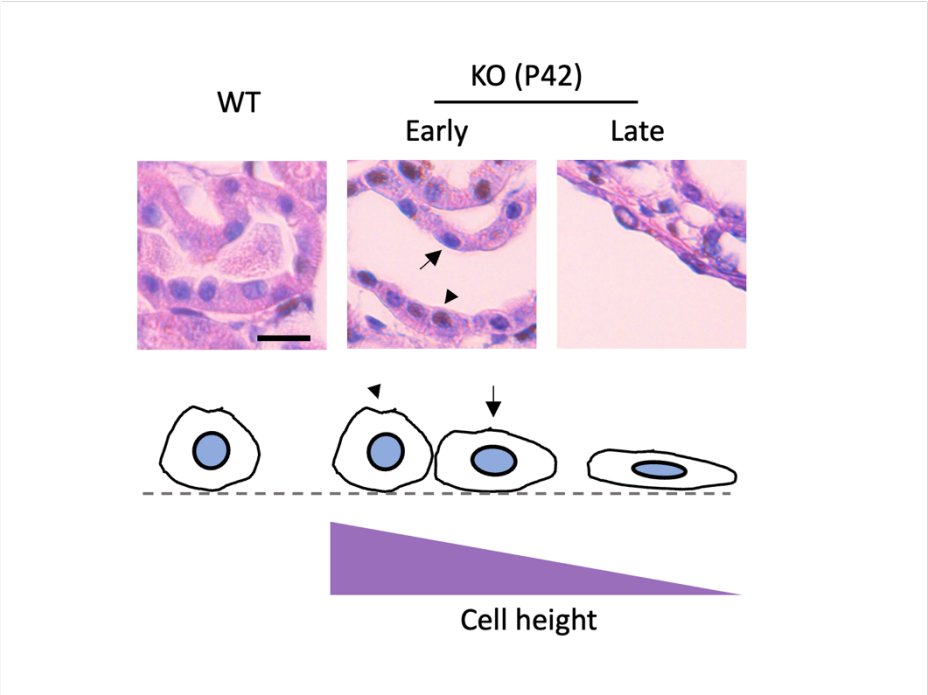

Figure 26. Flattening of epithelial cells in the *Cep90* KO kidneys (A) H&E staining of the kidney tissues of P42 *Cep90* KO mice and graphical summary of flattening of kidney tubular cells. Cuboidal cells and flattened cells were indicated as arrowheads and arrows, respectively. Scale bar, 10 μm.

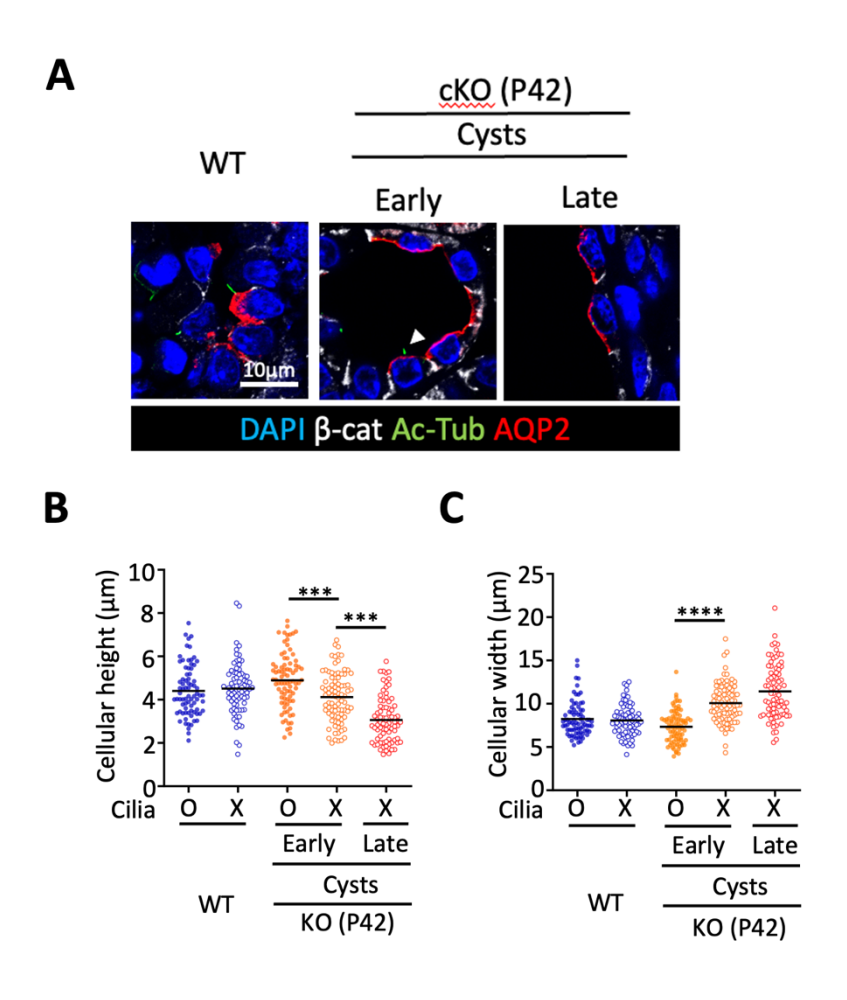

Figure 27. 2D analysis of cell morphology change during renal cystogenesis (A) Kidney tissues of *Cep90* KO mice at P42 were coimmunostained with β-catenin (white), acetylated tubulin (AC-Tub, green), and Aquaporin-2 (AQP2, red) antibodies. Cilia in the early-stage cysts were indicated as arrowheads. Nuclei were visualized with DAPI. Scale bars, 10 μm. (B, C) The height (B) and width (C) of the epithelial cells with and without cilia were measured. (B, C) At least 60 cells per experimental group were analyzed in 3 independent experiments (n=3). Statistical significance was determined using Kruskal-Wallis test with Dunn's post hoc test (*, P<0.05; ***, P< 0.001; ****, P<0.0001).

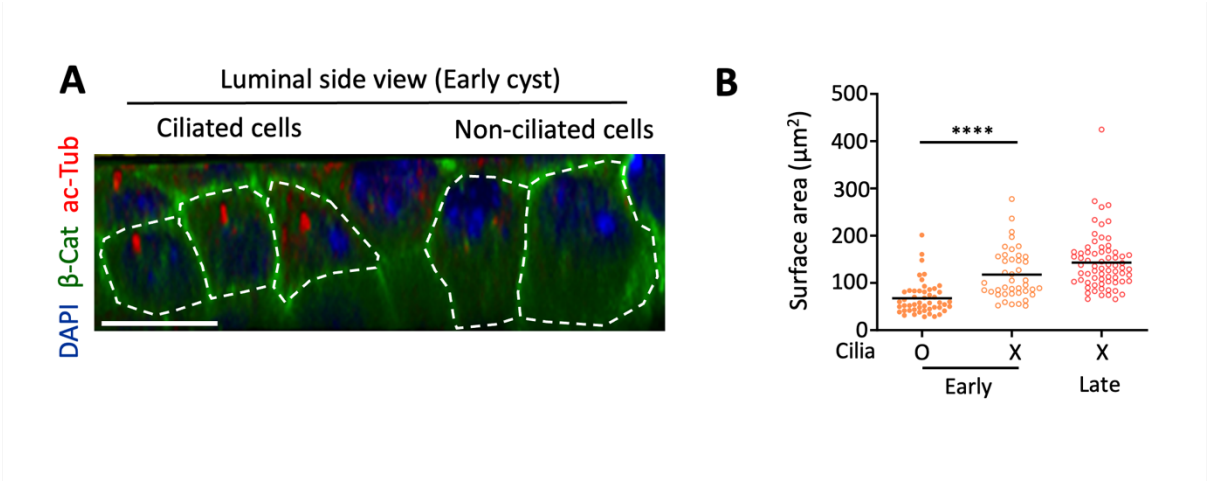

Figure 28. 3D analysis of cell morphology change during renal cystogenesis (A) Kidney tissues of Cep90 KO mice at P42 were coimmunostained with β-catenin (green) and acetylated tubulin (red) antibodies and observed from the lumen side. Dotted lines were drawn to designate cell boundary. Nuclei were visualized with DAPI. Scale bars, 10 μm. (B) Surface area of the epithelial cells was measured. (B) At least 43 cells per experimental group were analyzed in 3 independent experiments (n=3). Statistical significance was determined using Kruskal-Wallis test with Dunn's post hoc test (*, P<0.05; ***, P< 0.001; ****, P<0.0001).

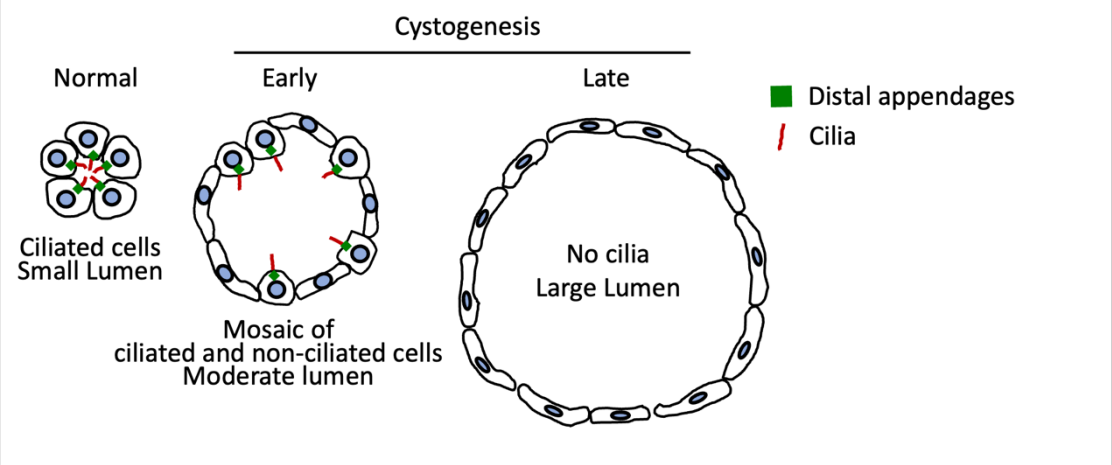

Figure 29. Hypothetical schematics illustrating the progression of renal cystogenesis Normal tubules have small lumens with ciliated tubular cells. Early-stage cysts consist of mosaics of ciliated and non-ciliated epithelial cells with moderate size of lumens. When cystogenesis progresses to late stage, cysts are enlarged and all the cyst epithelial cells are devoid of cilia.

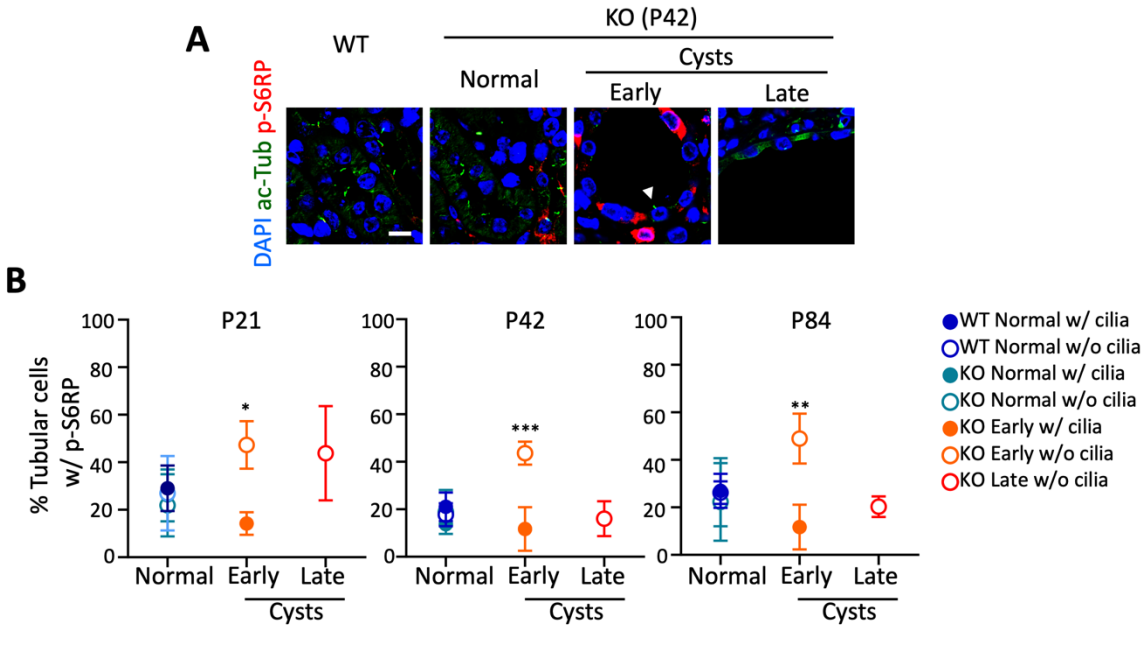

Figure 30. Activation of S6RP at non-ciliated epithelial cells in early-stage cysts (A) Kidney tissues of *Cep90* KO mice at P42 were coimmunostained with acetylated tubulin (ac-Tub, green) and phospho-S6RP (p-S6RP, red) antibodies. Cilia in the early-stage cysts were indicated as arrowheads. DNA was visualized with DAPI. Scale bars, 10 μm. (B) The number of phospho-S6RP-positive epithelial cells was counted in the cysts of *Cep90* KO kidneys at indicated ages. (B) At least 60 cells per experimental group was analyzed in 3 independent experiments (n=3). Values are means with standard deviations. Statistical significance was determined using one-way ANOVA with Tukey post hoc test (*, P<0.05; **, P< 0.01; ***, P< 0.001; ****, P<0.0001).

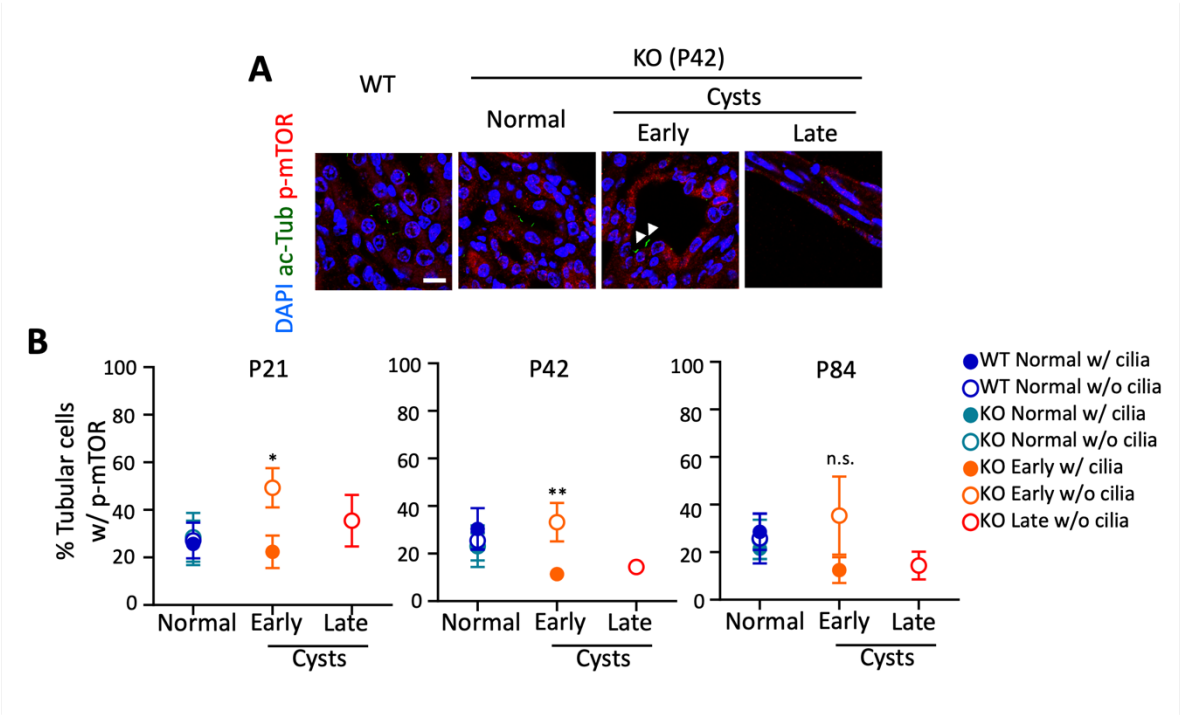

Figure 31. Activation of mTOR at non-ciliated epithelial cells in early-stage cysts (A) Kidney tissues of *Cep90* KO mice at P42 were coimmunostained with acetylated tubulin (ac-Tub, green) and phospho-mTOR (p-mTOR, red) antibodies. Cilia in the early-stage cysts were indicated as arrowheads. DNA was visualized with DAPI. Scale bars, 10 μm. (B) The number of phospho-S6RP-positive epithelial cells was counted in the cysts of *Cep90* KO kidneys at indicated ages. (B) At least 60 cells per experimental group was analyzed in 3 independent experiments (n=3). Values are means with standard deviations. Statistical significance was determined using one-way ANOVA with Tukey post hoc test (*, P<0.05; **, P< 0.01; ***, P< 0.001; ****, P<0.0001).

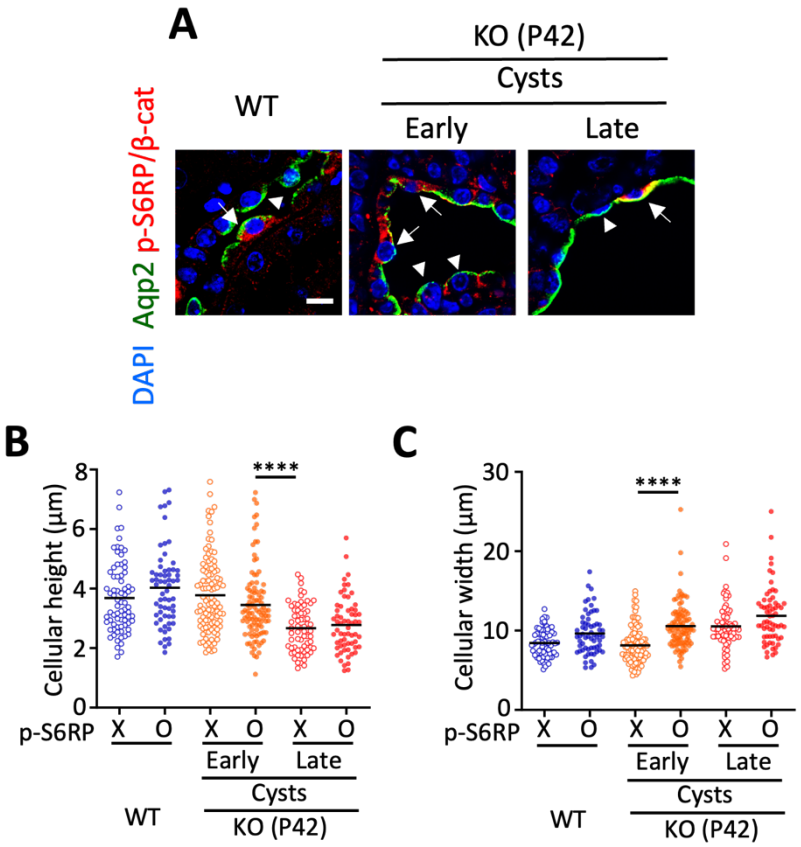

Figure 32. Cell morphology change in correlation with mTOR activation (A) Kidney tissues of *Cep90* KO mice at P42 were coimmunostained with aquaporin 2 (green), phospho-S6RP (red) and β-catenin (β-cat, red) antibodies. Cells with and without p-S6RP were indicated as arrows and arrowheads, respectively. Scale bars, 10 μm. (B, C) The height (B) and width (C) of the cells with p-S6RP signals were measured. (B, C) At least 60 cells per experimental group was analyzed in 3 independent experiments (n=3). Values are means with standard deviations. Statistical significance was determined using one-way ANOVA with Tukey post hoc test (*, P<0.05; **, P< 0.01; ***, P< 0.001; ****, P<0.0001).

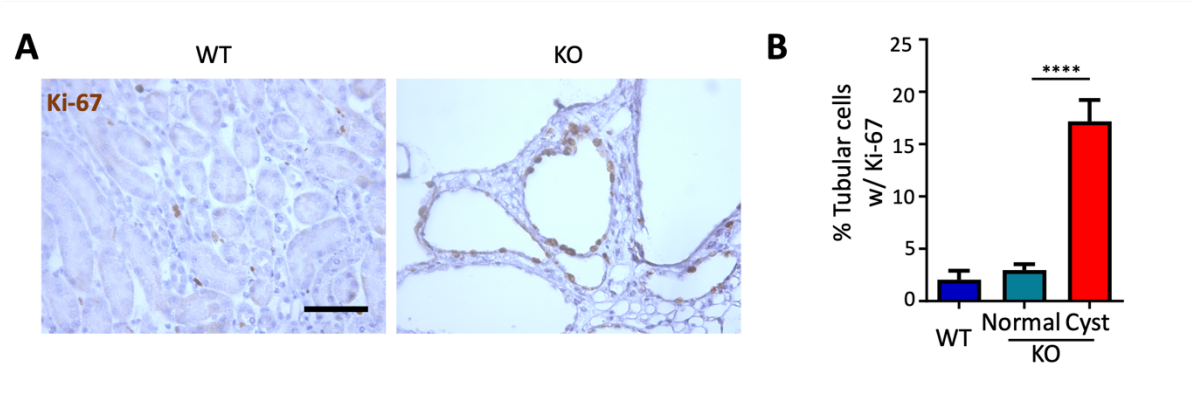

Figure 33. Active proliferation of the cyst epithelial cells (A) Kidney tissues of *Cep90* KO mice at P42 were immunostained with Ki-67 and counterstained with hematoxylin. Scale bars, 50 μm. (B) The number of tubular cells with Ki-67 signals was counted. At least 900 cells per experimental group were analyzed (n=3). Values are means with standard deviations. Statistical significance was determined with one-way ANOVA with Tukey post hoc test (****, P<0.0001).

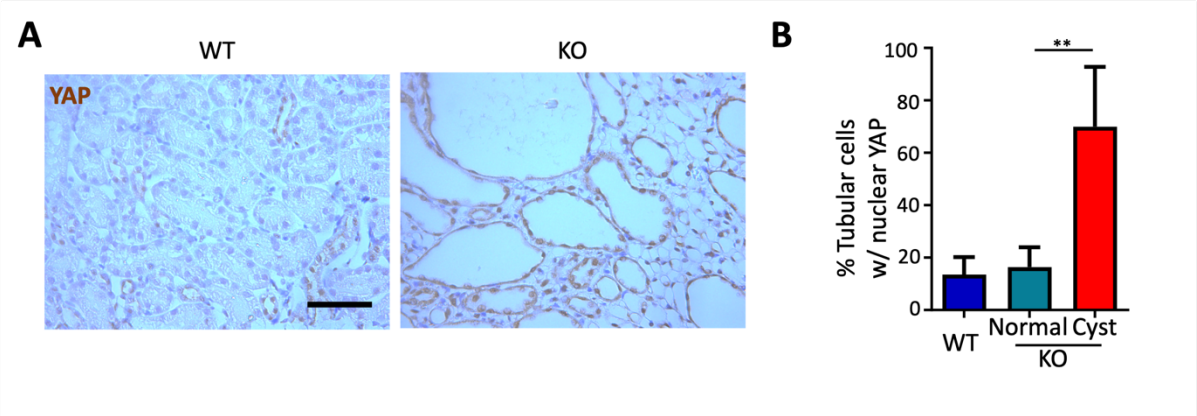

Figure 34. Activation of YAP in the cyst epithelial cells (A) Kidney tissues of *Cep90* KO mice at P42 were immunostained with YAP antibodies and counterstained with hematoxylin. Scale bars, 50 μm. (B) The number of tubular cells with nuclear YAP signals was counted. At least 900 cells per experimental group were analyzed (n=3). Values are means with standard deviations. Statistical significance was determined with one-way ANOVA with Tukey post hoc test (B) (**, $p<0.01$).

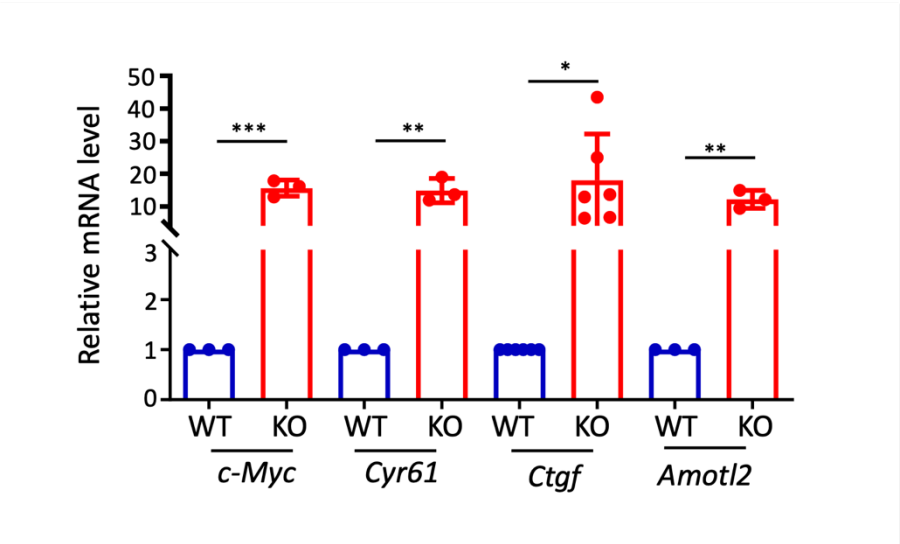

Figure 35. Analysis on the expression of YAP target genes in *Cep90* KO kidneys
Quantitative RT-PCR was carried out to determine expression of the YAP downstream genes (*c-Myc*, *Cyr61*, *Ctgf* and *Amotl2*) in *Cep90* KO kidneys at P84. At least 3 kidneys per experimental group were analyzed in 3 independent experiments (n=3). Values are means with standard deviations (n=3). Statistical significance was determined with unpaired t-test (E) (*, P<0.05; **, p<0.01; ***, P< 0.001).

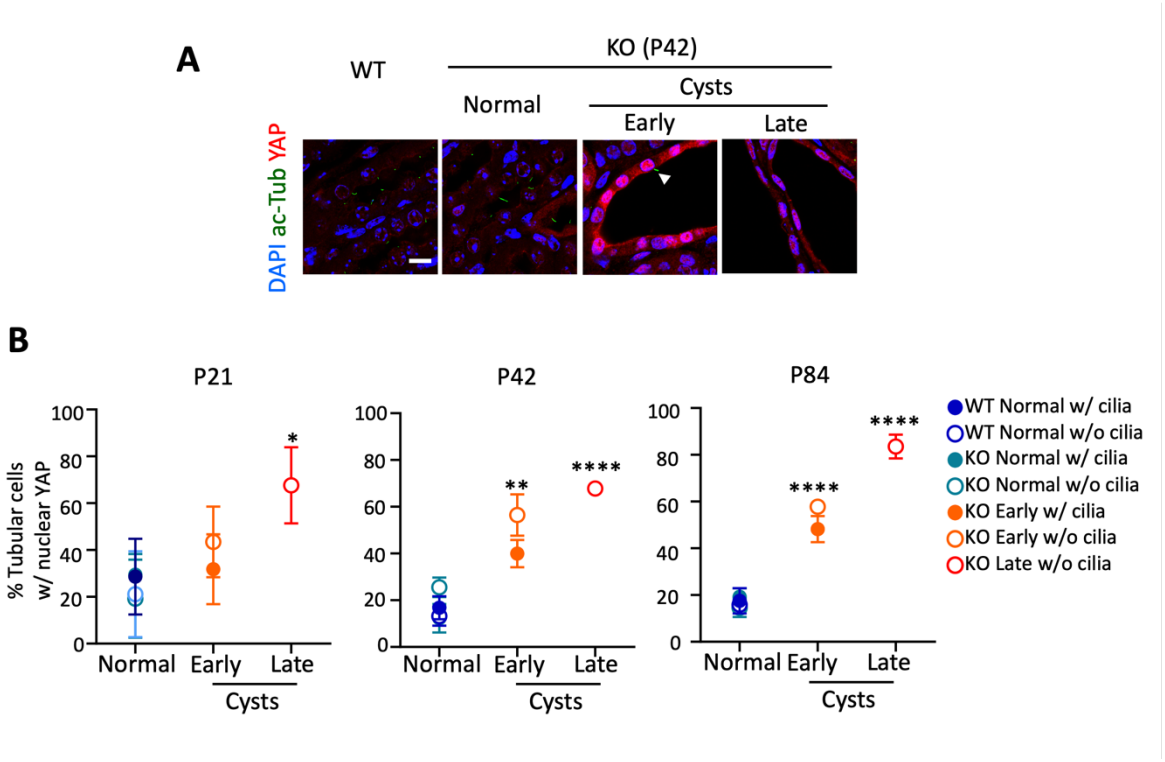

Figure 36. YAP activation in the late-stage cyst cells of *Cep90* KO kidneys (A) Kidney tissues of *Cep90* KO mice at P42 were coimmunostained with acetylated tubulin (green) and YAP (red) antibodies. Nuclei were visualized with DAPI. Scale bar, 10 μm. (B) The number of epithelial cells with nuclear YAP signals was counted. At least 60 cells per experimental group were analyzed in 3 independent experiments (n=3). Values are means with standard deviations. Statistical significance was determined using one-way ANOVA with Tukey post hoc test (*, P<0.05; **, P< 0.01; ****, P<0.0001).

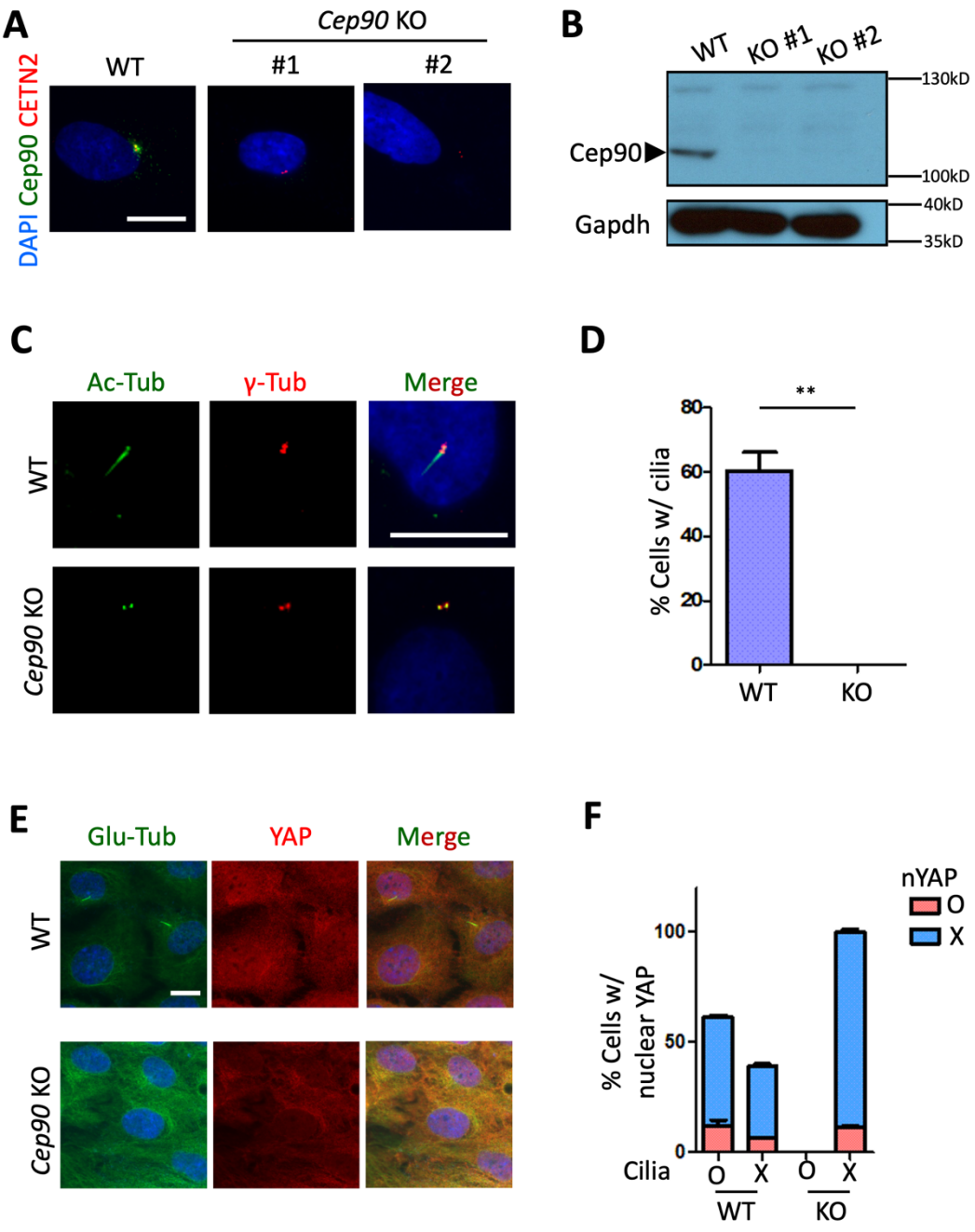
A
Cep90 KO
WT
#1
#2
DAPI Cep90 CETN2
B
WT
KO #1
KO #2
130kD
Cep90
100kD
40kD
Gapdh
35kD
C
Ac-Tub
γ-Tub
Merge
WT
Cep90 KO
D
**
% Cells w/ cilia
80
60
40
20
0
WT
KO
E
Glu-Tub
YAP
Merge
WT
Cep90 KO
F
nYAP
O
X
% Cells w/ nuclear YAP
100
50
0
Cilia
O
X
O
X
WT
KO

Figure 37. Absence of YAP activation in *Cep90* KO RPE1 cells (A) Two different lines of *Cep90* KO RPE1 cells were coimmunostained with Cep90 (green) and centrin-2 (CETN2, red) antibodies. (B) The *Cep90* KO RPE1 cells were subjected to immunoblot analysis with Cep90 and Gapdh antibodies. (C-F) *Cep90* KO RPE1 cells were cultured in serum-deprived medium for 48 h and coimmunostained with acetylated tubulin (ac-Tub, green) and γ-tubulin (γ-Tub, red) antibodies (C), or with glutamylated tubulin (Glu-Tub, green) and YAP (red) antibodies (E). (D, F) The number of cells with primary cilia (D) and with nuclear YAP (F) was counted. At least 90 cells per experimental group were analyzed in 3 independent experiments (n=3). Values are means with standard deviations. Statistical significance was determined with two-sided t test (D) and one-way ANOVA with Tukey post hoc test (F) ($p<0.005$). (A, C, E) Nuclei were visualized with DAPI. Scale bars, 10 μm.

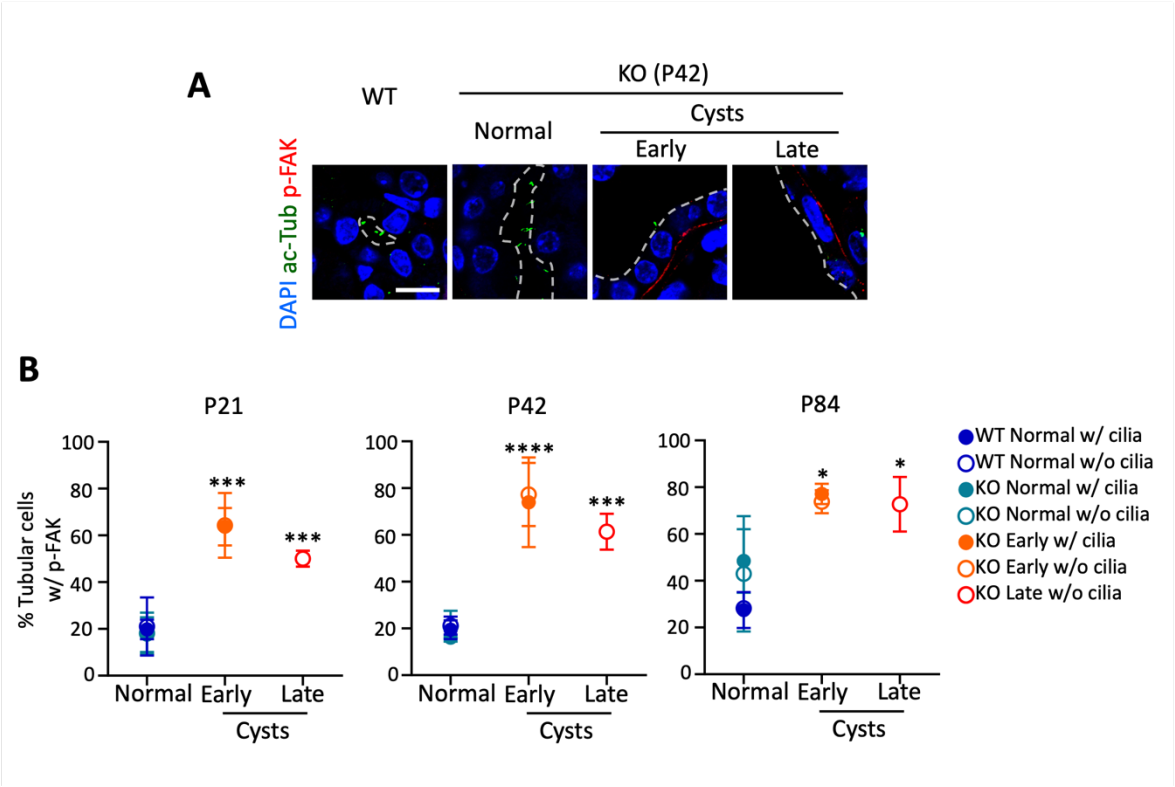

Figure 38. FAK activation in the late-stage cyst cells of *Cep90* KO kidneys (A) Kidney tissues of *Cep90* KO mice at P42 were coimmunostained *with* acetylated tubulin (ac-Tub, green) and phospho-focal adhesion kinase (p-FAK, red) antibodies. Dotted lines were drawn to designate lumen boundary. Nuclei were visualized with DAPI. Scale bar, 10 μm. (B) The number of epithelial cells with p-FAK signals was counted. At least 60 cells per experimental group were analyzed in 3 independent experiments (n=3). Values are means with standard deviations. Statistical significance was determined using one-way ANOVA with Tukey post hoc test (*, P<0.05; ***, P< 0.001; ****, P<0.0001).

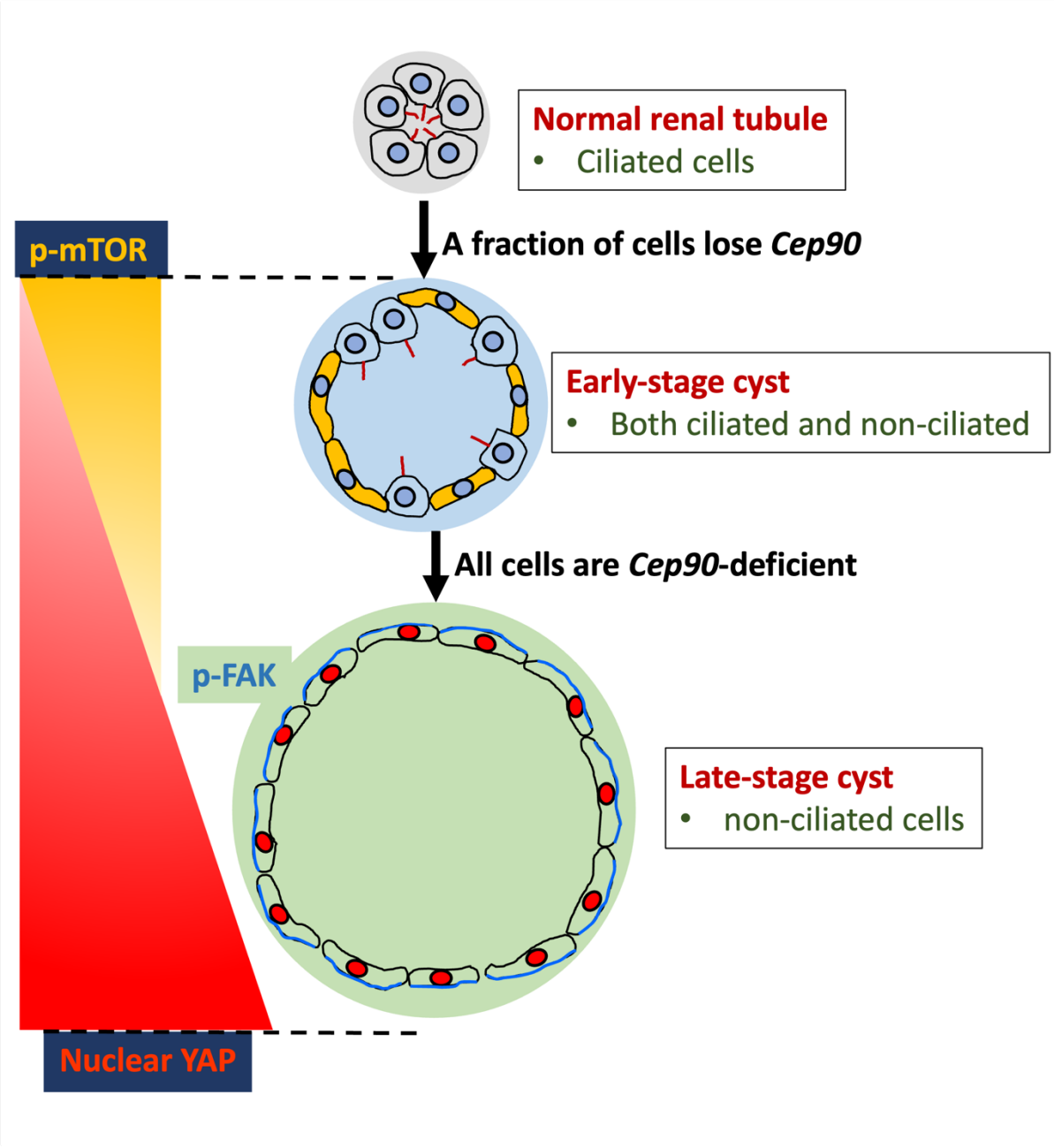

Figure 39. A model of cytogenesis induced by Cep90 deficiency Most of the renal epithelial cells possess cilia. In the early stage of cystogenesis, slow *Cep90* deletions make only a fraction of epithelial cells lose cilia. These non-ciliated epithelial cells exhibit increased activity in the mTOR signaling pathway and undergo a flattening in morphology. As cystogenesis progresses into the late stage, the majority of cyst epithelial cells lose their cilia and adopt a flattened morphology with activation of focal adhesion kinase (depicted with blue color). Concurrently there is a widespread activation of YAP in most of the cyst epithelial cells during the late stage of cystogenesis.

Group	Mouse ID	S	*Cep90*[*]	*Cdh16-Cre Tg*[†]	Age (days)	Total protein (g/dL)	Albumin (g/dL)	Globulin (g/dL)	Bilirubin (mg/dL)	ALP (IU/L)	AST (IU/L)	ALT (IU/L)	Creatine (mg/dL)
Normal	PCK-069	m	f/+	+	81	5.07	1.89	3.18	0.04	349.9	242.6	201.1	0.32
	PCK-287	f	f/f	-	87	5.31	1.94	3.37	0.015	411.2	82.1	40.4	0.37
	PCK-290	f	f/f	-	87	4.97	1.78	3.19	-0.043	418.7	112.1	42.8	0.33
	PCK-282	f	f/f	-	89	4.95	1.86	3.09	-0.024	440.6	71.5	27.4	0.32
	PCK-037	m	+/+	+	96	5.27	1.93	3.34	0.011	270.3	250.6	249.5	0.38
	PCK-045	f	+/+	+	96	4.37	1.63	2.74	0.113	345.1	58.2	29.4	0.34
	PCK-271	f	f/f	-	104	5.39	1.7	3.69	-0.04	301.2	52.7	25.4	0.3
	PCK-016	f	f/+	+	163	5.89	1.98	3.91	0.058	268.1	95.3	36.8	0.33
Cep90 KO	PCK-081	f	f/f	+	33	4.47	1.57	2.9	-0.009	906.0	73.6	28.2	0.9
	PCK-066	m	f/f	+	62	4.82	1.73	3.09	0.052	641.5	117.5	52.1	1.24
	PCK-060	m	f/f	+	75	4.42	1.52	2.9	0.014	1,015.6	357.2	225.2	0.87
	PCK-039	m	f/f	+	77	5.25	1.81	3.44	0.016	839.8	85.3	28.7	1.75
	PCK-283	f	f/f	+	89	4.89	1.66	3.23	-0.059	887.2	102.3	20.1	1.51
	PCK-270	f	f/f	+	104	5.4	1.79	3.61	-0.062	11,106.1	94.2	12.3	1.84

[*]f, floxed allele; +, wild-type

[†]+, Cdh16-Cre Tg; -, wild-type

ALT, alanine aminotransferase; AST, aspartate aminotransferase: ALP, alkaline phosphatase.

Table 1. Summary of kidney dysfunction in *Cep90* KO mice

DISCUSSION

Discovery of the early-stage cysts

In my study, I observed sequential progression of renal cystogenesis in kidney-specific *Cep90* KO mice. One notable aspect of my findings is the characterization of early-stage cysts, which exhibit unique composition of both ciliated and non-ciliated cells. This differs from observations in other PKD mouse models targeting cilia-associated genes, such as Cep164 and Wdr19 where cysts predominantly consist of non-ciliated epithelial cells (Aririk et al., 2019; Yu et al., 2022). Interestingly, I noted a slower progression of cystogenesis in *Cep90* KO mice compared to other PKD mouse models. For instance, by postnatal day 21, the kidneys in *Cep164* and *Wdr19* KO mice already exhibit significant cystogenesis leading to mortality (Aririk et al., 2019; Yu et al., 2022), whereas in *Cep90* KO mice of the same age, cystogenesis is just beginning (Fig. 18). Moreover, the presence of mosaic cysts containing both ciliated and non-ciliated epithelial cells is a unique feature not previously reported in other PKD mouse models.

The reasons underlying the slow progression of cystogenesis in Cep90 KO kidneys remain uncertain. One possibility is that the LoxP recombination events may occur less frequently in *Cep90* KO kidneys. It is known that the efficiency of LoxP recombination can be influenced by the distance between LoxP sites in the genome (Turlo et al., 2010; Faust et al., 2023). In my *Cep90*-floxed allele, the LoxP sites are spaced approximately 149 kb apart, a distance notably longer than other floxed alleles (Aririk et al., 2019; Yu et al., 2022). The long genomic distance between LoxP sites may contribute to a lower recombination efficiency, potentially leading to a delayed onset of cystogenesis in *Cep90* KO kidneys.

Mosaic early-stage cysts with ciliated and non-ciliated cells

In contrast to the monoclonal proliferation hypothesis for renal cystogenesis, a chimeric mouse model showed that early-stage cystic epithelium is composed of Pkd1-deficient cells and wild-type cells (Nishio et al., 2005). I observed the initiation of cystogenesis where only a fraction of tubular cells lost cilia. It means that we have established a novel PKD

mouse model capable of genetically inducing mosaicism in the cyst epithelium in the early stage.

Non-ciliated cells in early-stage cysts exhibited distinct characteristics, including preferential activation of the mTOR pathway and flattened cell morphology, consistent with previous reports indicating up-regulation of mTOR signaling concomitant with loss of cilia (Boehlke et al., 2010; Orhon et al., 2016). The absence of cilia might lead to mTOR activation, resulting in the enlargement of cell surface area, a phenomenon observed in both kidney and brain (Boehlke et al., 2010; Foerster et al., 2017). The involvement of mTOR in cystogenesis has been reported in the ADPKD mice (Shillingford et al., 2006; Fantus et al., 2016). However, its activation is not consistently maintained in late-stage renal cysts, suggesting transient activation of mTOR only at the initial stage of renal cystogenesis (Hartman et al., 2009; Ma et al., 2013).

Sequential progression of renal cysts from early to late stages

The advance from the early-stage cysts, characterized by the presence of both ciliated and non-ciliated epithelial cells, to late-stage cysts, which predominantly consist of non-ciliated epithelial cells, suggests a dynamic progression during renal cystogenesis in Cep90 KO kidneys (Fig. 39). This transition is supported by the decrease in the number of early-stage cysts and concurrent increase in the number of late-stage cysts with age. It is conceivable that during this progression, the continuous deletion of *Cep90* in tubular cells may lead to cilia loss, contributing to the formation of late-stage cysts. Additionally, the concept of clonal expansion of cyst cells, proposed in ADPKD mice, could also be applicable in this context (Wu et al., 1998). That is, non-ciliated, *Cep90*-deleted cyst cells may undergo preferential expansion, eventually dominating the normal epithelial cell population and resulting in mostly non-ciliated late-stage cysts. However, it is important to acknowledge the possibility that early-stage cysts may maintain their configuration over time without significant changes in epithelial cell composition. Indeed, intact normal tubules and small cysts persist even in aged *Cep90* KO mice.

The impact of cyst epithelial cells on adjacent cells has long been a subject of interest. A previous study utilizing chimeric mice with coexisting *Pkd1*-deficient cells and normal tubular cells, has suggested that the cystic environment might influence nearby normal cells

(Nishio et al., 2005). Similarly, it has been proposed that *Pkd1*-deficient cell-derived extracellular vesicles could affect neighboring cells (Ding et al., 2021). Following primary alterations in cystic cells, possibly mediated by mTOR, nearby cells may become involved in cystogenesis via the YAP signaling pathways (Panda et al., 2022). This provides an example that an interplay between cystic and neighboring cells underscores the complexity of renal cyst development and the potential for cross-talk between different cellular populations within the kidney.

Signaling pathways for late-stage cysts

YAP serves as a downstream effector of the Hippo signaling pathways, which include regulatory kinases such as Mst1/2 and Lats1/2 (Fu et al., 2022). Indeed, YAP functions as a mechano-transducer whose activity is influenced by cell shape and rigidity of the extracellular matrix (ECM) substrate (Dupont et al., 2011; Aragona et al., 2013; Totaro et al., 2018). In *Cep90* KO kidneys, I observed that YAP activation commences at early-stage cysts and intensifies in late-stage cysts. Interestingly, nuclear YAP was detected not only in non-ciliated cells but also in ciliated cells of early-stage cysts, suggesting that YAP activity is not directly regulated by ciliary functions. Similarly, FAK, an upstream regulator of YAP, was also activated in both ciliated and non-ciliated cyst cells in Cep90 KO kidneys.

Based on these observations, I propose that YAP activation in *Cep90* KO kidneys is likely triggered by the cystic environment, characterized by factors such as excessive deposition of ECM components accompanying inflammation or dysregulation of normal physiological flow within cystic lumen. Indeed, previous studies have highlighted the importance of ECM components in cyst progression, particularly in ADPKD mice (Lee et al. 2015; Zhang et al. 2020). As YAP acts as a transcriptional coactivator involved in both the disassembly of cilia as the promotion of cell proliferation, its activation may exacerbate cystogenesis by affecting ciliated cells in early-stage cysts (Moya et al., 2019; Kim et al., 2015).

Sequential activation of the signaling pathways during renal cystogenesis

Multiple signal transduction pathways are known to be activated for renal cystogenesis in mouse PKD models. I propose that these pathways are sequentially activated by diverse signaling ques during cystogenesis. The mTOR pathway may serve as an early player, activated

only in non-ciliated tubular cells at early-stage cysts, while YAP may act as a late-playing pathway, predominantly activated at late-stage cysts regardless of cilia presence (Fig. 39). Understanding the linkage between these pathways could provide valuable insights into the mechanisms underlying cyst development.

CONCLUSION AND PERSPECTIVES

In my doctoral research, I set out to investigate the roles of centrosomes and cilia in pathological conditions, with a specific focus on cancer and polycystic kidney disease (PKD). In chapter 1, I demonstrated that pericentriolar material, presumed essential for microtubule organization, can suppress centriole amplification in cancer cells. In chapter 2, I identified a progression mechanism for PKD driven by structural abnormalities of cilia. While these findings align with existing perspectives to some extent, they uncover underexplored aspects of centrosome and cilia biology, expanding our understanding of these organelles in disease contexts.

Historically, dysfunction of the centrosome and cilia has been associated with a narrow range of cellular phenotypes. Centrosome abnormalities were primarily linked to spindle pole formation, while cilia dysfunction was considered mainly a disruption in cilia-associated signaling. Although my research corroborates these traditional views, it also reveals that the pathways to these cellular abnormalities are not monolithic. For instance, centrosome amplification in cancer cells is typically attributed to PLK4 overexpression, but my work highlights an alternative mechanism that contributes to this amplification. Similarly, my study on PKD illustrates a specific sequence of abnormal signaling events driving disease progression. These findings further imply that the extent to which these abnormalities contribute to the severity of the outcome is not uniform either. For instance, centrioles assembled during M-phase may not induce multipolar spindle formation as robustly as those amplified via PLK4 overexpression, as they lack sufficient maturation time.

The centrosome, while small and structurally complex, serves as a foundational organizer within the cell. My research underscores the diversity of mechanisms leading to pathological outcomes, and the variation in the severity of these outcomes. Future work focusing on the underexplored paths to the centrosome abnormality will be of great value.

REFERENCES

Airik R, Airik M, Schueler M, Bates CM, Hildebrandt F. Roscovitine blocks collecting duct cyst growth in Cep164-deficient kidneys. Kidney Int. 2019;96(2):320-6.

Aragona M, Panciera T, Manfrin A, Giulitti S, Michielin F, Elvassore N, et al. A mechanical checkpoint controls multicellular growth through YAP/TAZ regulation by actin-processing factors. Cell. 2013;154(5):1047-59.

Balczon R, Bao L, Zimmer WE, Brown K, Zinkowski RP, Brinkley BR. Dissociation of centrosome replication events from cycles of DNA synthesis and mitotic division in hydroxyurea-arrested Chinese hamster ovary cells. J Cell Biol. 1995;130(1):105-15.

Bettencourt-Dias M, Rodrigues-Martins A, Carpenter L, Riparbelli M, Lehmann L, Gatt MK, et al. SAK/PLK4 is required for centriole duplication and flagella development. Curr Biol. 2005;15(24):2199-207.

Boehlke C, Kotsis F, Patel V, Braeg S, Voelker H, Bredt S, et al. Primary cilia regulate mTORC1 activity and cell size through Lkb1. Nat Cell Biol. 2010;12(11):1115-22.

Cabral G, Sans SS, Cowan CR, Dammermann A. Multiple mechanisms contribute to centriole separation in C. elegans. Curr Biol. 2013;23(14):1380-7.

Cai J, Song X, Wang W, Watnick T, Pei Y, Qian F, et al. A RhoA-YAP-c-Myc signaling axis promotes the development of polycystic kidney disease. Genes Dev. 2018;32(11-12):781-93.

Chan JY. A clinical overview of centrosome amplification in human cancers. Int J Biol Sci. 2011;7(8):1122-44.

Chapin HC, Caplan MJ. The cell biology of polycystic kidney disease. J Cell Biol. 2010;191(4):701-10.

Chng WJ, Ahmann GJ, Henderson K, Santana-Davila R, Greipp PR, Gertz MA, et al. Clinical implication of centrosome amplification in plasma cell neoplasm. Blood. 2006;107(9):3669-75.

Claude-Taupin A, Isnard P, Bagattin A, Kuperwasser N, Roccio F, Ruscica B, et al. The AMPK-Sirtuin 1-YAP axis is regulated by fluid flow intensity and controls autophagy flux in kidney epithelial cells. Nat Commun. 2023;14(1):8056.

Davenport JR, Watts AJ, Roper VC, Croyle MJ, van Groen T, Wyss JM, et al. Disruption of intraflagellar transport in adult mice leads to obesity and slow-onset cystic kidney disease. Curr Biol. 2007;17(18):1586-94.

Derderian C, Canales GI, Reiter JF. Seriously cilia: A tiny organelle illuminates evolution, disease, and intercellular communication. Dev Cell. 2023;58(15):1333-49.

Dictenberg JB, Zimmerman W, Sparks CA, Young A, Vidair C, Zheng Y, et al. Pericentrin and gamma-tubulin form a protein complex and are organized into a novel lattice at the centrosome. J Cell Biol. 1998;141(1):163-74.

Ding H, Li LX, Harris PC, Yang J, Li X. Extracellular vesicles and exosomes generated from cystic renal epithelial cells promote cyst growth in autosomal dominant polycystic kidney disease. Nat Commun. 2021;12(1):4548.

Dupont S, Morsut L, Aragona M, Enzo E, Giulitti S, Cordenonsi M, et al. Role of YAP/TAZ in mechanotransduction. Nature. 2011;474(7350):179-83.

Dwivedi D, Harry D, Meraldi P. Mild replication stress causes premature centriole disengagement via a sub-critical Plk1 activity under the control of ATR-Chk1. Nat Commun. 2023;14(1):6088.

Dwivedi N, Tao S, Jamadar A, Sinha S, Howard C, Wallace DP, et al. Epithelial Vasopressin Type-2 Receptors Regulate Myofibroblasts by a YAP-CCN2-Dependent Mechanism in Polycystic Kidney Disease. J Am Soc Nephrol. 2020;31(8):1697-710.

Fantus D, Rogers NM, Grahammer F, Huber TB, Thomson AW. Roles of mTOR complexes in the kidney: implications for renal disease and transplantation. Nat Rev Nephrol. 2016;12(10):587-609.

Faust TE, Feinberg PA, O'Connor C, Kawaguchi R, Chan A, Strasburger H, et al. A comparative analysis of microglial inducible Cre lines. Cell Rep. 2023;42(9):113031.

Foerster P, Daclin M, Asm S, Faucourt M, Boletta A, Genovesio A, et al. mTORC1 signaling and primary cilia are required for brain ventricle morphogenesis. Development. 2017;144(2):201-10.

Fu M, Hu Y, Lan T, Guan KL, Luo T, Luo M. The Hippo signalling pathway and its implications in human health and diseases. Signal Transduct Target Ther. 2022;7(1):376.

Fukasawa K, Choi T, Kuriyama R, Rulong S, Vande Woude GF. Abnormal centrosome amplification in the absence of p53. Science. 1996;271(5256):1744-7.

Galipeau PC, Cowan DS, Sanchez CA, Barrett MT, Emond MJ, Levine DS, et al. 17p (p53) allelic losses, 4N (G2/tetraploid) populations, and progression to aneuploidy in Barrett's esophagus. Proc Natl Acad Sci U S A. 1996;93(14):7081-4.

Galofré C, Asensio E, Ubach M, Torres IM, Quintanilla I, Castells A, et al. Centrosome reduction in newly-generated tetraploid cancer cells obtained by separase depletion. Sci Rep. 2020;10(1):9152.

Ganem NJ, Godinho SA, Pellman D. A mechanism linking extra centrosomes to chromosomal instability. Nature. 2009;460(7252):278-82.

Godinho SA, Picone R, Burute M, Dagher R, Su Y, Leung CT, et al. Oncogene-like induction of cellular invasion from centrosome amplification. Nature. 2014;510(7503):167-71.

Greil C, Engelhardt M, Wäsch R. The Role of the APC/C and Its Coactivators Cdh1 and Cdc20 in Cancer Development and Therapy. Front Genet. 2022;13:941565.

Habedanck R, Stierhof YD, Wilkinson CJ, Nigg EA. The Polo kinase Plk4 functions in centriole duplication. Nat Cell Biol. 2005;7(11):1140-6.

30. Harris PC, Torres VE. Polycystic kidney disease. Annu Rev Med. 2009;60:321-37.

Hartman TR, Liu D, Zilfou JT, Robb V, Morrison T, Watnick T, et al. The tuberous sclerosis proteins regulate formation of the primary cilium via a rapamycin-insensitive and polycystin 1-independent pathway. Hum Mol Genet. 2009;18(1):151-63.

Hebbar M, Kanthi A, Shukla A, Bielas S, Girisha KM. A biallelic 36-bp insertion in PIBF1 is associated with Joubert syndrome. J Hum Genet. 2018;63(8):935-9.

Inanç B, Dodson H, Morrison CG. A centrosome-autonomous signal that involves centriole disengagement permits centrosome duplication in G2 phase after DNA damage. Mol Biol Cell. 2010;21(22):3866-77.

Ito KK, Watanabe K, Ishida H, Matsuhashi K, Chinen T, Hata S, et al. Cep57 and Cep57L1 maintain centriole engagement in interphase to ensure centriole duplication cycle. J Cell Biol. 2021;220(3).

Jung GI, Rhee K. Triple deletion of TP53, PCNT, and CEP215 promotes centriole amplification in the M phase. Cell Cycle. 2021;20(15):1500-17.

Karki M, Keyhaninejad N, Shuster CB. Precocious centriole disengagement and centrosome fragmentation induced by mitotic delay. Nat Commun. 2017;8:15803.

Kim J, Jo H, Hong H, Kim MH, Kim JM, Lee JK, et al. Actin remodelling factors control ciliogenesis by regulating YAP/TAZ activity and vesicle trafficking. Nat Commun. 2015;6:6781.

Kim J, Kim J, Rhee K. PCNT is critical for the association and conversion of centrioles to centrosomes during mitosis. J Cell Sci. 2019;132(6).

Kim J, Lee K, Rhee K. PLK1 regulation of PCNT cleavage ensures fidelity of centriole separation during mitotic exit. Nat Commun. 2015;6:10076.

Kim K, Lee K, Rhee K. CEP90 is required for the assembly and centrosomal accumulation of centriolar satellites, which is essential for primary cilia formation. PLoS One. 2012;7(10):e48196.

Kim K, Lee S, Chang J, Rhee K. A novel function of CEP135 as a platform protein of C-NAP1 for its centriolar localization. Exp Cell Res. 2008;314(20):3692-700.

Kim K, Rhee K. The pericentriolar satellite protein CEP90 is crucial for integrity of the mitotic spindle pole. J Cell Sci. 2011;124(Pt 3):338-47.

Kim K, Rhee K. The pericentriolar satellite protein CEP90 is crucial for integrity of the mitotic spindle pole. J Cell Sci. 2011;124(Pt 3):338-47.

Kodani A, Yu TW, Johnson JR, Jayaraman D, Johnson TL, Al-Gazali L, et al. Centriolar satellites assemble centrosomal microcephaly proteins to recruit CDK2 and promote centriole duplication. Elife. 2015;4.

Kohlmaier G, Loncarek J, Meng X, McEwen BF, Mogensen MM, Spektor A, et al. Overly long centrioles and defective cell division upon excess of the SAS-4-related protein CPAP. Curr Biol. 2009;19(12):1012-8.

Krajcovic M, Johnson NB, Sun Q, Normand G, Hoover N, Yao E, et al. A non-genetic route to aneuploidy in human cancers. Nat Cell Biol. 2011;13(3):324-30.

Krzywicka-Racka A, Sluder G. Repeated cleavage failure does not establish centrosome amplification in untransformed human cells. J Cell Biol. 2011;194(2):199-207.

Kumar D, Rains A, Herranz-Pérez V, Lu Q, Shi X, Swaney DL, et al. A ciliopathy complex builds distal appendages to initiate ciliogenesis. J Cell Biol. 2021;220(9).

Kuznetsova AY, Seget K, Moeller GK, de Pagter MS, de Roos JA, Dürrbaum M, et al. Chromosomal instability, tolerance of mitotic errors and multidrug resistance are promoted by tetraploidization in human cells. Cell Cycle. 2015;14(17):2810-20.

Kwon M, Godinho SA, Chandhok NS, Ganem NJ, Azioune A, Thery M, et al. Mechanisms to suppress multipolar divisions in cancer cells with extra centrosomes. Genes Dev. 2008;22(16):2189-203.

Lachowski D, Cortes E, Robinson B, Rice A, Rombouts K, Del Río Hernández AE. FAK controls the mechanical activation of YAP, a transcriptional regulator required for durotaxis. Faseb j. 2018;32(2):1099-107.

Lambrus BG, Daggubati V, Uetake Y, Scott PM, Clutario KM, Sluder G, et al. A USP28-53BP1-p53-p21 signaling axis arrests growth after centrosome loss or prolonged mitosis. J Cell Biol. 2016;214(2):143-53.

Lambrus BG, Holland AJ. A New Mode of Mitotic Surveillance. Trends Cell Biol. 2017;27(5):314-21.

Lawo S, Hasegan M, Gupta GD, Pelletier L. Subdiffraction imaging of centrosomes reveals higher-order organizational features of pericentriolar material. Nat Cell Biol. 2012;14(11):1148-58.

Lee EJ, Seo E, Kim JW, Nam SA, Lee JY, Jun J, et al. TAZ/Wnt-β-catenin/c-MYC axis regulates cystogenesis in polycystic kidney disease. Proc Natl Acad Sci U S A. 2020;117(46):29001-12.

Lee JG, Yon JM, Kim G, Lee SG, Kim CY, Cheong SA, et al. PIBF1 regulates trophoblast syncytialization and promotes cardiovascular development. Nat Commun. 2024;15(1):1487.

Lee K, Boctor S, Barisoni LM, Gusella GL. Inactivation of integrin-β1 prevents the development of polycystic kidney disease after the loss of polycystin-1. J Am Soc Nephrol. 2015;26(4):888-95.

Lee K, Rhee K. Separase-dependent cleavage of pericentrin B is necessary and sufficient for centriole disengagement during mitosis. Cell Cycle. 2012;11(13):2476-85.

Lee S, Rhee K. CEP215 is involved in the dynein-dependent accumulation of pericentriolar matrix proteins for spindle pole formation. Cell Cycle. 2010;9(4):774-83.

Lens SMA, Medema RH. Cytokinesis defects and cancer. Nat Rev Cancer. 2019;19(1):32-45.

Li Z, Dai K, Wang C, Song Y, Gu F, Liu F, et al. Expression of Polo-Like Kinase 4(PLK4) in Breast Cancer and Its Response to Taxane-Based Neoadjuvant Chemotherapy. J Cancer. 2016;7(9):1125-32.

Liao Z, Zhang H, Fan P, Huang Q, Dong K, Qi Y, et al. High PLK4 expression promotes tumor progression and induces epithelial-mesenchymal transition by regulating the Wnt/β-catenin signaling pathway in colorectal cancer. Int J Oncol. 2019;54(2):479-90.

Lin F, Hiesberger T, Cordes K, Sinclair AM, Goldstein LS, Somlo S, et al. Kidney-specific inactivation of the KIF3A subunit of kinesin-II inhibits renal ciliogenesis and produces polycystic kidney disease. Proc Natl Acad Sci U S A. 2003;100(9):5286-91.

Loncarek J, Hergert P, Khodjakov A. Centriole reduplication during prolonged interphase requires procentriole maturation governed by Plk1. Curr Biol. 2010;20(14):1277-82.

Lu D, Hsiao JY, Davey NE, Van Voorhis VA, Foster SA, Tang C, et al. Multiple mechanisms determine the order of APC/C substrate degradation in mitosis. J Cell Biol. 2014;207(1):23-39.

Ma M. Cilia and polycystic kidney disease. Semin Cell Dev Biol. 2021;110:139-48.

Ma M, Gallagher AR, Somlo S. Ciliary Mechanisms of Cyst Formation in Polycystic Kidney Disease. Cold Spring Harb Perspect Biol. 2017;9(11).

Ma M, Tian X, Igarashi P, Pazour GJ, Somlo S. Loss of cilia suppresses cyst growth in genetic models of autosomal dominant polycystic kidney disease. Nat Genet. 2013;45(9):1004-12.

Marteil G, Guerrero A, Vieira AF, de Almeida BP, Machado P, Mendonça S, et al. Over-elongation of centrioles in cancer promotes centriole amplification and chromosome missegregation. Nat Commun. 2018;9(1):1258.

Matsuo K, Ohsumi K, Iwabuchi M, Kawamata T, Ono Y, Takahashi M. Kendrin is a novel substrate for separase involved in the licensing of centriole duplication. Curr Biol. 2012;22(10):915-21.

McConnachie DJ, Stow JL, Mallett AJ. Ciliopathies and the Kidney: A Review. Am J Kidney Dis. 2021;77(3):410-9.

Mennella V, Keszthelyi B, McDonald KL, Chhun B, Kan F, Rogers GC, et al. Subdiffraction-resolution fluorescence microscopy reveals a domain of the centrosome critical for pericentriolar material organization. Nat Cell Biol. 2012;14(11):1159-68.

Morretton JP, Simon A, Herbette A, Barbazan J, Pérez-González C, Cosson C, et al. A catalog of numerical centrosome defects in epithelial ovarian cancers. EMBO Mol Med. 2022;14(9):e15670.

Moya IM, Halder G. Hippo-YAP/TAZ signalling in organ regeneration and regenerative medicine. Nat Rev Mol Cell Biol. 2019;20(4):211-26.

Nishio S, Hatano M, Nagata M, Horie S, Koike T, Tokuhisa T, et al. Pkd1 regulates immortalized proliferation of renal tubular epithelial cells through p53 induction and JNK activation. J Clin Invest. 2005;115(4):910-8.

O'Connell KF, Caron C, Kopish KR, Hurd DD, Kemphues KJ, Li Y, et al. The C. elegans zyg-1 gene encodes a regulator of centrosome duplication with distinct maternal and paternal roles in the embryo. Cell. 2001;105(4):547-58.

Ogden A, Rida PC, Aneja R. Prognostic value of CA20, a score based on centrosome amplification-associated genes, in breast tumors. Sci Rep. 2017;7(1):262.

Ong AC, Devuyst O, Knebelmann B, Walz G. Autosomal dominant polycystic kidney disease: the changing face of clinical management. Lancet. 2015;385(9981):1993-2002.

Orhon I, Dupont N, Zaidan M, Boitez V, Burtin M, Schmitt A, et al. Primary-cilium-dependent autophagy controls epithelial cell volume in response to fluid flow. Nat Cell Biol. 2016;18(6):657-67.

Panda DK, Bai X, Zhang Y, Stylianesis NA, Koromilas AE, Lipman ML, et al. SCF-SKP2 E3 ubiquitin ligase links mTORC1/ER stress/ISR with YAP activation in murine renal cystogenesis. J Clin Invest. 2022;132(24).

Pannu V, Mittal K, Cantuaria G, Reid MD, Li X, Donthamsetty S, et al. Rampant centrosome amplification underlies more aggressive disease course of triple negative breast cancers. Oncotarget. 2015;6(12):10487-97.

Pazour GJ, Dickert BL, Vucica Y, Seeley ES, Rosenbaum JL, Witman GB, et al. Chlamydomonas IFT88 and its mouse homologue, polycystic kidney disease gene tg737, are required for assembly of cilia and flagella. J Cell Biol. 2000;151(3):709-18.

Pernicone N, Peretz L, Grinshpon S, Listovsky T. MDA-MB-157 Cell Line Presents High Levels of MAD2L2 and Dysregulated Mitosis. Anticancer Res. 2020;40(10):5471-80.

Potapova TA, Seidel CW, Box AC, Rancati G, Li R. Transcriptome analysis of tetraploid cells identifies cyclin D2 as a facilitator of adaptation to genome doubling in the presence of p53. Mol Biol Cell. 2016;27(20):3065-84.

Press MF, Xie B, Davenport S, Zhou Y, Guzman R, Nolan GP, et al. Role for polo-like kinase 4 in mediation of cytokinesis. Proc Natl Acad Sci U S A. 2019;116(23):11309-18.

Prosser SL, Samant MD, Baxter JE, Morrison CG, Fry AM. Oscillation of APC/C activity during cell cycle arrest promotes centrosome amplification. J Cell Sci. 2012;125(Pt 22):5353-68.

Sagona AP, Stenmark H. Cytokinesis and cancer. FEBS Lett. 2010;584(12):2652-61.

Sala R, Farrell KC, Stearns T. Growth disadvantage associated with centrosome amplification drives population-level centriole number homeostasis. Mol Biol Cell. 2020;31(24):2646-56.

Schrock MS, Stromberg BR, Scarberry L, Summers MK. APC/C ubiquitin ligase: Functions and mechanisms in tumorigenesis. Semin Cancer Biol. 2020;67(Pt 2):80-91.

Seo MY, Jang W, Rhee K. Integrity of the Pericentriolar Material Is Essential for Maintaining Centriole Association during M Phase. PLoS One. 2015;10(9):e0138905.

Shao X, Somlo S, Igarashi P. Epithelial-specific Cre/lox recombination in the developing kidney and genitourinary tract. J Am Soc Nephrol. 2002;13(7):1837-46.

Shillingford JM, Murcia NS, Larson CH, Low SH, Hedgepeth R, Brown N, et al. The mTOR pathway is regulated by polycystin-1, and its inhibition reverses renal cystogenesis in polycystic kidney disease. Proc Natl Acad Sci U S A. 2006;103(14):5466-71.

Shin B, Kim MS, Lee Y, Jung GI, Rhee K. Generation and Fates of Supernumerary Centrioles in Dividing Cells. Mol Cells. 2021;44(10):699-705.

Shindo N, Otsuki M, Uchida KSK, Hirota T. Prolonged mitosis causes separase deregulation and chromosome nondisjunction. Cell Rep. 2021;34(3):108652.

Shukla A, Kong D, Sharma M, Magidson V, Loncarek J. Plk1 relieves centriole block to reduplication by promoting daughter centriole maturation. Nat Commun. 2015;6:8077.

Song S, Jung S, Kwon M. Expanding roles of centrosome abnormalities in cancers. BMB Rep. 2023;56(4):216-24.

Szekeres-Bartho J, Šućurović S, Mulac-Jeričević B. The Role of Extracellular Vesicles and PIBF in Embryo-Maternal Immune-Interactions. Front Immunol. 2018;9:2890.

Tan AY, Zhang T, Michaeel A, Blumenfeld J, Liu G, Zhang W, et al. Somatic Mutations in Renal Cyst Epithelium in Autosomal Dominant Polycystic Kidney Disease. J Am Soc Nephrol. 2018;29(8):2139-56.

Totaro A, Panciera T, Piccolo S. YAP/TAZ upstream signals and downstream responses. Nat Cell Biol. 2018;20(8):888-99.

Turlo KA, Gallaher SD, Vora R, Laski FA, Iruela-Arispe ML. When Cre-mediated recombination in mice does not result in protein loss. Genetics. 2010;186(3):959-67.

Wang L, Zhang J, Wan L, Zhou X, Wang Z, Wei W. Targeting Cdc20 as a novel cancer therapeutic strategy. Pharmacol Ther. 2015;151:141-51.

Watnick TJ, Torres VE, Gandolph MA, Qian F, Onuchic LF, Klinger KW, et al. Somatic mutation in individual liver cysts supports a two-hit model of cystogenesis in autosomal dominant polycystic kidney disease. Mol Cell. 1998;2(2):247-51.

Wheway G, Schmidts M, Mans DA, Szymanska K, Nguyen TT, Racher H, et al. An siRNA-based functional genomics screen for the identification of regulators of ciliogenesis and ciliopathy genes. Nat Cell Biol. 2015;17(8):1074-87.

Wu G, D'Agati V, Cai Y, Markowitz G, Park JH, Reynolds DM, et al. Somatic inactivation of Pkd2 results in polycystic kidney disease. Cell. 1998;93(2):177-88.

Yu SS, Wang E, Chiang CY, Cheng PH, Yeh YS, Wu YY, et al. Large deletion of Wdr19 in developing renal tubules disrupts primary ciliogenesis, leading to polycystic kidney disease in mice. J Pathol. 2022;257(1):5-16.

Zack TI, Schumacher SE, Carter SL, Cherniack AD, Saksena G, Tabak B, et al. Pan-cancer patterns of somatic copy number alteration. Nat Genet. 2013;45(10):1134-40.

Zerres K, Mücher G, Bachner L, Deschennes G, Eggermann T, Kääriäinen H, et al. Mapping of the gene for autosomal recessive polycystic kidney disease (ARPKD) to chromosome 6p21-cen. Nat Genet. 1994;7(3):429-32.

Zhang Y, Reif G, Wallace DP. Extracellular matrix, integrins, and focal adhesion signaling in polycystic kidney disease. Cell Signal. 2020;72:109646.

ABSTRACT IN KOREAN
(국문 초록)

중심체는 거의 모든 종류의 동물 세포에 보편적으로 존재하는 세포 소기관이다. 중심체는 분열기 방추체의 형성과 세포 간기 미세소관의 형성과 같은 다양한 과정에 관련되어 있다. 중심체의 또 다른 필수적 기능은 중심 섬모 형성을 위한 주형 역할이다. 중심 섬모는 다양한 신호전달 체계를 통합하고 조절하는 세포의 안테나로서 기능한다. 중심체의 보편적 존재 양상을 주지하면, 중심 섬모 역시 다양한 종류의 세포에서 기능한다. 이것들의 광범위한 역할로 인해서 중심체와 중심 섬모의 구조적 혹은 기능적 이상은 암이나 다낭성 신장 질환과 같은 다양한 질병과 연관되어 있다. 그러나 이 소기관들의 이상이 질병으로 어떻게 이어지는지에 대해서는, 이러한 질병들이 매우 다측면적이고 다양한 생리학적 맥락에서 일어난다는 사실로 인해서 아직까지 연구가 미비하다.

이 연구에서, 연구자는 암과 다낭성 신장 질환의 맥락에서 중심체와 중심 섬모 이상의 새로운 측면에 대해 연구하였다. 암에서의 중심체 이상을 규명하는 일환으로서, 연구자는 암세포에서 세포 분열기의 중심체 과복제 현상에 대한 새로운 매커니즘을 연구하였다. 일련의 암세포주를 사용하여 연구자는 세포 주기와 중심체 과복제 간의 관계를 파악하였다. 또한 일부 세포주가 세포 분열기에서의 중심체 과복제라는 새로운 방식의 과복제를 나타내는 것을 확인하였다. 분열기 특이적인 중심체 과복제 현상을 더 깊이 규명하기 위해 연구자는 세포주들의 중심체 분리, 중심체 복제 효소를 막는 약물에 대한 반응성,

그리고 세포의 중심구의를 연구하여 중심체의 특성을 밝혔다. 추가적으로 일부 세포주들에서 중심구의 과발현이 중심체 과복제를 저해한다는 사실을 입증하였다. 이러한 결과들을 바탕으로하여, 연구자는 역치 이하의 중심구가 암세포에서 중심체 과복제를 유발한다는 사실을 제시한다.

신장 질환에서의 중심 섬모 이상을 연구하는 일환으로서는, 연구자는 Cep90 유전자가 신장에서 특이적으로 결실된 마우스 모델을 이용하여 중심 섬모의 이상으로 발병하는 신장 질환의 진행 양상에 대해 연구하였다. Cep90 결실 마우스는 다낭성 신장과 함께 중심 섬모의 결실을 나타냈다. 특히나 Cep90 결실 마우스는 느린 발병을 보임으로써 신장낭 형성에 있어서 섬모의 관여 양상에 대한 상세한 분석을 가능케하였다. Cep90 결실 마우스는 구성 세포들이 중심 섬모를 완전히 잃어버린 후기 신장낭과 중심 섬모를 가진 세포들이 일부 남아있는 초기 신장낭이 혼재된 신장을 가지고 있었다. 연구자는 신장낭 발병과 관련된 다양한 신호전달 체계에 대해 조사하여 그들 간의 시간적 역동성이 있는 것을 확인하였다. mTOR 신호는 초기 신장낭의 중심 섬모 결실 세포에서만 특이적으로 활성화된 반면에 YAP은 초기와 후기 신장낭 모두에서 섬모의 유무 상관 없이 활성화되어 있었다. 이러한 결과들을 바탕으로 하여 연구자는 중심 섬모의 결함이 시간적 역동성을 갖는 직간접적 경로를 통해 다낭성 신장을 유발한다는 사실을 제안한다.

주요어 : 중심체, 중심구, Cep90, 암, 다낭성 신장

학번 : 2020-21683

감사의 말

시

파블로 네루다

그러니까 그 나이였어… 시가 나를 찾아왔어. 몰라, 그게 어디서 왔는지,
모르겠어, 겨울에서인지 강에서인지, 언제 어떻게 왔는지 모르겠어.
아냐, 그건 목소리가 아니었고, 말도 아니었으며, 침묵도 아니었어,
하여간 어떤 길거리에서 나를 부르더군.
밤의 가지에서, 갑자기 다른 것들로부터, 격렬한 불 속에서 불렀어.
또한 혼자 돌아오는데 말야, 그렇게 얼굴없이 있는 나를 그게 건드리더군.

나는 뭐라고 해야 할지 몰랐어,
내 입은 이름들을 도무지 대지 못했고, 눈은 멀었으며,
내 영혼 속에서 뭔가 시작되어 있었어,
끓어오르는 열기 또는 잃어버린 날개, 내 나름대로 해보았어.
그 불을 해독하며, 나는 어렴풋한 첫 줄을 섰어
어렴풋한, 뭔지 모를, 순전한 넌센스.
아무것도 모르는 어떤 사람의 순수한 지혜,
그리고 문득 나는 보았어.
풀리고 열린 하늘을, 유성들을,
고동치는 논밭, 구멍뚫린 그림자, 화살과 불과 꽃들로 들쑤셔진 그림자,
휘감아도는 밤, 우주를, 그리고 나, 이 미소한 존재는
그 큰 별들 총총한 허공에 취해, 신비의 모습에 취해,
나 자신이 그 심연의 일부임을 느꼈고, 별들과 더불어 굴렀으며,
내 심장은 바람에 풀렸어.

유년기의 어떤 시절에 다가왔던 열병처럼, 소리 없이 내게 다가와 나를 감싼 학문에 감사합니다.
그리고 그 소리마저 들을 수 있게 해주신 선생님께 감사드립니다..
마지막으로 학문과 함께 하는 삶을 선물해주신 모든 가족들께 감사드립니다.
앞으로 더욱 학문(詩)을 사랑하며 살겠습니다.